Vol. 43 | Special Issue 1 | July 2024

MALAYSIAN JOURNAL OF SCIENCE

Special Issue: 2nd Euro-Asia Conference on CO_2 Capture and Utilisation (EACCO2CU2022)

MJS Guest Editor
Prof. Dr. Wan Jefrey Basirun

Special Issue Editors
Dr. Mohd Arif Mohd Sarjidan
Dr. Mohd Zieauddin Kufian

Guest Editors
Prof. Mohamed Kheireddine Aroua
Prof. Ir. Dr. Rozita Binti Yusoff

Published: 31-07-2024

MALAYSIAN JOURNAL OF SCIENCE

MJS

ISSN 1394-3065

Malaysian Journal of Science is indexed in Scopus, EMBASE, Compendex, GEOBASE, EMBiology, Elsevier BIOBASE, FLUIDEX ,World Textiles, CAB Abstracts, Chemical Abstracts Service Database and ASEAN Citation Index (ACI).

Selected papers from the

2ND EURO-ASIA CONFERENCE ON CO2 CAPTURE AND UTILIZATION (EACCO2CU2022)

Sunway University, Malaysia. 6th - 8th December 2022.

Climate change is a real threat to life on earth to which carbon dioxide is recognized as the major contributor. This makes reduction in CO_2 emissions a worldwide emergency and priority. To achieve climate change goals, including those established in the Paris Agreement, and United Nations (UN) Sustainable Development Goals (SDGs), (particularly SDG13 and SDG7), new scientific discoveries and innovative technologies to mitigate carbon dioxide emissions are needed. Recognizing the importance of this issue, the Centre for Carbon Dioxide Capture and Utilization of Sunway University is organizing the 2nd Euro-Asia Conference on CO_2 capture and utilisation ($EACCO_2CU$) was held on 6th - 8th December 2022 at Sunway University, Malaysia.

This is a continuation of $EACCO_2CU$ 2019, the conference was successful, involving 55 participants from various countries originating from Europe and Asia. This year, the conference offers opportunities for academicians, researchers, and industry experts to meet, share their knowledge and new ideas with local and international participants. In addition, participants also can engage with distinguished invited speakers who delivered keynote and plenary talks. Discover the latest trends and challenges in CO_2 capture and utilisation through Zoom platform at $EACCO_2CU$ 2022.

MALAYSIAN JOURNAL OF SCIENCE
MJS
ISSN 1394 - 3065

2nd Euro-Asia Conference on CO_2 Capture and Utilization (EACCO2CU2022)

Special issue

Malaysian Journal of Science 43 (Special Issue 1): 1-7 (July 2024)

https://mjs.um.edu.my

THE EFFECT OF CHEMICAL ACTIVATION AGENTS AND ACTIVATION TEMPERATURE ON THE PORE STRUCTURE OF RICE HUSK-DERIVED ACTIVATED CARBON

Dendi Adi Saputra[1a*], Adjar Pratoto[2a], Muhammad Fadhil Rahman[3a], Akio Kodama[4b]

Abstract: This study investigates the optimization of production parameters for rice husk-derived activated carbon, targeting its effective application in direct air capture (DAC) technology. Various chemical activation agents—potassium hydroxide (KOH), urea, and their combination—and activation temperatures (600°C, 700°C, and 800°C) were explored using pyrolysis. The morphology of the resulting activated carbon was analyzed via scanning electron microscopy (SEM) and ImageJ. Results demonstrate that the choice of activation agent and temperature significantly influence pore diameter size and quantity. Higher temperatures led to smaller pore diameters and an increased number of pores. The combination of KOH and urea at 800°C produced the most favorable particle size (0.811 µm), suitable for applications requiring a well-defined pore structure. This combination also exhibited the most even pore distribution and highest pore density. These findings provide valuable insights for optimizing the production of rice husk-derived activated carbon, contributing to the development of sustainable and effective sorbents for CO_2 capture in DAC technology. Additionally, they offer potential for broader applications of husk-activated carbon in various industrial and environmental fields.

Keywords: Direct air capture, activated carbon, rice husk, chemical activation agents, activation temperature

1. Introduction

The escalating atmospheric CO_2 burden necessitates immediate intervention. Deploying efficient and sustainable CO_2 capture technologies is critical to mitigate its adverse impacts. Current options include pre-combustion, post-combustion, and oxyfuel capture methods, serving as platforms for further advancement (Cannone et al., 2021). However, the spatiotemporal variability of atmospheric CO_2 concentrations presents a significant challenge for the widespread implementation of capture technologies (Deng et al., 2021). Consequently, direct air capture (DAC) technology has emerged as a promising approach, focusing on directly removing CO_2 from ambient air.

DAC technology represents a negative emissions technique that can directly reduce CO_2 concentrations in the atmosphere. One of its key advantages is independence from concentrated emission sources, such as flue gases from cement plants, steam power plants, and steel processing facilities, making it a promising option for achieving significant CO_2 reduction targets. However, several challenges must be addressed to successfully develop and deploy DAC technology. These challenges include the low partial pressure of CO_2 in the air, which reduces the sorbent's efficiency, as well as the low thermal and chemical stability of the sorbent material and the high energy requirements for sorbent regeneration (Lee et al., 2021). The search for environmentally friendly sorbent candidates has become crucial to advance DAC technology within the framework of a green economy. This study aims to identify sorbents that possess the desired characteristics for efficient CO_2 capture. Ideal criteria for sorbent materials include high specific surface area, high thermal conductivity, high CO_2 adsorption capacity, high selectivity for CO_2 over N_2, high porosity, ease of recyclability, and low energy consumption for regeneration (Dissanayake et al., 2020; Shi et al., 2020; Wang et al., 2023).

Several adsorbents such as porous carbon (Dissanayake et al., 2020), activated carbon (Rinawati et al., 2019), zeolite (Zhang et al., 2019), metal-organic frameworks (Elhenawy et al., 2020), and nanomaterials (Segneri et al., 2023) have been studied for CO_2 capture applications. These materials demonstrate excellent CO_2 adsorption performance. However, the difficulty of finding raw materials and the limited availability of materials pose challenges in terms of cost-effectiveness and commercial feasibility for industrial applications (Goembira et al., 2021). To overcome this problem, the synthesis of activated carbon from rice husks has received much attention. Activated carbon derived from rice husks is known for its extraordinary adsorption capabilities, making it a versatile and popular adsorbent material (Rinawati et al., 2019; Yaumi et al., 2018; Hussin et al., 2021). Utilizing agricultural waste as a precursor for activated carbon synthesis aligns with the increasing environmental concerns and the demand for sustainable practices. Rice husks, an abundant byproduct of rice milling, offer significant potential as a cost-efficient and sustainable source of activated carbon, particularly in regions such as West Sumatera, Indonesia, where rice cultivation is prevalent. However, the properties and functionality of activated carbon are significantly influenced by various factors,

Authors information:
[a]Department of Mechanical Engineering, Faculty of Engineering, Universitas Andalas, Padang, West Sumatera 25163, Indonesia. Email: dendias@eng.unand.ac.id[1], adjar.pratoto@eng.unand.ac.id[2], fadil.rahman86@gmail.com[3],
[b]Institute for Frontier Science Initiative, Kanazawa University, Kakumamachi, Kanazawa, Ishikawa 920-1192, Japan. Email: akodama@se.kanazawa-u.ac.jp[4]

*Corresponding author e-mail: dendias@eng.unand.ac.id

Received: February 7, 2024
Accepted: May 7, 2024
Published: July 31, 2024

DOI: https://doi.org/10.22452/mjs.vol43sp1.1
Malaysian Journal of Science 43 (Special Issue 1): 1-7 (July 2024)

such as the selection of chemical activating agents and the activation temperature (Jouhara et al., 2018).

Therefore, it is important to know the optimal combination of chemical activating agents and activation temperature to optimize the production process and improve the performance of activated carbon derived from rice husks. This research aims to determine the most suitable parameters to produce activated carbon with the desired characteristics, especially a clear pore structure. Observations of pore structure focus on the size, shape, distribution, and density. The results of these observations can not only be used as a reference for determining treatments and materials as CO_2 adsorbents but can also be applied to various industrial and environmental applications. Industrial and environmental applications of activated carbon include supercapacitors, water filters, oil and gas purifiers, poison absorbers, pharmaceutical product cleaners, and aroma and taste absorbers.

Research to determine the microstructural parameters of a material has been carried out, but the material observed is often nanoporous. Such research is necessary to use statistical analysis methods to process large arrays of nanosized pores, develop methodologies and algorithms to study morphological and nanostructural features, and automate the measurement process (Lushpa et al., 2018). In this research, the observations focused on activated carbon material from rice husk charcoal with a different end goal. The observed characterization only focuses on morphological observations using Scanning Electron Microscopy (SEM) which will be used as quantitative data with the help of the ImageJ application.

The size, shape, distribution, and density of rice husk-activated carbon treated with physical and chemical activation variations were observed. To achieve this objective, a systematic experimental approach was employed. Various chemical activating agents, namely potassium hydroxide (KOH), urea, and a combination of KOH and urea, were selected for the activation process. Different activation temperatures within a predetermined range of 600°C, 700°C, and 800°C were considered. The activation process was carried out using the pyrolysis method. Meanwhile, the rice husk-derived activated carbon morphology was investigated using scanning electron microscopy (SEM) and the ImageJ application. The experimental results provided insights into the impact of different activating agents and activation temperatures on the pore diameter size and pore quantity of the activated carbon derived from rice husk. By understanding the correlation between the synthesis variables and the properties of activated carbon, this research seeks to contribute to the development of effective treatments to produce activated carbon that can be applied in industry and the environment.

2. Materials and methods

2.1 Materials

Rice husk (Oryza sativa L.), obtained from a rice mill in Padang, West Sumatera, Indonesia, was selected as the raw material. The rice husks were cleaned with distilled water to remove adhering dust and inorganic impurities and then dried at 105°C for 12 hours. Potassium hydroxide (KOH ≤ 100%) was purchased from PT Smart Lab Indonesia, and urea (CH4N2O ≤ 99%) was obtained from Pudak Scientific. Before testing, the samples were cleaned and neutralized with distilled water and hydrochloric acid (HCl 15%) purchased from Rofa Laboratory Centre.

2.2 Preparation of sample

Activated carbon (AC) was prepared using the pyrolysis method, as shown in the flow diagram in Figure 1. Initially, the cleaned rice husks were placed in a container for carbonization. Prior to the carbonization process, nitrogen was introduced into the furnace for 5 minutes at a flow rate of 80 ml/min to displace oxygen and prevent combustion reactions. The carbonization process was conducted at 500°C with a heating rate of 10°C/minute for 2 hours, while nitrogen continued to flow at a rate of 80 ml/minute. After cooling to room temperature, the resulting biochar was removed from the furnace for the activation process.

In the activation process, the biochar was impregnated with activating agents (KOH, urea, and a combination of KOH and urea) to produce porous carbon, with a mass ratio of 1:2 (mass of adsorbent: activating agents). The mixture was stirred and left for 12 hours at 60°C. Subsequently, the samples were pyrolyzed in the furnace for 1 hour at various activation temperatures of 600°C, 700°C, and 800°C, with a nitrogen flow of 50 ml/minute. After cooling to room temperature, the samples were taken out of the furnace and immersed in a 15% HCl solution, followed by repeated washing with distilled water until the washing solution became neutral. The samples were then dried for 24 hours in an oven at 80°C. Finally, the activated carbon samples were stored in sample bags.

2.3 Characterization

2.3.1 Morphology investigation using field emission Scanning Electron Microscopy (SEM)

The morphology of the activated carbon samples was studied using field emission scanning electron microscopy (SEM). The samples were placed on SEM stubs and plated with carbon, followed by gold for two minutes using an argon plasma metallizer (sputter coater K575X) (Edwards Limited, Crawley, United Kingdom) to reduce electron charge through the sputtering process. Field Emission Scanning Electron Microscopy (FEI Nova Nano SEM 230) was utilized with a 10 kV voltage to optimize the observation of sample surface morphology at 5000x magnification.

2.3.2 Measurement pore diameter dan pore number using ImageJ application

The ImageJ application was chosen for measuring the pore diameter and pore number due to its simplicity and user-friendly

DOI: https://doi.org/10.22452/mjs.vol43sp1.1
Malaysian Journal of Science 43 (Special Issue 1): 1-7 (July 2024)

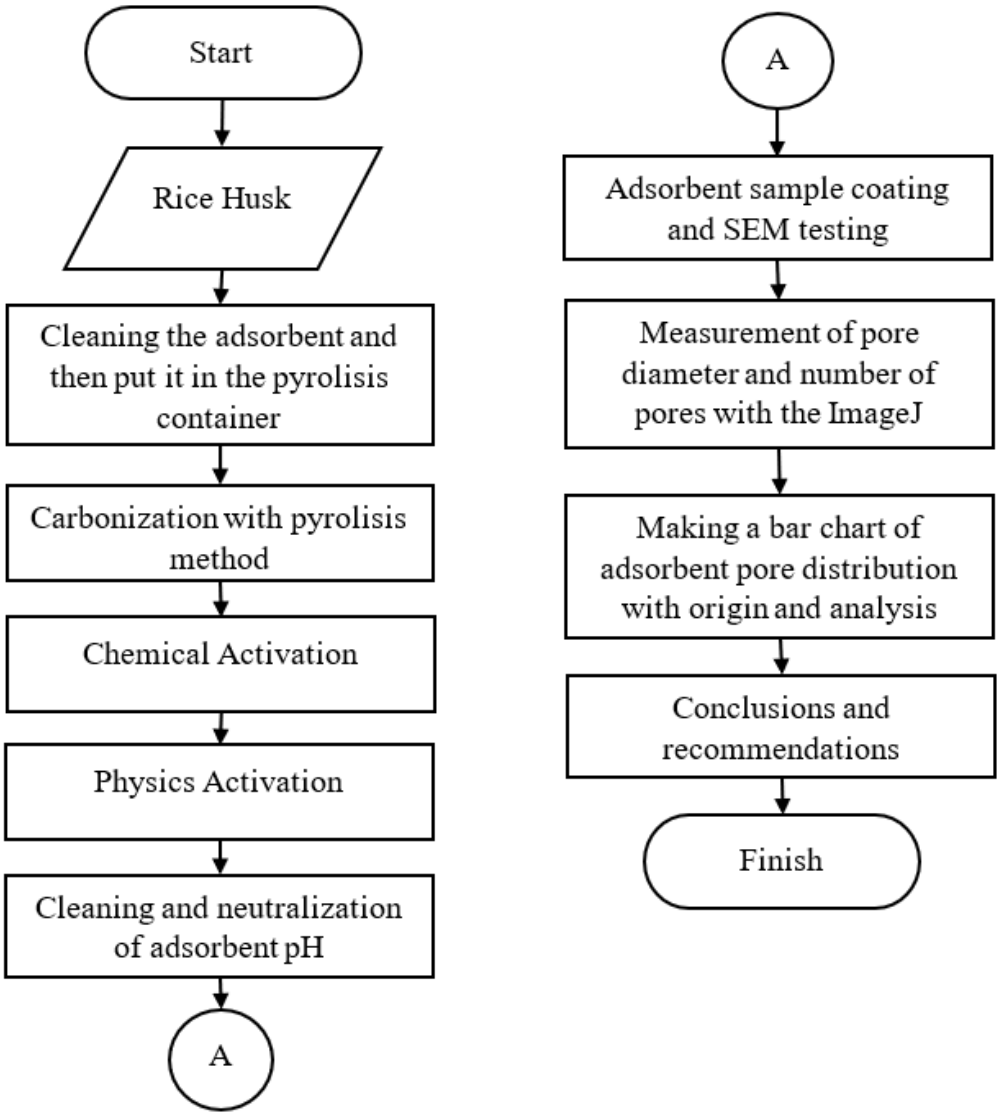

Figure 1. Sample Preparation Flow Diagram

interface. ImageJ is widely used open-source software that provides various image analysis tools, making it suitable for analyzing SEM images and extracting quantitative data. To begin the measurement process, the SEM images were imported into the ImageJ software. The images were calibrated to ensure accurate measurements by aligning the scale and line tool units with the SEM ruler. This calibration step allowed for precise conversion of pixel dimensions into real-world measurements.

The SEM images were divided into four sections for more manageable and systematic measurements. This division helped avoid confusion and ensure consistency in the measurements across the image. Using the line tool in ImageJ, manual measurements of pore diameter and pore number were conducted on each section of the SEM images. The line tool allowed for the selection of individual pores, and their diameters were measured directly from the images. Additionally, the number of pores present in each section was counted manually.

Once the pore diameter and pore number data were obtained, further analysis was conducted by grouping the data based on the same activation temperature and activating agent. This grouping allowed for a comprehensive examination of the influence of different activating agents and activation temperatures on the pore characteristics of the rice husk-activated carbon. To visualize the distribution of pore diameters, the data were processed using OriginPro 2019 software. The software facilitated the creation of a bar chart, where the pore sizes were plotted along the x-axis, and the corresponding frequencies or counts were represented on the y-axis. This graphical representation provided a clear understanding of the pore size distribution in the rice husk-activated carbon samples.

The analysis of the bar chart was crucial for assessing the characteristics of the adsorbent material. By comparing the pore diameter distributions resulting from different activating agents and activation temperatures, valuable insights could be gained

DOI: https://doi.org/10.22452/mjs.vol43sp1.1
Malaysian Journal of Science 43 (Special Issue 1): 1-7 (July 2024)

regarding the impact of these parameters on the surface conditions and adsorption properties of the rice husk-activated carbon.

3. Results and discussions

3.1 Effect of chemical activation agents and activation temperatures on the morphology of adsorbent

Figure 2 (a - i) visually represents the morphology resulting from different chemical activation agents (KOH, urea, KOH+urea) at various activation temperatures on the pore formation process in rice husk-derived activated carbon. Specifically, Figure 2 (a-c) illustrates the formation of pores in activated carbon using KOH, urea, and a combination of KOH and urea at an activation temperature of 600°C. The presence of visible boundaries between pores is evident in these samples. This phenomenon is also observed with the activation agent urea and the combination of KOH and urea.

Furthermore, when the activation temperature was increased from 700°C to 800°C, there was a noticeable enhancement in pore formation, as shown in Figure 2 (d-i). This result indicates that the activation process becomes more effective and efficient at higher temperatures. The higher temperature provides the necessary energy for enhanced chemical reactions and for developing a more extensive pore structure in the rice husk-activated carbon. As a result, the visible boundaries between pores observed at 600°C start to diminish, suggesting a more complete and optimized activation process at 800°C.

This phenomenon can be explained by the fact that potassium hydroxide (KOH), being a strong alkali, exhibits corrosive properties towards carbonaceous materials at high temperatures. Consequently, it has the ability to permeate through the material, creating a significant number of pores. Additionally, the reaction between KOH and carbon during the activation process generates gas. The effusion of this gas contributes to the expansion and enlargement of the pore structure. Thus, the combined effects of chemical reactions and gas effusion play a crucial role in altering the particle size of rice husk-activated carbon when KOH is used as the activating agent.

Furthermore, urea plays a significant role in the pore formation process of rice husk-activated carbon. When urea is used as an activation agent, it undergoes thermal decomposition during the activation process. This decomposition releases gases, such as ammonia (NH_3) and carbon dioxide (CO_2), which create pressure within the carbon matrix. The pressure generated by the gas release helps to create pores in the rice husk-activated carbon. The gases diffuse through the carbonaceous material, causing the formation of voids and channels. These voids and channels contribute to the development of a porous structure in the activated carbon. The decomposition of urea and the subsequent gas release also facilitate the removal of volatile

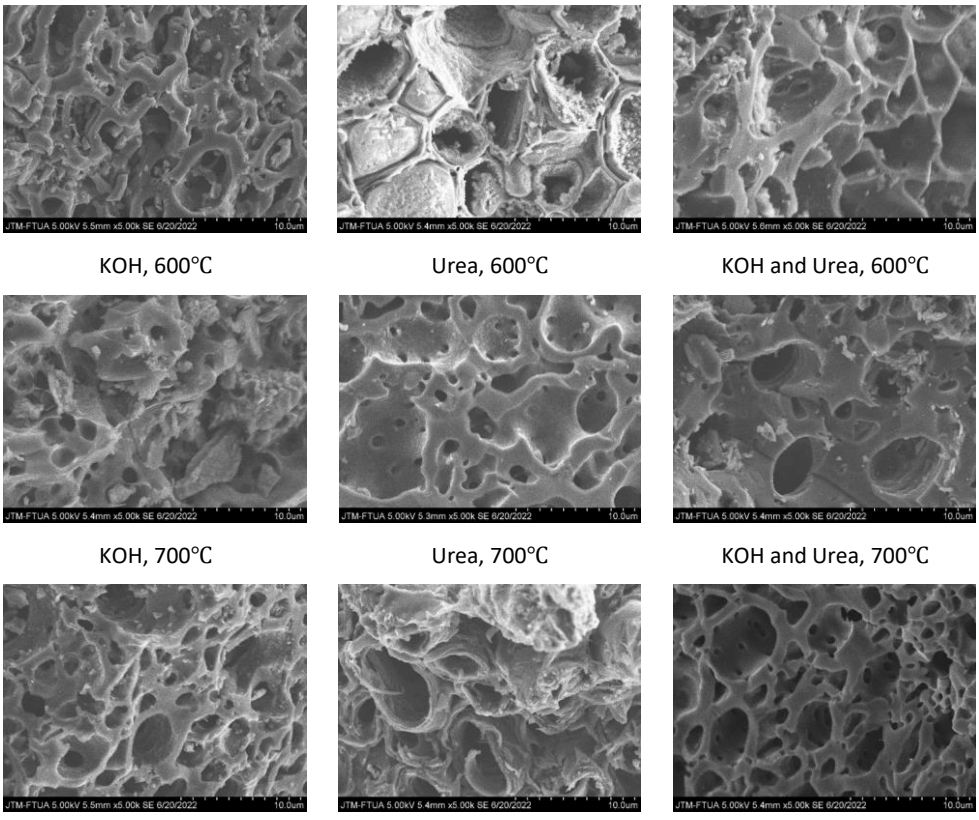

Figure 2. Morphology view of rice husk activated carbon at various chemical activating agents and activation temperatures

DOI: https://doi.org/10.22452/mjs.vol43sp1.1
Malaysian Journal of Science 43 (Special Issue 1): 1-7 (July 2024)

components and impurities from the rice husk, resulting in a purer and more highly porous carbon material.

Meanwhile, the combination of KOH and urea as activation agents for rice husk-activated carbon at high temperatures leads to several significant effects. Firstly, the interaction between KOH and urea initiates chemical reactions with the carbon precursor (rice husk), resulting in the decomposition and transformation of the carbonaceous material. This process releases gases and creates pores. Additionally, the combination of KOH and urea exhibits a synergistic effect on the activation process. The presence of both agents together enhances pore formation compared to using them individually, possibly due to a more efficient activation process or the generation of unique pore structures.

Moreover, the combined activation process promotes the release of gases, such as ammonia (NH_3) and carbon dioxide (CO_2), which contribute to the expansion and enlargement of the pore structure in the rice husk-activated carbon. The effusion of these gases facilitates the creation of interconnected pores, resulting in an overall increase in the material's porosity. Thus, the combined use of KOH and urea at high temperatures effectively induces chemical reactions, exhibits synergistic effects, and promotes gas release, all of which play crucial roles in pore formation and the development of a highly porous activated carbon material.

3.2 Effect of chemical activation agents and activation temperatures on the size and number of pores

The effects of chemical activation agents (KOH, urea, KOH + urea) and activation temperatures on the size and number of pores in rice husk-activated carbon were investigated. SEM images were analyzed using the ImageJ application, providing quantitative data on pore characteristics. The number and diameter of pores under various chemical activation agents at temperatures of 600°C, 700°C, and 800°C are presented in Figure 3 (a-c). Table 1 shows the average pore diameter of rice husk-activated carbon formed under different conditions. The KOH + urea activating agents produced a smaller average pore size (0.92 µm) than urea (1.17 µm) and KOH (1.2 µm). An activation temperature of 700°C resulted in a smaller average pore size (1.00 µm) compared to activation temperatures of 800°C (1.01 µm) and 600°C (1.28 µm).

During the activation process, the chemical activation agents (KOH, urea, and their combination) primarily act as catalysts and react with the carbonaceous components in the rice husk. However, the structural properties of the precursor material seem to play a dominant role in determining pore size rather than the specific activation agents used. The natural composition and arrangement of the carbonaceous components within the rice husk result in a relatively consistent range of pore diameters. Despite the use of different activation agents, the resulting pore diameter in the rice husk-activated carbon remains relatively unchanged. This suggests that the unique characteristics of the rice husk material itself strongly influence the resulting pore size, overriding the individual effects of the activation agents.

Table 1. Average diameter of activated carbon with various variations

		Chemical Activation Agents		
		KOH (µm)	Urea (µm)	KOH+Urea µm)
Activation Temperatures	600°C	1.40	1.37	1.06
	700°C	1.11	1.00	0.90
	800°C	1.10	1.13	0.81

The increase in activation temperature correlating with an increase in the number of pores in the rice husk-activated carbon can be attributed to enhanced reactivity between the chemical activation agents and the material at higher temperatures. Higher activation temperatures increase thermal energy for chemical reactions, promoting more extensive and efficient interactions between the activation agents (KOH, urea, KOH + urea) and the carbonaceous components in the rice husk. The chemical activation agents act as catalysts, facilitating the removal of volatile matter and the development of porosity in the rice husk material. Higher temperatures provide the necessary energy for these reactions to occur at a faster rate and to a greater extent, leading to the formation of additional pores.

Among the various combinations tested, the combination of KOH and urea as chemical activation agents at an activation temperature of 800°C yielded the most favorable results in terms of particle size, as shown in Figure 3 (c). This specific combination and temperature likely provided an optimal environment for the reactions to occur, resulting in a well-defined pore structure. The average diameter of the porous particles obtained under these conditions was measured to be 0.811 µm. This particle size is particularly suitable for applications requiring a well-defined pore structure, such as adsorption, gas separation, or catalysis. The presence of well-defined pores allows for efficient adsorption and separation processes, maximizing the material's performance in these applications.

In summary, the activation temperature increase in the number of pores in the rice husk-activated carbon can be attributed to higher temperatures facilitating more extensive reactions between the chemical activation agents and the material. The use of KOH and urea as activation agents at an activation temperature of 800°C resulted in the most favorable particle size.

4. Conclusion

The experimental results and discussions elucidate the effects of chemical activation agents and activation temperatures on the morphology, size, and number of pores in rice husk-activated carbon. SEM images clearly show the impact of different activation agents (KOH, urea, KOH + urea) on pore formation at various activation temperatures. The results indicate that an increase in activation temperature correlates with increased pore formation in the rice husk-activated carbon. This can be attributed to the higher thermal energy available at elevated temperatures, which facilitates more extensive reactions between the chemical activation agents and the carbonaceous material. Higher temperatures promote enhanced pore

DOI: https://doi.org/10.22452/mjs.vol43sp1.1
Malaysian Journal of Science 43 (Special Issue 1): 1-7 (July 2024)

development, resulting in a more complete and optimized activation process.

Among the various combinations tested, that of KOH and urea as chemical activation agents at an activation temperature of 800°C yielded the most favorable results in terms of particle size. The resulting activated carbon exhibited an average pore diameter of 0.811 µm. This particle size is well-suited for applications requiring a well-defined pore structure, e.g., adsorption, gas separation, or catalysis.

The experimental findings demonstrate that the specific activation agents (KOH, urea, KOH + urea) had a limited impact on the pore diameter of the rice husk activated carbon. Alternatively, the rice husk material's structural properties tended to dominate in determining the pore size. The natural composition and

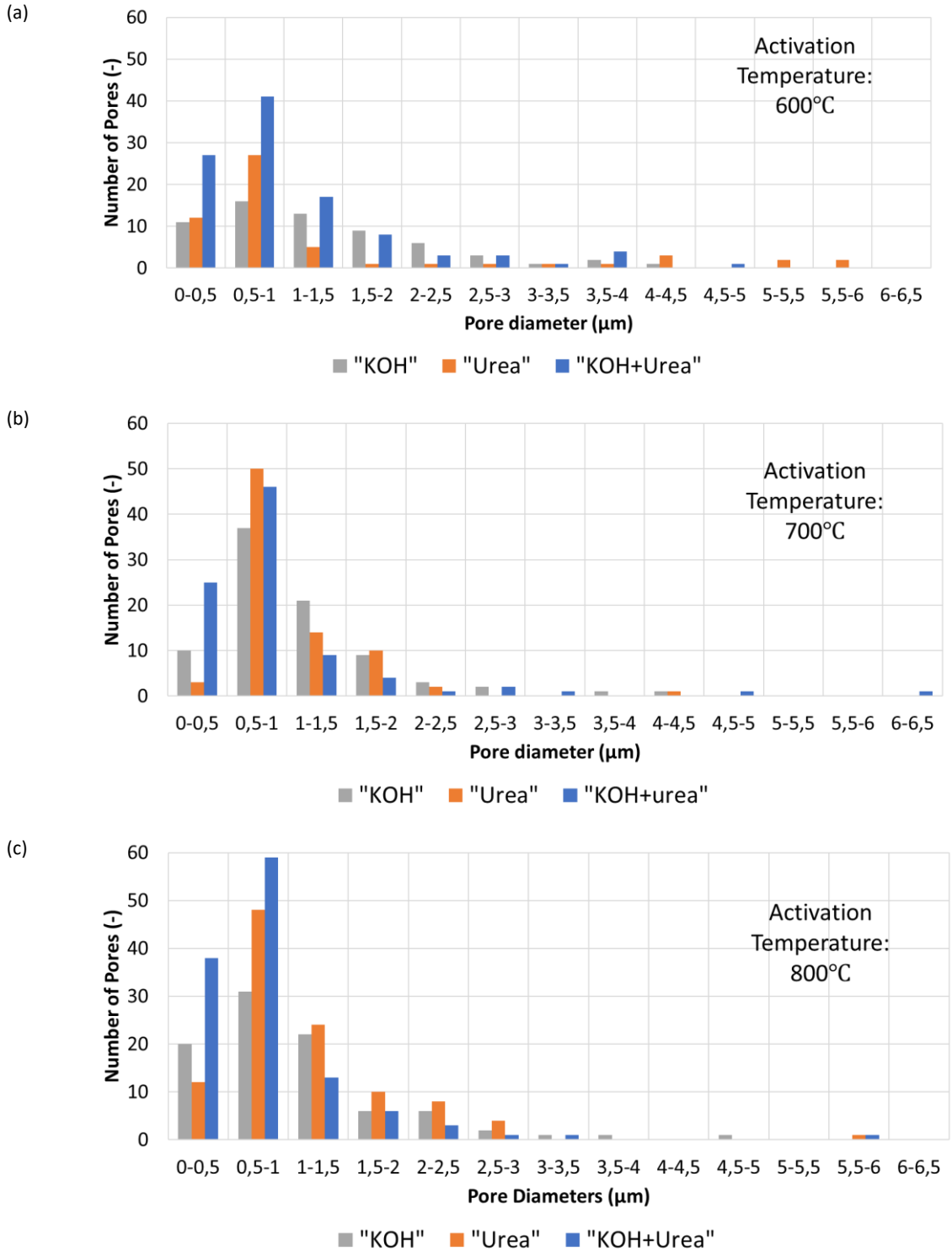

Figure 3. Effect of the chemical activating agent and activation temperatures on the pore number and size

DOI: https://doi.org/10.22452/mjs.vol43sp1.1
Malaysian Journal of Science 43 (Special Issue 1): 1-7 (July 2024)

arrangement of the rice husk's carbonaceous components strongly influenced the resulting pore size, regardless of the activation agents employed. In summary, the research demonstrates the significance of activation temperature in pore development, with higher temperatures leading to increased pore formation. The combination of KOH and urea as activation agents at 800°C yielded a desirable particle size for applications requiring a well-defined pore structure. These results show that variations in the combination of KOH and urea produce a more even pore distribution and higher pore density compared to other variations. The study highlights the importance of considering both the activation temperature and the inherent properties of the precursor material when optimizing pore characteristics in rice husk-activated carbon.

5. Acknowledgement

We thank the Research Institutions and Community Service of Andalas University for funding this research with contract number: T/5/UN16.19/PT.01.03/IS-RD/2023.

6. References

Cannone, S. F., Lanzini, A., & Santarelli, M. (2021). A review on CO_2 capture technologies with focus on CO_2-enhanced methane recovery from hydrates. Energies 14 (2): 1-32.

Deng, Y., Li, J., Miao, Y., & Izikowitz, D. (2021). A comparative review of performance of nanomaterials for Direct Air Capture. Energy Reports 7: 3506–3516.

Dissanayake, P. D., You, S., Igalavithana, A. D., Xia, Y., Bhatnagar, A., Gupta, S., Kua, H. W., Kim, S., Kwon, J. H., Tsang, D. C. W., & Ok, Y. S. (2020). Biochar-based adsorbents for carbon dioxide capture: A critical review. Renewable and Sustainable Energy Reviews 119(109582): 1-47.

Elhenawy, S. E. M., Khraisheh, M., Almomani, F., & Walker, G. (2020). Metal-organic frameworks as a platform for CO_2 capture and chemical processes: Adsorption, membrane separation, catalytic-conversion, and electrochemical reduction of CO_2. Catalysts 10(11): 1–33.

Goembira, F., Aristi, D. M., Nofriadi, D., & Putri, N. T. (2021). Analisis Konsentrasi PM2,5, CO, dan CO_2, serta Laju Konsumsi Bahan Bakar Biopelet Sekam Padi dan Jerami pada Kompor Biomassa. Jurnal Ilmu Lingkungan 19(2), 201–210.

Hussin, F., Aroua, M. K., Yusoff, R., & Szlachta, M. (2021). Preparation of eco-friendly adsorbent for enhancing CO_2 adsorption capacity. Separation Science and Technology 57(10): 1–15.

Jouhara, H., Ahmad, D., van den Boogaert, I., Katsou, E., Simons, S., & Spencer, N. (2018). Pyrolysis of domestic based feedstock at temperatures up to 300 °C. Thermal Science and Engineering Progress 5: 117–143.

Lee, J. W., Kim, S., Torres Pineda, I., & Kang, Y. T. (2021). Review of nanoabsorbents for capture enhancement of CO_2 and its industrial applications with design criteria. Renewable and Sustainable Energy Reviews 138 (110524): 1-18.

Lushpa, N. V, Lawah, A. I., Chernyakova, K. V., & Vrublevs, I. A. (2018). Using The ImageJ Software for Determining Parameters Of Microstructure Of Nanoporous Materials By The Results Of SEM Image Processing. Fourth International Scientific and Pratical Conference of Big Data and Advanced Analytics, Minsk, 3-4 May, pp 136-138, Republic of Belarus.

Rinawati, Hidayat, D., Supriyanto, R., Permana, D. F., & Yunita. (2019). Adsorption of Polycyclic Aromatic Hydrocarbons using Low-Cost Activated Carbon Derived from Rice Husk. Journal of Physics: Conference Series 1338(1): 1-8.

Segneri, V., Trinca, A., Libardi, N., Colelli, L., Micciancio, M., & Vilardi, G. (2023). Nanoparticles used for CO_2 Capture by Adsorption: a Review. Chemical Engineering Transactions, 101: 133–138.

Shi, X., Xiao, H., Azarabadi, H., Song, J., Wu, X., Chen, X., & Lackner, K. S. (2020). Sorbents for the Direct Capture of CO_2 from Ambient Air. In Angewandte Chemie - International Edition 59 (18): 6984–7006.

Wang, X., Chen, Y., Xu, W., Lindbråthen, A., Cheng, X., Chen, X., Zhu, L., & Deng, L. (2023). Development of high capacity moisture-swing DAC sorbent for direct air capture of CO_2. Separation and Purification Technology 324 (124489): 1-11.

Yaumi, A. L., Bakar, M. Z. A., & Hameed, B. H. (2018). Melamine-nitrogenated mesoporous activated carbon derived from rice husk for carbon dioxide adsorption in fixed-bed. Energy 155: 46–55.

Zhang, X., Huang, Y., Gao, H., Luo, X., Liang, Z., & Tontiwachwuthikul, P. (2019). Zeolite catalyst-aided tri-solvent blend amine regeneration: An alternative pathway to reduce the energy consumption in amine-based CO_2 capture process. Applied Energy 240: 827–841.

DOI: https://doi.org/10.22452/mjs.vol43sp1.1
Malaysian Journal of Science 43 (Special Issue 1): 1-7 (July 2024)

MALAYSIAN JOURNAL OF SCIENCE
MJS
ISSN 1394 - 3065

2nd Euro-Asia Conference on CO_2 Capture and Utilization (EACCO2CU2022)

Special issue

Malaysian Journal of Science 43 (Special Issue 1): 8-14 (July 2024)

https://mjs.um.edu.my

IMMOBILISATION OF COPPER (I) OXIDE/ZINC OXIDE NANOPARTICLES ON THE GAS DIFFUSION LAYER FOR CO_2 REDUCTION REACTION APPLICATION

Nor Hafizah Yasin[1a,b]* and Wan Zaireen Nisa Yahya[2a]

Abstract: The electrochemical reduction of carbon dioxide (CO_2RR) represents a promising strategy for CO_2 mitigation, requiring highly efficient catalysts integrated into electrochemical devices to achieve high conversion rates and energy efficiencies for desired products. Establishing a gas diffusion electrode is crucial for practical applications of CO_2 electrochemical reduction reactions (CO_2RR). This study uses the air-spraying method to immobilise nano-catalysts onto a gas diffusion layer (GDL) with exceptional homogeneity. A composite of copper(I) oxide (Cu_2O) and zinc oxide (ZnO) nanoparticles in a 4:1 ratio was deposited onto the GDL. Surface morphology analysis revealed the successful immobilisation of cubic Cu_2O and hexagonal wurtzite ZnO with a uniform distribution, indicating potential improvements in CO_2RR performance. Contact angle measurements were conducted to assess surface hydrophobicity, comparing pristine GDL with Cu_2O/ZnO-based GDL. Although the contact angle on the surface of the Cu_2O/ZnO-based GDL slightly reduced from 143.69° to 134.82°, it maintained its hydrophobic nature. This reduction is attributed to Nafion, a binder in the catalyst ink mixture. The sustained high contact angle is crucial for the CO_2 reduction reaction process. X-ray diffraction (XRD) diffractograms of Cu_2O/ZnO-based GDL were compared with reference Cu_2O, ZnO, and bare GDL. The presence of all essential peaks confirms the successful immobilisation. The air-spraying technique effectively achieved a favourable distribution of active metals.

Keywords: Cu_2O/ZnO, gas diffusion layer, immobilisation, CO_2 reduction reaction

1. Introduction

Carbon Carbon dioxide is categorized among greenhouse gases (GHG) and is a significant contributor primarily to fossil fuel combustion (Lin et al., 2020; Kim et al., 2015). It is a by-product of natural gas field monetisation within the oil and gas industry (Ahmad Zuhdi et al., 2021; Hassan et al., 2018). With the increasing demand for natural gas, there is a growing exploration of high-CO_2 fields to meet this need. However, the monetisation of high CO_2 fields has led to a rise in global carbon dioxide emissions, contributing to global warming. In response, PETRONAS has set a net-zero carbon emissions target by 2050, emphasizing the necessity for cleaner energy sources. Given the surge in environmental regulations addressing CO_2 emissions, gas field monetisation processes must prioritise fields with fewer contaminants. The depletion of such fields poses a challenge, necessitating urgent strategies to manage the extensive inventories of CO_2 by-products from high CO_2 fields (Hassan et al., 2018).

Effective monitoring of CO_2 emissions is achievable through adopting carbon capture, utilisation, and storage (CCUS). While sequestration remains a primary strategy for handling significant volumes of CO_2, this approach is characterised by its energy-intensive nature and potential costliness (Hassan et al., 2018; Qiao et al., 2014). In pursuit of alternative solutions, methods involving utilising and converting CO_2 are considered. These approaches aim to generate more value by producing higher outputs of valuable chemicals while concurrently minimising costs (Lin et al., 2020; Qiao et al., 2014).

Exploring reliable pathways such as photoelectrochemical, thermochemical, photocatalytic, and electrochemical routes for converting CO_2 into valuable products is crucial for mitigating global carbon emissions (Yuan et al., 2023; Qiao et al., 2014). Among these methods, the electrochemical route, known as the CO_2 reduction reaction (CO_2RR), stands out as a highly favourable technique. It reduces CO_2 emissions by transforming it into valuable products through heterogeneous electrochemical reduction principles (Lee et al., 2020; De Luna et al., 2018; Lee et al., 2015). CO_2 reduction occurs on the catalytic metal surface of the working electrode, involving two-, four-, six-, and eight-electron reductions, either in an H-cell or flow cell configuration (Yuan et al., 2023; Mowbray et al., 2021; Lin et al., 2020; Qiao et al., 2014). This method has been extensively investigated, yielding valuable products such as methane, carbon monoxide, ethanol, ethylene, formic acid, methanol, and propanol (Lin et al., 2020; Jouny et al., 2018; Qiao et al., 2014). With ongoing research, the prospects for extensive implementation of this technology appear promising.

Authors information:
[a]Department of Chemical Engineering, Universiti Teknologi PETRONAS, 32610 Bandar Seri Iskandar, Perak, Malaysia. E-mail: nor_21001482@utp.edu.my[1], zaireen.yahya@utp.edu.my[2]
[b]PETRONAS Research Sdn Bhd, Lot 3288 & 3289 Off Jalan Ayer Itam, Kawasan Institusi Bangi, 43000 Kajang, Selangor, Malaysia. E-mail: norhafizah.yasin@petronas.com[1]

*Corresponding Author: nor_21001482@utp.edu.my

Received: February 7, 2024
Accepted: May 7, 2024
Published: July 31, 2024

DOI: https://doi.org/10.22452/mjs.vol43sp1.2
Malaysian Journal of Science 43 (Special Issue 1): 8-14 (July 2024)

Ethylene, a highly versatile product generated through the CO_2 reduction reaction (CO_2RR) process, has significant market value and annual consumption. This chemical is a pivotal raw material in producing various items, including tyres, automotive products, textiles, paint, children's toys, and electronics. Despite the current lab-scale status of ethylene production technology, challenges such as limited ethylene selectivity over other by-products like H_2, resulting from the hydrogen evolution reaction (HER), carbon monoxide, CH_4, and other substances, coupled with drawbacks like a current density below 100 mA/cm² and electrolyser design, have hindered substantial progress toward commercialisation (Yuan et al., 2023). According to Lin et al., the electrochemical reduction technology must fulfil specific criteria to be deemed suitable for commercialisation (Lin et al., 2020). Feasibility for commercialisation hinges on process characteristics meeting certain benchmarks, including a current density within the range of 200-400 mA/cm², a 90% faradaic efficiency, a cell potential below 2.3 V, and a minimum of 30% conversion of CO_2 (Lin et al., 2020).

Since 1989, researchers have investigated the optimal working electrode for the CO_2RR. Copper-based electrodes have emerged as distinctive and efficient catalysts for converting CO_2 into hydrocarbons. While their efficiency has endured, there persists a demand for an active and selective catalyst that can generate specific products (Mok et al., 2023; Yuan et al., 2023; Chen et al., 2021; Chu et al., 2021). The quest for an effective catalyst demonstrating high activity and exceptional selectivity continues. Numerous copper-based working electrodes have been explored, including those with surface modifications geared towards ethylene production from CO_2, such as copper nanoparticles (NPs), copper wire, copper foil, copper oxide-based, bimetallic copper-based, copper-polymer, and copper-MOF (Strijevskaya et al., 2023; Yang et al., 2023; Chen et al., 2021; Chu et al., 2021; Tang et al., 2021; Ivan Merino-Garcia et al., 2019; Hoang et al., 2018; I. Merino-Garcia et al., 2018; Dohyung Kim et al., 2017; Reske et al., 2014). Kim et al. highlighted the efficacy of copper oxide nanoparticles for ethylene production, achieving a faradaic efficiency exceeding 65% (J. Kim et al., 2019). The nano-catalysts were deposited on a glassy carbon electrode and evaluated in a conventional H-cell configuration, with the current density limited to less than 50 mA/cm² due to mass transport limitations. To facilitate the assessment of CO_2RR at higher current densities of 200-400 mA/cm², the integration of the catalyst onto gas diffusion electrodes becomes imperative (Zhang et al., 2019).

This study involves the synthesis of nanosized copper(I) oxide and zinc oxide, applied through air-spraying onto a gas diffusion layer to create copper-based electrodes. In accordance with existing literature (Albo & Irabien, 2016), the inclusion of zinc contributes to the stabilisation of copper ions (Cu^+) and the elimination of impurities capable of deactivating the electrocatalyst. Moreover, zinc has the potential to mitigate hydrogen formation during the hydrogen evolution reaction (HER), thereby enhancing the overall performance of CO_2 conversion (Merino-Garcia et al., 2019; Keerthiga & Chetty, 2017). There is a gap in the catalyst immobilisation technique on the gas diffusion layer for use in CO_2RR. Previous researchers focused more on the catalyst and CO_2RR performance compared to the catalyst immobilisation, which is a vital procedure in producing an effective working electrode. With detailed steps, this paper aims to assess the effectiveness of immobilising Cu_2O/ZnO-based gas diffusion layers using the air-spraying technique and characterise the resulting working electrode for potential application in the CO_2RR. The primary objective is to enhance the catalytic efficiency of the gas diffusion layer-based working electrode, particularly when employed in a liquid-flowing system. This enhancement aims to increase the selectivity for ethylene production and improve overall energy efficiency within a CO_2 electroreduction system.

2. Experimental

2.1 Synthesis Preparation of Cu_2O Nanoparticles

Cubic copper(I) oxide (Cu_2O) nanoparticles (NP) were synthesized by dissolving 6g of copper(II) nitrate trihydrate in 30 mL of ethylene glycol with vigorous stirring, heated to 120°C for 20 minutes. The copper solution was then poured into a Teflon-lined sealed reactor. The temperature was gradually increased to a crystal growth temperature of 180°C in an oven and maintained for 7 hours to induce cubic morphology, following the procedure outlined by Jung et al. (Jung et al., 2019). The solution was then cooled to ambient temperature, and the resulting precipitate was subjected to centrifugation and washed multiple times with distilled water and isopropyl alcohol until a clear solution was achieved. The obtained powder was dried overnight at 100°C. The Cu_2O nanoparticle powder was securely stored in a clean and dry Duran bottle for subsequent use.

2.2 Synthesis Preparation of ZnO Nanoparticles

Zinc oxide (ZnO) nanoparticles were synthesized using a modified polyol chemistry method tailored to the available laboratory facilities, following the approach outlined by Mahamuni et al. with modification (Mahamuni et al., 2019). To initiate the synthesis, 6 g of zinc acetate dihydrate was dissolved in 100 mL of triethylene glycol with vigorous stirring, and the mixture was heated to 80°C for 0100 hours. Subsequently, the zinc solution was transferred into a Teflon-lined sealed reactor, and the temperature was gradually increased to 220°C using an oven, maintaining this temperature for 0500 hours. The reaction resulted in the formation of a white precipitate, which was then subjected to centrifugation and washed multiple times with distilled water and ethanol until a clear solution was achieved. The obtained powder was dried overnight at 100°C, and the resulting ZnO nanoparticle powder was stored in a clean and dry Duran bottle for subsequent use.

2.3 Immobilisation of Cu_2O/ZnO Nanoparticles on Gas Diffusion Layer (GDL)

Cu_2O NPs and ZnO NPs were combined in a 4:1 ratio to study the effect of ZnO on the CO_2 reduction performance. Sigracet 39BB carbon paper served as the gas diffusion layer, providing support for the immobilisation of Cu_2O/ZnO. The catalytic ink was formulated by dispersing Cu_2O/ZnO NPs in a 5% Nafion solution, which served as a binder, with isopropyl alcohol (IPA) as the ink deposition carrier. This process followed the methodology outlined in previous studies (Guzman et al., 2021; Jung et al., 2019

DOI: https://doi.org/10.22452/mjs.vol43sp1.2
Malaysian Journal of Science 43 (Special Issue 1): 8-14 (July 2024)

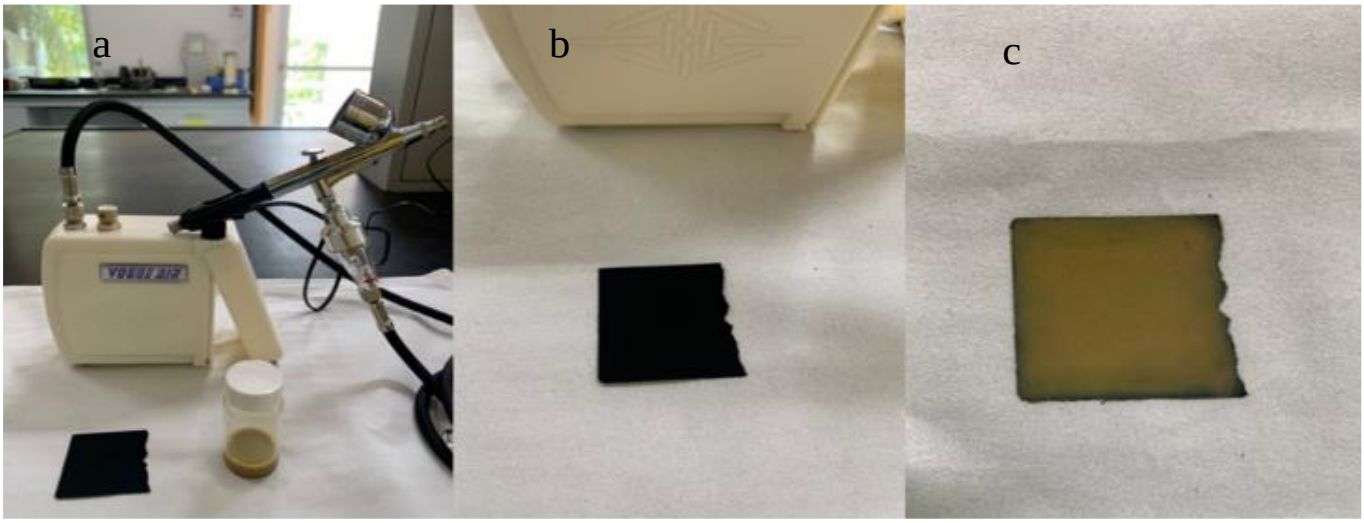

Figure 1. The Setup of a) Air-spraying System for Immobilisation of Cu_2O/ZnO-based GDL, b) neat Gas Diffusion Layer, c) Cu_2O/ZnO-based GDL

I. Merino-Garcia et al., 2018). A mass ratio of 50:50 Cu_2O/ZnO NP with 5 wt% nafion solution was established as the baseline. The solution underwent ultrasonication for 1 hour at ambient temperature to ensure optimal homogeneity. The catalytic layer was then immobilised by spraying the catalyst ink onto the GDL surface and allowing it to dry in an oven for one hour. Figure 1 illustrates the setup of the air-spraying equipment and the colour change of the GDL before and after the immobilisation of Cu_2O/ZnO on its surface.

2.4 Catalyst Characterization

Characterizing Cu_2O/ZnO nanoparticles on the gas diffusion layer (GDL) is essential for evaluating the catalyst's properties. Various characterization methods were employed, as outlined below. A Theta Lite Optical Tensiometer determined the hydrophobicity and hydrophilicity of the gas diffusion electrode (GDE) surface surface. One centimetre (cm) samples of both the pristine GDL and Cu_2O/ZnO-based GDL were tested. Hydrophobicity was assessed by dropping distilled water on the GDE surface and measuring the contact angle. A Hitachi SU8020 Field Emission Scanning Electron Microscope coupled with Energy Dispersive X-Ray (FESEM-EDX) was utilized to examine the surface morphology of the pristine GDL and Cu_2O/ZnO-based GDL. Both surface and cross-sectional morphologies of the bare GDL and modified GDL were analyzed for structural comparisons at 10K and 40K magnifications. Simultaneously, EDX was employed to identify the elemental compositions and distribution of active metals on the surface and cross-section of the Cu_2O/ZnO-based GDL. For an in-depth analysis of inorganic and nanomaterial phase purity as well as crystallinity properties, X-ray diffraction (XRD) was performed using the Shimadzu XRD-7000 over a range of 30-80 2θ. This technique was applied to both the pristine GDL paper and the Cu_2O/ZnO-based GDL.

3. Results & discussion

3.1 Hydrophobicity of the Cu_2O/ZnO Immobilized on GDL

The contact angle measurement is imperative for assessing surface hydrophobicity and hydrophilicity, providing insight into a liquid's ability to wet a solid surface. A surface is categorized as hydrophobic if its angle exceeds 90°, while an angle below 90° denotes hydrophilicity. Figure 2 displays the contact angles of the pristine GDL and the GDL modified with Cu_2O/ZnO. The average contact angle for the pristine GDL is 143.69°, whereas the Cu_2O/ZnO-based GDL exhibits a reduced angle of 134.82°, indicating a decrease of approximately 6%. Despite this reduction, the surface remains classified as hydrophobic.

This reduction in contact angle may be attributed to the presence of Nafion ionomers acting as binders, which enhance catalyst utilization by promoting ionic connectivity. The Nafion ionomer presents a dual advantage by aiding in the binding of metals to the gas diffusion layer and concurrently enhancing ionic conduction (Ramasamy, 2020). However, the inherently hydrophilic nature of Nafion results in an elevated water content within the pores (Kibria et al., 2019). The preservation of high hydrophobicity is crucial for the success of this technology, as it prevents the flooding of the gas diffusion layer. Flooding could adversely impact the mass transfer of CO_2 to the catalyst layer during experimental runs (Guzman et al., 2021; Mowbray et al., 2021; Lin et al., 2020).

Burdyny and Smith (2019) discovered that the elevated hydrophobicity of the electrocatalyst on the gas diffusion layer played a significant role in enhancing CO_2 reduction efficiency and bolstering the stability of the GDL. The hydrophilic and hydrophobic conditions at the working electrode significantly influence the products generated during CO_2 reduction. A hydrophobic environment fosters the hydrocarbon reaction pathway, leading to enhanced C-C hydrocarbon coupling and thus boosting the formation of ethylene (Chang et al., 2022).

DOI: https://doi.org/10.22452/mjs.vol43sp1.2
Malaysian Journal of Science 43 (Special Issue 1): 8-14 (July 2024)

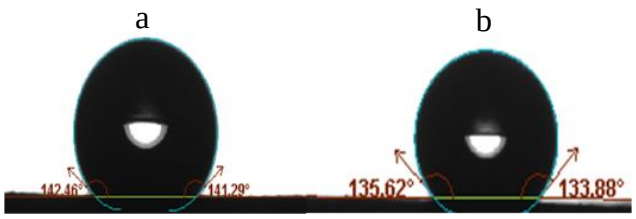

Figure 2. Contact Angle of a) GDL b) immobilized Cu_2O/ZnO-based GDL

3.2 Morphology of the Cu_2O/ZnO Immobilized on GDL

A comparative analysis of FESEM images was conducted at varying magnifications to examine the cross-sectional and surface morphology of both pristine GDL and GDL modified with immobilized Cu_2O/ZnO. Figures 3(a), (b), (e), and (f) depict the cross-sectional views of the pristine GDL and Cu_2O/ZnO-based GDL, respectively. Meanwhile, Figures 3(c), (d), (g), and (h) showcase the surface morphology at magnifications of 10K and 40K.

The results indicate the successful immobilisation of Cu_2O/ZnO nanoparticles on the pristine GDL surface. The catalyst was incorporated into a Nafion solution, serving as a binder, with isopropyl alcohol (IPA) acting as the catalyst carrier during the

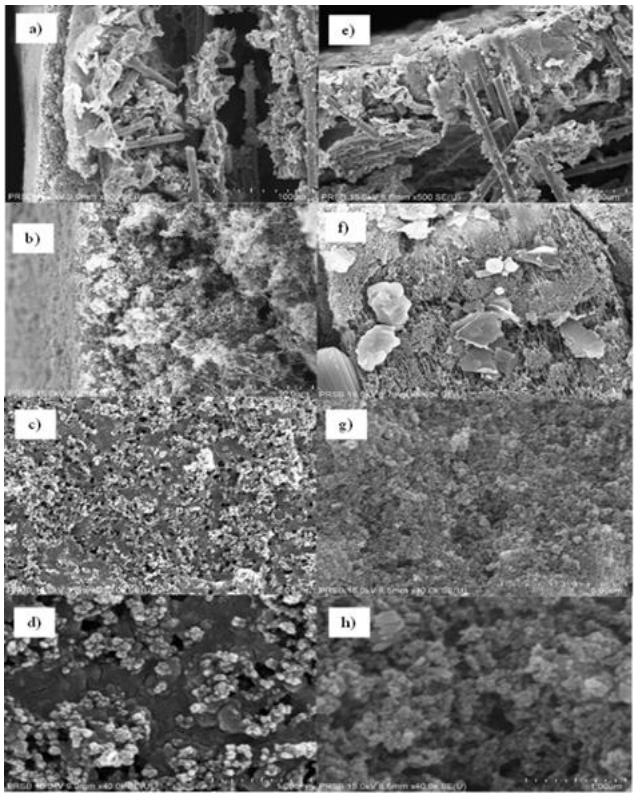

Figure 3. Cross-section and Surface Morphology of a-d) GDL, e-h) Cu_2O/ZnO-based GDL

immobilisation process, following protocols outlined by Guzman et al., Jung et al., and Merino-Garcia et al. (Guzman et al., 2021; Jung et al., 2019; I. Merino-Garcia et al., 2018). The Cu_2O/ZnO nanoparticles were effectively deposited, providing homogeneous coverage over the GDL surface. Notably, the surface morphologies of the immobilised GDL revealed the cubic shape of Cu_2O and the hexagonal shape of ZnO at both 10K and 40K magnifications.

3.3 Elemental Composition of the Cu_2O/ZnO Immobilized on GDL

Figure 4 depicts the Energy Dispersive X-ray (EDX) spectrum of the gas diffusion layer (GDL), revealing the presence of carbon, fluorine, and oxygen elements. The GDL comprises two primary layers. The first is a microporous layer designed to provide mechanical stability and electrical contact, facilitating gas distribution through macroscale pores composed of carbon structure paper (Kibria et al., 2019). According to Liang et al. (2020), the inclusion of a catalyst in the composition of the GDL prolongs the retention time on the electrode surface, thereby enhancing mass transport and resulting in an augmented current density for CO_2RR.

The second layer, situated between the microporous and catalyst layers, is also microporous and serves to enhance interfacial electrical connectivity while preventing flooding. This is achieved through a combination of carbon black nanoparticles and a hydrophobic polymer mixture. The presence of fluorine is attributed to the inclusion of polytetrafluoroethylene (PTFE) in the GDL compound mixture. PTFE enhances the hydrophobic nature of the GDL, mitigating the risk of flooding during electroreduction reactions.

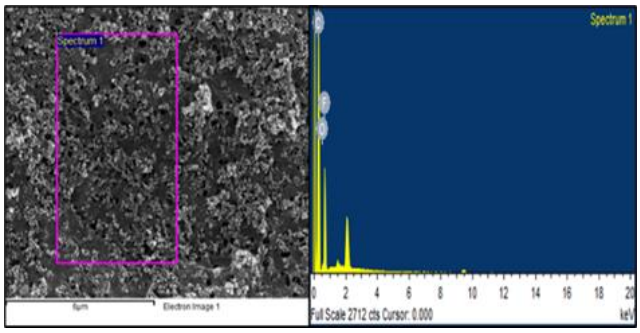

Figure 4. Energy Dispersive X-ray (EDX) Spectrum of GDL

Figure 5 presents the Energy Dispersive X-ray (EDX) spectrum of Cu_2O/ZnO-based GDL. The spectrum reveals the presence of Cu, O, and Zn elements, confirming that the Cu_2O and ZnO compounds were effectively immobilized onto the GDL substrate. The homogeneous distribution of Cu, Zn, and O elements across the gas diffusion layer was achieved using the air-spraying technique. Jhong et al. (2013) similarly observed that the air-spraying method results in a more uniform catalyst layer, thereby contributing to improved performance.

Element mapping is employed to assess Cu_2O/ZnO dispersion uniformity on the GDL. In Figure 6, the oxygen atoms are denoted by red dots, copper by blue dots, and zinc by green dots, indicating their distribution on the GDL. The surface crack observed on the catalyst on the GDL is due to the slow evaporation rate of the solvent from the catalyst ink solution during immobilisation. This aspect can be improved by immobilising catalysts on a heated surface, such as a hot plate operating at temperatures ranging from 60 to 80°C.

DOI: https://doi.org/10.22452/mjs.vol43sp1.2
Malaysian Journal of Science 43 (Special Issue 1): 8-14 (July 2024)

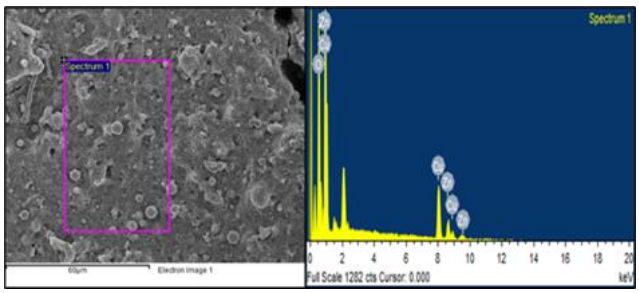

Figure 5. Energy Dispersive X-ray (EDX) Spectrum of Cu_2O/ZnO-based GDL

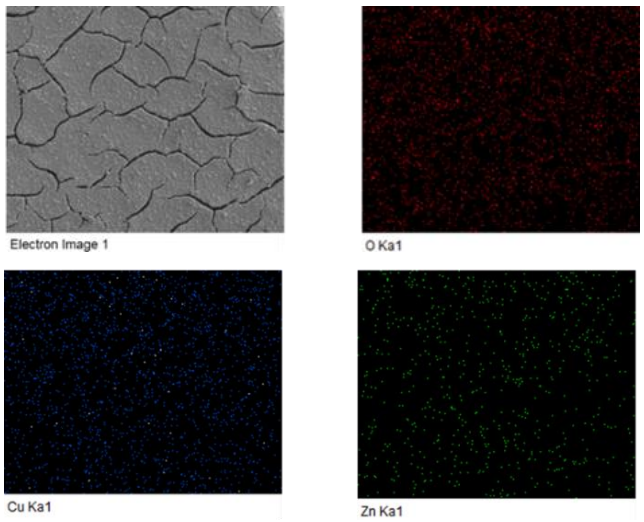

Figure 6: Elements Mapping of Cu_2O/ZnO-based GDL

3.4 Crystalline Structure of Cu_2O/ZnO Immobilized on GDL

Figure 7 illustrates the X-ray diffraction (XRD) patterns of pristine GDL and GDL modified with Cu_2O/ZnO, validating the crystalline structures of the deposited nanoparticles. The XRD diffractogram of Cu_2O/ZnO-based GDL was compared with the pristine GDL, standard Cu_2O (JCPDS 01-078-2078), and ZnO (JCPDS 00-036-1451) patterns to elucidate the crystal structure of these compounds.

The XRD analysis revealed distinct diffraction peaks for the pristine GDL at 37.9°, 44.1°, 54.2°, 64.4°, and 77.5°, as depicted in Figure 7. The immobilized Cu_2O/ZnO-based GDL exhibited all crucial diffraction peaks associated with the Cu_2O cubic crystalline structure (111), (200), and (220) at 36.4°, 42.3°, 52.5°, 61.4°, 65.6°, 69.6°, 73.6°, and 77.4°. This observation aligns with the results reported by Jung et al. (2019), who identified face-centered cubic Cu_2O.

Furthermore, the hexagonal wurtzite crystal structures of ZnO, specifically (100), (002), (101), and (110), were observed on the Cu_2O/ZnO-based GDL surface at 31.8°, 34.4°, 36.3°, 47.5°, 56.6°, 62.9°, 66.4°, 67.9°, 69.1°, 72.6°, and 76.9°. The compilation of prominent diffraction peaks corresponding to GDL, Cu_2O, and ZnO in the XRD pattern for Cu_2O/ZnO-based GDL serves as conclusive evidence, affirming the successful immobilisation of the nanocatalyst onto the GDL substrate.

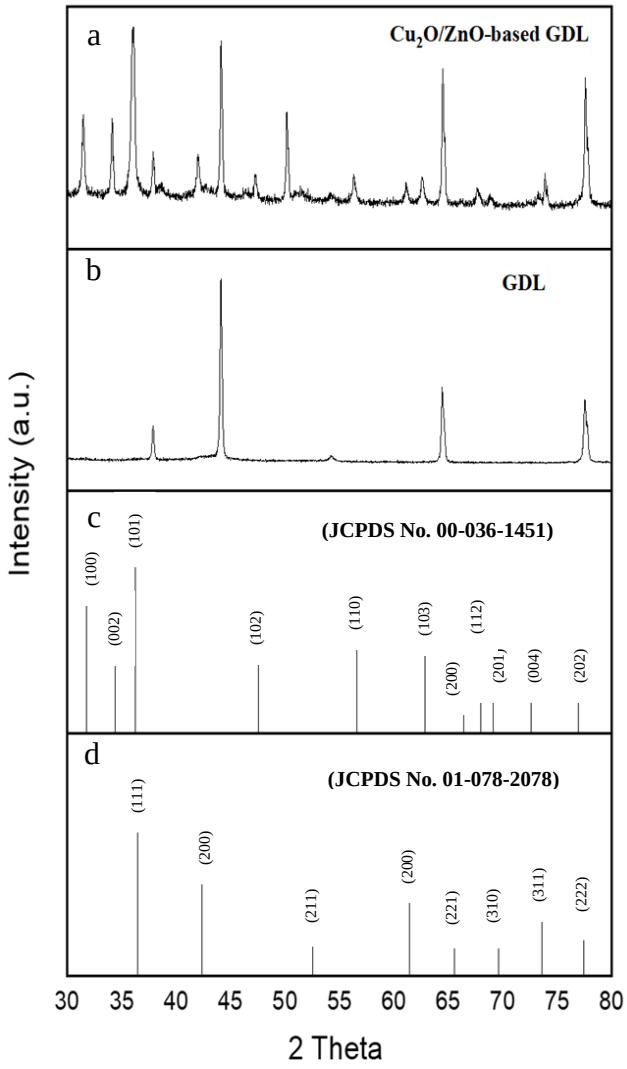

Figure 7. X-ray Diffraction (XRD) Pattern of a) Cu_2O/ZnO-based GDL, b) neat GDL, c) Reference ZnO, d) Reference Cu_2O

4. Conclusion

The deployment of the air-spraying technique for immobilizing Cu_2O/ZnO nanoparticles on the gas diffusion layer (GDL) has been effectively implemented. Detailed examinations of the working electrode's surface morphology, textural properties, and phase characteristics were conducted. The Cu_2O nanoparticles display a cubic structure, while ZnO manifests a hexagonal wurtzite shape, with both uniformly deposited across the gas diffusion layer. The introduction of the Nafion binder resulted in a slight decrease in the hydrophobicity of the Cu_2O/ZnO-based GDL compared to the pristine GDL. Nonetheless, the hydrophobicity level remains acceptable, effectively mitigating the risk of flooding at the working electrode during the liquid flow system's CO_2 reduction reaction process. Projected as an exceptional electrocatalyst for CO_2 reduction reactions, the Cu_2O/ZnO nanoparticle gas diffusion electrode shows considerable potential for future applications.

DOI: https://doi.org/10.22452/mjs.vol43sp1.2
Malaysian Journal of Science 43 (Special Issue 1): 8-14 (July 2024)

5. Acknowledgement

The authors acknowledge the support provided by PETRONAS Research Sdn. Bhd. (PRSB) and Universiti Teknologi PETRONAS (UTP).

6. References

Ahmad Zuhdi, M. F., Rahman, F. H., Shahjavan, H., Mas'od, M. A., Salihuddin, R. S., Zulkepli, N. A., Alias, A., Jalani, M. Y., & Yiin, T. K. (2021). Feasibility Study of Offshore Hybrid Technology for High CO2 Gas Field Monetization. Proceedings of International Petroleum Technology Conference, March, Virtual.

Albo, J., & Irabien, A. (2016). Cu2O-loaded gas diffusion electrodes for the continuous electrochemical reduction of CO2 to methanol. In Journal of Catalysis 343: 232–239.

Burdyny, T., & Smith, W. A. (2019). CO2 reduction on gas-diffusion electrodes and why catalytic performance must be assessed at commercially-relevant conditions. Energy and Environmental Science 12(5): 1442–1453.

Chang, Q., Lee, J. H., Liu, Y., Xie, Z., Hwang, S., Marinkovic, N. S., Park, A. H. A., Kattel, S., & Chen, J. G. (2022). Electrochemical CO2Reduction Reaction over Cu Nanoparticles with Tunable Activity and Selectivity Mediated by Functional Groups in Polymeric Binder. JACS Au 2(1): 214–222.

Chen, X., Chen, J., Alghoraibi, N. M., Henckel, D. A., Zhang, R., Nwabara, U. O., Madsen, K. E., Kenis, P. J. A., Zimmerman, S. C., & Gewirth, A. A. (2021). Electrochemical CO2-to-ethylene conversion on polyamine-incorporated Cu electrodes. Nature Catalysis 4(1): 20–27.

Chu, M., Chen, C., Wu, Y., Yan, X., Jia, S., Feng, R., Wu, H., He, M., & Han, B. (2021). Enhanced CO2 electroreduction to ethylene via strong metal-support interaction. Green Energy and Environment 7(4): 792-798.

De Luna, P., Quintero-Bermudez, R., DInh, C. T., Ross, M. B., Bushuyev, O. S., Todorović, P., Regier, T., Kelley, S. O., Yang, P., & Sargent, E. H. (2018). Catalyst electro-redeposition controls morphology and oxidation state for selective carbon dioxide reduction. Nature Catalysis 1(2): 103–110.

Guzman, H., Zammillo, F., Roldan, D., Galleti, C., Russo, N., & Hernandez, S. (2021). Investigation of Gas Diffusion Electrode Systems for the Electrochemical CO2 Conversion. Catalysts 11(4): 482.

Hassan, H., Omar, N. F. N., Jalil, A. A. M. M., Salihuddin, R. S., & Shah, S. S. M. (2018). Gearing toward CCUS for CO2 reduction in Malaysia. Proceedings of Offshore Technology Conference Asia March, Kuala Lumpur.

Hoang, T. T. H., Verma, S., Ma, S., Fister, T. T., Timoshenko, J., Frenkel, A. I., Kenis, P. J. A., & Gewirth, A. A. (2018). Nanoporous Copper-Silver Alloys by Additive-Controlled Electrodeposition for the Selective Electroreduction of CO2 to Ethylene and Ethanol. Journal of the American Chemical Society 140(17): 5791–5797.

Jhong, H. R. Q., Brushett, F. R., & Kenis, P. J. A. (2013). The effects of catalyst layer deposition methodology on electrode performance. Advanced Energy Materials 3(5): 589–599.

Jouny, M., Luc, W., & Jiao, F. (2018). General Techno-Economic Analysis of CO2 Electrolysis Systems. Industrial and Engineering Chemistry Research 57(6): 2165–2177.

Jung, H., Lee, S. Y., Lee, C. W., Cho, M. K., Won, D. H., Kim, C., Oh, H. S., Min, B. K., & Hwang, Y. J. (2019). Electrochemical Fragmentation of Cu 2 O Nanoparticles Enhancing Selective C-C Coupling from CO 2 Reduction Reaction. Journal of the American Chemical Society 141(11): 4624–4633.

Keerthiga, G., & Chetty, R. (2017). Electrochemical Reduction of Carbon Dioxide on Zinc-Modified Copper Electrodes. Journal of The Electrochemical Society 164(4): 164–169.

Kibria, M. G., Edwards, J. P., Gabardo, C. M., Dinh, C. T., Seifitokaldani, A., Sinton, D., & Sargent, E. H. (2019). Electrochemical CO2 Reduction into Chemical Feedstocks: From Mechanistic Electrocatalysis Models to System Design. Advanced Materials31(31): 1–24.

Kim, Dahee, Lee, S., Ocon, J. D., Jeong, B., Lee, J. K., & Lee, J. (2015). Insights into an autonomously formed oxygen-evacuated Cu2O electrode for the selective production of C2H4 from CO2. Physical Chemistry Chemical Physics 17(2): 824–830.

Kim, Dohyung, Kley, C. S., Li, Y., & Yang, P. (2017). Copper nanoparticle ensembles for selective electroreduction of CO2 to C2–C3 products. Proceedings of the National Academy of Sciences, 15 August, pp. 10560–10565 United States of America.

Kim, J., Choi, W., Park, joon woo, Kim, C., Kim, M., & Song, H. (2019). Branched Copper Oxide Nanoparticles Induce Highly Selective Ethylene Production by Electrochemical Carbon Dioxide Reduction 141(17): 6986-6994.

Lee, M. Y., Park, K. T., Lee, W., Lim, H., Kwon, Y., & Kang, S. (2020). Current achievements and the future direction of electrochemical CO2 reduction: A short review. Critical Reviews in Environmental Science and Technology 50(8): 769–815.

Lee, S., Kim, D., & Lee, J. (2015). Electrocatalytic production of C3-C4 compounds by conversion of CO2 on a chloride-induced Bi-phasic Cu2O-Cu catalyst. Angewandte Chemie - International Edition 54(49): 14701–14705.

Liang, S., Altaf, N., Huang, L., Gao, Y., & Wang, Q. (2020). Electrolytic cell design for electrochemical CO2 reduction. Journal of CO2 Utilization 35: 90–105.

Lin, R., Guo, J., Li, X., Patel, P., & Seifitokaldani, A. (2020). Electrochemical reactors for CO2 conversion. In Catalysts 10(5): .

DOI: https://doi.org/10.22452/mjs.vol43sp1.2
Malaysian Journal of Science 43 (Special Issue 1): 8-14 (July 2024)

Mahamuni, P. P., Patil, P. M., Dhanavade, M. J., Badiger, M. V., Shadija, P. G., Lokhande, A. C., & Bohara, R. A. (2019). Using polyol chemistry for their antimicrobial and antibiofilm activity. Biochemistry and Biophysics Reports 17:71–80.

Merino-Garcia, I., Albo, J., & Irabien, A. (2018). Tailoring gas-phase CO2 electroreduction selectivity to hydrocarbons at Cu nanoparticles. Nanotechnology 29(1):014001.

Merino-Garcia, Ivan, Albo, J., Solla-Gullón, J., Montiel, V., & Irabien, A. (2019). Cu oxide/ZnO-based surfaces for a selective ethylene production from gas-phase CO2 electroconversion. Journal of CO2 Utilization 31: 135–142.

Mok, D. H., Li, H., Zhang, G., Lee, C., Jiang, K., & Back, S. (2023). Data-driven discovery of electrocatalysts for CO2 reduction using active motifs-based machine learning. Nature Communications, 14(7303): 1-12.

Mowbray, B. A. W., Dvorak, D. J., Taherimakhsousi, N., & Berlinguette, C. P. (2021). How Catalyst Dispersion Solvents Affect CO2Electrolyzer Gas Diffusion Electrodes. Energy and Fuels 35(23): 19178–19184.

Qiao, J., Liu, Y., Hong, F., & Zhang, J. (2014). A review of catalysts for the electroreduction of carbon dioxide to produce low-carbon fuels. In Chemical Society Reviews 43(2): 631-675.

Ramasamy, R.P. (2020). Membrane Electrode Assemblies, pp. 787–805, Elsevier B.V.

Reske, R., Mistry, H., Behafarid, F., Roldan Cuenya, B., & Strasser, P. (2014). Particle size effects in the catalytic electroreduction of CO2 on Cu nanoparticles. Journal of the American Chemical Society 136(19): 6978–6986.

Strijevskaya, A., Yamaguchi, A., Shoji, S., Ueda, S., Hashimoto, A., Wen, Y., Wardhana, A. C., Lee, J. E., Liu, M., Abe, H., & Miyauchi, M. (2023). Nanophase-Separated Copper-Zirconia Composites for Bifunctional Electrochemical CO2 Conversion to Formic Acid. ACS Applied Materials and Interfaces 15(19): 23299–23305.

Tang, Z., Nishiwaki, E., Fritz, K. E., Hanrath, T., & Suntivich, J. (2021). Cu(I) Reducibility Controls Ethylene vs Ethanol Selectivity on (100)-Textured Copper during Pulsed CO2Reduction. ACS Applied Materials and Interfaces 13(12): 14050–14055.

Yang, H., Chuai, H., Meng, Q., Wang, M., Zhang, S., & Ma, X. (2023). Copper-based bimetallic electrocatalysts for CO2 reduction: From mechanism understandings to product regulations. Materials Reports: Energy 3(1): 100174.

Yuan, L., Zeng, S., Zhang, X., Ji, X., & Zhang, S. (2023). Advances and challenges of electrolyzers for large-scale CO2 electroreduction. Materials Reports: Energy 3(1): 100177.

Zhang, J., Luo, W., & Zuttel, A. (2019). Self-supported copper-based gas diffusion electrodes for CO2 electrochemical reduction. Journal of Materials Chemistry A 46: 1–9.

DOI: https://doi.org/10.22452/mjs.vol43sp1.2
Malaysian Journal of Science 43 (Special Issue 1): 8-14 (July 2024)

MALAYSIAN JOURNAL OF SCIENCE
MJS
ISSN 1394 - 3065

2nd Euro-Asia Conference on CO_2 Capture and Utilization (EACCO2CU2022) Special issue

Malaysian Journal of Science 43 (Special Issue 1): 15-19 (July 2024) https://mjs.um.edu.my

EXPERIMENTAL INVESTIGATION OF AMINE-BASED GRAPHENE NANOSUSPENSION FOR CO_2 ABSORPTION

Nur Azni Farhana Mazri[1a], A Arifutzzaman[2b*], Mohamed Kheireddine Aroua[3a,c]

Abstract: Absorption is the most widely used carbon dioxide (CO_2) removal technology. The CO_2 absorption performance of monoethanolamine (MEA), the most commonly used CO_2 absorbent, can be improved by suspending nanoparticles. This work examined the performance of graphene nanoplatelets (GNPs) as additives to enhance CO_2 absorption in MEA. The GNPs were characterized by HRTEM, FTIR, and XRD. The study examined the influence of GNP concentrations on CO_2 absorption at room temperature. The images from HRTEM confirmed that the implemented graphene consists of several layers of graphene sheets. Increasing the loading of particles increased the solubility of CO_2 until the optimum concentration was reached. From this work, it is evident that incorporating GNPs into MEA enhances the CO_2 absorption performance of MEA. Thus, the addition of nanoparticles to the absorbent can enhance its CO_2 absorptivity.

Keywords: 2D Nanomaterials, Graphene, Nanosuspensions, Amine, CO_2 absorption.

1. Introduction

Absorption is one of the methods used for acid gas removal. Carbon dioxide (CO_2), one of the acidic gases, is derived from natural sources and anthropogenic emissions. CO_2 absorption is one of the techniques used for post-combustion CO_2 capture. Ochedi et al. (Ochedi, Yu, Yu, Liu, & Hussain, 2021) mentioned that the capability, experience, and reliability of the technique make it the most promising CO_2 capture technology. Monoethanolamine (MEA), a primary amine, has been extensively used and studied as a CO_2 absorbent. One mole of CO_2 will react with two moles of amines to form carbamate, as shown by the following equation:

$$CO_2 + 2RNH_2 \leftrightarrow RNHCOO^- + RNH_3^+ \quad (1)$$

The disadvantages of MEA include corrosivity, high toxicity, regeneration energy requirements, vapor pressure and volatility, low CO_2 capacity, and the need for additional operational equipment, which undermine the effectiveness of MEA (Hamidi, Farsi, & Eslamloueyan, 2018; Ramezani, Mazinani, & Di Felice, 2021; Seo, Lages, & Kim, 2020). An ideal absorption solvent should have high CO_2 capacity, chemical and thermal stability, fast reaction rates, and low absorption heat, regeneration energy, toxicity, and volatility (Hamidi et al., 2018; Ramezani et al., 2021). In this regard, nanofluid is one of the approaches identified to overcome the problem. Suspension of nanoparticles in a base fluid produces nanofluid.

Several studies have shown that adding nanoparticles can enhance CO_2 capture. Seo et al. (Seo et al., 2020) employed a nickel nanoparticles-MEA system for CO_2 absorption in two microfluidic platforms: a microreactor and a long serpentine channel. They reported an increase of 34% and 54% in the rate of CO_2 absorption in the microreactor and long serpentine channel, respectively. $TiO(OH)_2$ has also been reported to accelerate the CO_2 absorption of MEA (Lai et al., 2018). Mohammadpour et al. (Mohammadpour, Mirzaei, & Azimi, 2019) employed a dimensionless number system to quantify the effect of additives on the CO_2 absorption of MEA. Among the carbon additives used in the study, graphene oxide (GO) showed the most significant impact on enhancing solubility and mass transfer rate. Source (Rahimi, Riahi, & Abbasi, 2020) suspended pristine and modified carbon nanotubes (CNTs) in different base fluids, where all types of CNT addition increased CO_2 absorption. In the GO-SDS-MEA system (mohammadpoor, Mirzaei, Azimi, & ghomshe, 2018), the addition of GO increased the mass transfer coefficient and CO_2 molecular diffusion, with a linear relationship with temperature and an inverse relationship with pressure.

In this work, we evaluated the performance of graphene nanoplatelets (GNPs) as additives to enhance CO_2 absorption in MEA. The influence of the volume fraction of GNPs at room temperature was investigated. To eliminate the influence of dispersants, the GNP-MEA nanofluids were prepared using the ultrasonic dispersion method without adding any dispersant.

Authors information:
[a]*Centre for Carbon Dioxide Capture and Utilization (CCDCU), School of Science and Technology, Sunway University, No. 5, Jalan Universiti, Bandar Sunway, 47500 Petaling Jaya, Selangor, Malaysia. Email:* kheireddinea@sunway.edu.my[3]
[b]*Tyndall National Institute, University College Cork, Lee Maltings, Cork, T12 R5CP, Ireland. Email:* arifutzzaman.rahat@tyndall.ie[2]
[c]*School of Engineering, Lancaster University, Lancaster LA1 4YW, United Kingdom. Email:* kheireddinea@sunway.edu.my[3]

*Corresponding author: arifutzzaman.rahat@tyndall.ie[2], kheireddinea@sunway.edu.my[3]

Received: February 7, 2024
Accepted: May 7, 2024
Published: July 31, 2024

DOI: https://doi.org/10.22452/mjs.vol43sp1.3
Malaysian Journal of Science 43 (Special Issue 1): 15-19 (July 2024)

2. Methodology

2.1. Materials

This study used GNPs (Sigma-Aldrich), MEA (Merck), CO_2 (Alpha Gas Solution, Malaysia), and deionized water (DW).

2.2. Synthesis of Nanofluids

The nanofluids used in this study were prepared using the two-step method, where the nanoparticles were introduced into the base fluid. The stock solution of the base fluid was prepared by stirring a mixture of MEA and DW for 30 min. The GNPs needed were then measured so that the resultant nanofluids would have the following volume fractions (ϕ): 0.01, 0.03, and 0.05. Before the nanofluids were sonicated for 1 h via an ultrasonic bath, where the sonication process was conducted for 15 min for each session, the GNP-MEA dispersions were stirred for 30 min. The temperature of the sonication process was kept constant at 25 ± 2 °C throughout the process. No dispersing agent was used in the preparation to prevent any interference with CO_2 absorption.

3. Characterization

3.1 High-Resolution Transmission Electron Microscope

A FEI-Tecnai G^2 20 S-Twin high-resolution transmission electron microscope (HRTEM) was employed to analyze the morphologies and geometric specifications of the GNPs. The preparation of the sample involves 20-min sonication of 1 mg of GNP suspension in isopropyl alcohol, followed by overnight air-drying on a copper grid (Formvar-carbon coated, 300 mesh).

3.2 Fourier Transform Infrared Spectroscopy

An attenuated total reflectance (ATR)-equipped VERTEX 70v Fourier transform infrared (FTIR) spectrometer (Bruker) was employed to identify the functional groups of the GNPs. The spectra of the samples were acquired in the range of 4000–400 cm^{-1} and with a resolution of 4 cm^{-1}.

3.3. X-ray Diffraction

A Miniflex X-ray diffractometer (Rigaku) equipped with Kβ-filtered Cu-Kα radiation (λ = 0.1544 nm) generated at 15 mA and 40 kV was used for X-ray diffraction (XRD) analysis. The diffractogram was recorded in the 2θ range between 10° and 90° with a scanning speed of 6° min^{-1}.

3.4. CO_2 Absorption

Fig. 1 shows the setup used for the CO_2 absorption experiments, which is identical to the one used by (Abdul Samat, Yusoff, Aroua, Ramalingam, & Kassim, 2019). CO_2 flowed from (I) to (II), where it was heated and pressurized to the required conditions. Then, 20 mL of the sample was added into (IV) and heated to the required temperature. The temperature of (II) and (IV) was kept constant during the experiment. The pressure of CO_2 was simultaneously recorded by (VII) during the experiment until

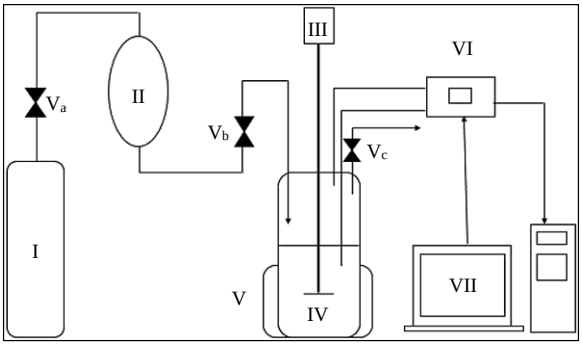

Figure 1. A diagram of the experimental setup: (I) gas cylinder, (II) gas reservoir, (III) motor, (IV) high-pressure reactor cell, (V) water bath, (VI) controller, (VII) computer, (V_a) control valve, (V_b) needle valve, and (V_c) pressure relief valve.

the equilibrium was reached, where the pressure remained constant for at least 30 min. The CO_2 absorptivity of the prepared nanofluids was determined using the CO_2 pressure drop (Eqn. (3)), expressed as CO_2 solubility (mol of CO_2 /mol of solvent).

$$PV = nRT \quad (2)$$

Table 1 Experimental conditions of CO_2 absorption

Parameters	Value
Mass concentration of MEA solution	30%
Pressure of CO_2	50, 125, and 200 psi
Temperature of thermostatic water bath	26 °C
Ultrasonication time	1 h
Volume of nanofluids	20 mL
Volume fraction of GNPs	0.01, 0.03, and 0.05

$$\Delta n = \frac{P_1 V_1}{RT} - \frac{P_2 V_2}{RT} \quad (3)$$

Where P1 and P2 are the initial and final pressures (Pa), respectively, V1 is the volume of the gas reservoir (m^3), V2 is the volume of the system except the reactor cell (m^3), R is the gas constant ($m^3 \cdot Pa \cdot K^{-1} \cdot mol^{-1}$), and T is the temperature (K). The experimental conditions of CO2 absorption are summarized in Table 1.

4. Results and Discussion

4.1. Characterization

4.1.1. HRTEM Analysis

Fig. 2 shows the optical microscopy images of GNPs. The flat multi-layered graphene sheets are rough and jagged (Fig. 2(a)). Also, the edges of the sheets appear smooth but irregular in some areas (Fig. 2(a)). The interlayer distance of the graphene sheets

DOI: https://doi.org/10.22452/mjs.vol43sp1.3
Malaysian Journal of Science 43 (Special Issue 1): 15-19 (July 2024)

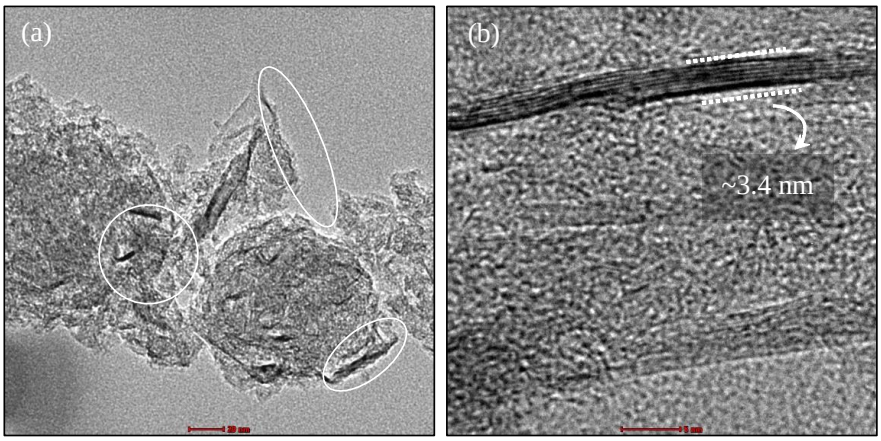

Figure 2. TEM images of GNPs

was found to be approximately 340 pm (Fig. 2(b)), in agreement with the XRD results (Fig. (3)).

4.1.2. XRD Analysis

Fig. 3 shows the XRD patterns of GNPs. It can be seen that a strong peak was emitted at 2θ = ~26.3°, which is related to the [002] plane (Gomari, Esfandeh, & Ghasemi, 2017). The wide peak at 2θ = ~43.0° and the small peak at 2θ = ~54.2° of the XRD patterns could be ascribed to the [100] and [004] peaks, respectively (Kumar et al., 2018). The interlayer distance $d_{(002)}$ is 0.34 nm, as calculated by Bragg's law (Eqn. (4)). The value is in agreement with the $d_{(002)}$ value of graphite (Farinre et al., 2022).

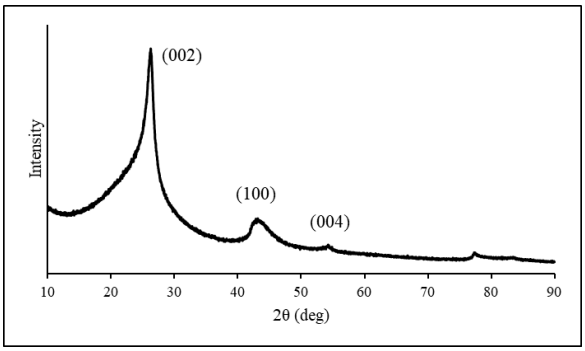

Figure 3. XRD crystallographic patterns of GNPs.

$$d_{hkl} = \frac{\lambda}{2sin\theta} \quad (4)$$

4.1.3. FTIR Analysis

Fig. 4 illustrates the bonds and their respective wavelengths of GNPs. The C=C peak was observed at 1564 cm^{-1}. As seen in the spectra, a negligible amount of oxygen groups can be found in the GNPs.

4.1.4 Stability Analysis

Nanofluid stability is important for CO_2 absorption as it influences the mass transfer enhancement mechanisms. The MEA-GNP nanofluids used in this work were prepared via the two-step method, where the production and dispersion of the nanoparticles occur in two separate steps. To achieve a uniform colloidal dispersion, ultrasonication was also employed to prepare the nanofluids. Fig. 5 visualizes the stability performance of the prepared MEA-GNP nanofluids, where the GNPs were found to be sedimented 72 h after the preparation (Fig. 5(b)).

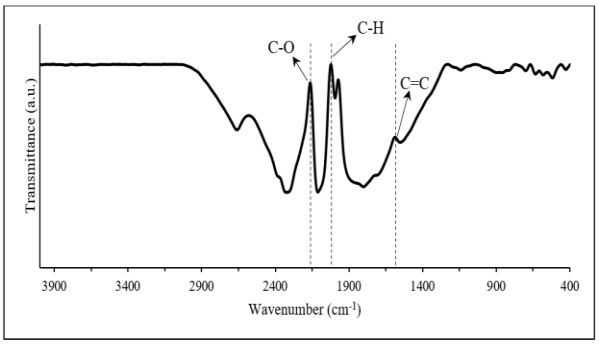

Figure 4. FTIR spectra of GNPs.

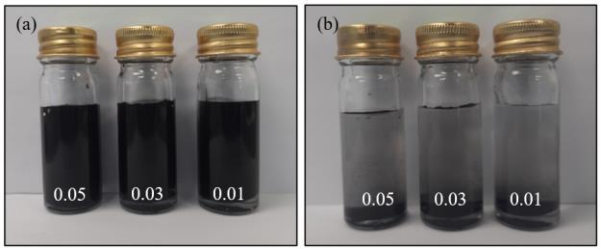

Figure 5. The stability of MEA-GNP nanofluids (a) after preparation and (b) after 72 h.

4.2. CO_2 Absorption Study

The absorption of CO_2 in the pure MEA solution is about 0.62 mol/mol MEA, which agrees with the solubility of CO_2 in MEA (0.64 mol/mol MEA) as reported by Jiang et al. (Jiang, Zhao, Zhuo, & Wang, 2014). Fig. 6 indicates that the CO_2 solubility of GNP-MEA nanofluids was slightly higher than the base fluid, MEA. The GNP addition improved the CO_2 solubility of MEA by 2%. The effect of GNP loading on the CO_2 solubility of MEA was then investigated. The CO_2 solubility of GNP-MEA nanofluids increased until reaching

DOI: https://doi.org/10.22452/mjs.vol43sp1.3
Malaysian Journal of Science 43 (Special Issue 1): 15-19 (July 2024)

the optimum level of ϕ = 0.03 and then decreased. The increase in CO_2 solubility of MEA can be explained by the generally acknowledged mass transfer enhancement mechanisms, the hydrodynamic effect, the shuttle effect, and the inhibition of bubble coalescence (Zhang et al., 2022). The shuttle effect can be explained as the nanoparticles acting as a shuttle for the adsorbed gas, transferring the gas repetitively, thus enhancing the gas-liquid mass transfer. The hydrodynamic effect relates to the

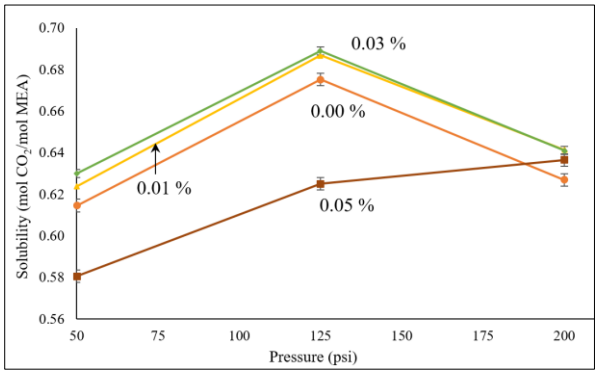

Figure 6. CO_2 solubility of nanofluids.

diffusion boundary layer of a gas-liquid system. The presence of nanoparticles induces Brownian motion, microconvections, and velocity disturbances, which affect the diffusion boundary layer and reduce its thickness. The bubbles of the gas molecules collide with nanoparticles and break into smaller bubbles. Smaller bubbles increase the gas-liquid contact area, thereby enhancing the mass transfer. This phenomenon is called the inhibition of bubble coalescence. Adding GNPs enhances the mass transfer of MEA through the mass transfer enhancement mechanisms. The effect becomes greater as the concentration of solid increases. However, when the solid loading is too high, the gas-liquid interfacial area is limited, and adjacent particles may be exposed to form a "plate", which can hinder mass transfer (Jiang et al., 2014). Combining these two effects leads to an increment, followed by a reduction in the enhancement factor with the concentration of the GNP nanoparticles. The highest enhancement result of CO_2 solubility at each concentration of GNPs can be observed at 125 psi (862 kPa).

5. Conclusion

In this study, GNP-MEA nanofluids were prepared, and its performance in CO_2 absorption was studied. The characterization revealed typical characteristics of GNPs. The experimental data revealed that the addition of GNPs increased the performance of MEA for CO_2 absorption by 2%. For the effect of nanoparticle concentrations, the CO_2 absorptivity of MEA increased with increasing concentrations until the optimum concentration was reached. The enhancement of MEA performance in CO_2 absorption was related to the generally acknowledged mass transfer enhancement mechanisms. Therefore, the suspensions of GNPs in MEA are expected to enhance CO_2 absorption.

6. Acknowledgements

Dr. A. Arifutzzaman and Professor Mohamed Kheireddine Aroua would like to acknowledge the financial support provided by Sunway University, Malaysia, through the internal grant project No. # GRTIN-IGS-CCDCU[S]-09-2022.

7. References

Abdul Samat, N. F. N., Yusoff, R. B., Aroua, M. K., Ramalingam, A., & Kassim, M. A. (2019). Solubility of CO2 in aqueous 2-amino-1, 3-propanediol (Serinol) at elevated pressures. *Journal of Molecular Liquids, 277*, 207-216. doi: https://doi.org/10.1016/j.molliq.2018.12.102

Farinre, O. Z., Alghamdi, H., Kelley, M. L., Biacchi, A. J., Albert, V., Davydov, . . . Misra, P. (2022). *A Comprehensive Study on the Molecular Dynamics of Pristine and Functionalized Graphene Nanoplatelets*.

Gomari, S., Esfandeh, M., & Ghasemi, I. (2017). All-solid-state flexible nanocomposite polymer electrolytes based on poly(ethylene oxide): Lithium perchlorate using functionalized graphene. *Solid State Ionics, 303*, 37-46. doi: https://doi.org/10.1016/j.ssi.2017.02.005

Hamidi, R., Farsi, M., & Eslamloueyan, R. (2018). CO2 solubility in aqueous mixture of MEA, MDEA and DAMP: Absorption capacity, rate and regeneration. *Journal of Molecular Liquids, 265*, 711-716. doi: https://doi.org/10.1016/j.molliq.2018.07.013

Jiang, J., Zhao, B., Zhuo, Y., & Wang, S. (2014). Experimental study of CO2 absorption in aqueous MEA and MDEA solutions enhanced by nanoparticles. *International Journal of greenhouse gas control, 29*, 135-141.

Kumar, J. S., Murmu, N. C., Samanta, P., Banerjee, A., Ganesh, R. S., Inokawa, H., & Kuila, T. (2018). Novel synthesis of a Cu2O–graphene nanoplatelet composite through a two-step electrodeposition method for selective detection of hydrogen peroxide. *New Journal of Chemistry, 42*(5), 3574-3581. doi: 10.1039/C7NJ04510G

Lai, Q., Toan, S., Assiri, M. A., Cheng, H., Russell, A. G., Adidharma, H., . . . Fan, M. (2018). Catalyst-TiO(OH)2 could drastically reduce the energy consumption of CO2 capture. *Nature Communications, 9*(1), 2672. doi: 10.1038/s41467-018-05145-0

Mohammadpoor, A., Mirzaei, M., Azimi, A., & ghomshe, m. t. (2018). The simultaneous effect of graphene oxide and sodium dodecyl sulphate nanoparticles on the kinetics of CO2 absorption in amine. *Advances in environmental science and technology, 4*, 163-174.

Mohammadpour, A., Mirzaei, M., & Azimi, A. (2019). Dimensionless numbers for solubility and mass transfer rate of CO2 absorption in MEA in presence of additives. *Chemical Engineering Research and Design, 151*, 207-213. doi: https://doi.org/10.1016/j.cherd.2019.06.026

DOI: https://doi.org/10.22452/mjs.vol43sp1.3
Malaysian Journal of Science 43 (Special Issue 1): 15-19 (July 2024)

Ochedi, F. O., Yu, J., Yu, H., Liu, Y., & Hussain, A. (2021). Carbon dioxide capture using liquid absorption methods: a review. *Environmental Chemistry Letters, 19*, 77-109.

Rahimi, K., Riahi, S., & Abbasi, M. (2020). Effect of host fluid and hydrophilicity of multi-walled carbon nanotubes on stability and CO2 absorption of amine-based and water-based nanofluids. *Journal of Environmental Chemical Engineering, 8*(1), 103580. doi: https://doi.org/10.1016/j.jece.2019.103580

Ramezani, R., Mazinani, S., & Di Felice, R. (2021). Density, Viscosity, pH, Heat of Absorption, and CO2 Loading Capacity of Methyldiethanolamine and Potassium Lysinate Blend Solutions. *Journal of Chemical & Engineering Data, 66*(4), 1611-1629.

Seo, S., Lages, B., & Kim, M. (2020). Catalytic CO2 absorption in an amine solvent using nickel nanoparticles for post-combustion carbon capture. *Journal of CO2 Utilization, 36*, 244-252.

Zhang, H., Wang, B., Xiong, M., Gao, C., Ren, H., & Ma, L. (2022). Process intensification in gas-liquid mass transfer by nanofluids: Mechanism and current status. *Journal of Molecular Liquids, 346*, 118268.

DOI: https://doi.org/10.22452/mjs.vol43sp1.3
Malaysian Journal of Science 43 (Special Issue 1): 15-19 (July 2024)

MALAYSIAN JOURNAL OF SCIENCE
MJS
ISSN 1394 - 3065

2nd Euro-Asia Conference on CO_2 Capture and Utilization (EACCO2CU2022) Special issue

Malaysian Journal of Science 43 (Special Issue 1): 20-25 (July 2024) https://mjs.um.edu.my

CHARACTERISATION OF EGG WHITE-IMPREGNATED ACTIVATED CARBON FOR CO_2 ADSORPTION APPLICATION

Nur Syahirah Mohamed Hatta[1a], Farihahusnah Hussin[2a,b], Lai Ti Gew[3b,c] and Mohamed Kheireddine Aroua[4a,b,d*]

Abstract: In this study egg white was used as a source of natural amino acids to modify the surface properties of palm shell-based activated carbon to enhance its CO_2 capture performance. A simple impregnation method was employed for this purpose. Characterisation analysis was performed on the egg white-impregnated activated carbon to examine any changes in its surface properties before the CO_2 adsorption test. The modified adsorbent showed high thermal stability below 300 °C and comprised of a new amide functional group. Furthermore, the modified adsorbent exhibited a 31% higher breakthrough time and maintained its CO_2 adsorption capacity at 0.3 mmol/g, in comparison to raw activated carbon, regardless of the surface area and micropore volume reductions of 17% and 18%, respectively. These findings provide evidence for the prospect of using egg white-impregnated activated carbon for CO_2 adsorption applications, which could lead to a new generation of affordable and eco-friendly adsorbents.

Keywords: Activated carbon, CO_2 capture, CO_2 adsorption, Natural Amino Acids, Egg White

1. Introduction

Carbon dioxide (CO_2) emissions account for about 76% of all global greenhouse gas emissions, leading to climate warming (U.S. EPA, 2023). In fact, the sudden drop in daily carbon dioxide (CO_2) emissions during the pandemic in 2019 due to measures like stringent movement control orders demonstrated that human activities are contributing to the rise of global CO_2 concentration (Le Quéré et al., 2020; Rasmussen, 2021). Although major efforts have been made worldwide to reduce CO_2 emissions, in the long run, more sustainable ways are still required from the social, environmental and economic perspectives. One key solution to this issue is to implement Carbon Capture and Sequestration (CCS) technology, preferably by post-combustion mode which can be easily integrated into existing plants (Allangawi et al., 2023). Of the post-combustion methods available, adsorption constitutes to a highly profitable and effective means of CO_2 capture, consuming less energy than the conventional absorption process (Khan et al., 2023).

Authors information:
[a]Research Centre for Carbon Dioxide Capture and Utilisation (CCDCU), School of Engineering and Technology, Sunway University, Bandar Sunway, Petaling Jaya 47500, Selangor, MALAYSIA. E-mail: nur.m227@imail.sunway.edu.my[1]
[b]Sunway Materials Smart Science and Engineering (SMS2E) Research Cluster, Sunway University, Bandar Sunway, Petaling Jaya 47500, Selangor, MALAYSIA. E-mail: farihah@sunway.edu.my[2]
[c]Department of Biological Sciences, School of Medical and Life Sciences, Sunway University, Bandar Sunway, Petaling Jaya 47500, Selangor, MALAYSIA. E-mail: janeg@sunway.edu.my[3]
[d]School of Engineering, Lancaster University, Lancaster LA1 4YW, UK. E-mail: kheireddinea@sunway.edu.my[4]

*Corresponding Author: kheireddinea@sunway.edu.my

Typical groups of adsorbents include activated carbons, polymeric materials, zeolites, silica and metal–organic frameworks (MOFs). However, the efficiency of capturing CO_2 using solid sorbents (adsorbents) always depend on the selection of a suitable adsorbent for use in a particular application (Ketabchi et al., 2023). Subsequently, these adsorbents are generally subjected to physicochemical treatment to enhance their surface functionalities and thus increase their CO_2 selectivity. Malaysia has abundant biomass/biowaste resources that could be converted into activated carbon. These biomass-derived forms of carbon are inexpensive and can be further modified for improved surface functionalities (Nazir et al., 2023). However, the solvents commonly used as modifying agents during the treatment are alkaline metal salts, strong acids and amine-based solvents, which have proven less environmentally friendly (Shu Hui & Ahmad Zaini, 2015; You & Kim, 2020). Therefore, a sustainable approach would be to use green solvents like natural-based ionic liquids (ILs) and deep eutectic solvents (DESs) (Vanda et al., 2018; Zhao et al., 2021). These solvents not only possess low toxicity and high biodegradability but also potentially reduce material costs owing to the cheap, abundant and easily accessible natural compounds, i.e., organic acids and bases, amino acids, sugars and choline (Vanda et al., 2018). Of these, amino acid was found to be prominently functionalised with IL (AAIL) and DES (Suhaili et al., 2023), and it was used as a modifying agent with porous solids, suggesting its efficiency in facilitating the CO_2 capture process (Balsamo et al., 2018; Philip & Henni, 2023).

Pure single amino acids can be easily obtained commercially but they cost more than other natural compounds. Alternatively, amino acids can be sourced from foods and plants. For example, Imtiaz-Ul-Islam et al. (2011) determined that whey protein could

Received: February 7, 2024
Accepted: May 7, 2024
Published: July 31, 2024

DOI: https://doi.org/10.22452/mjs.vol43sp1.4
Malaysian Journal of Science 43 (Special Issue 1): 20-25 (July 2024)

adsorb CO_2 over 15 cycles with a minimal loss of capacity, a better result compared to activated carbon and zeolites. Other recent literature has explored the use of egg white in fabricating nitrogen-doped materials but in other applications such as wastewater treatment (Chen et al., 2022; Wang et al., 2020) and high-performance supercapacitor electrodes (Zhu et al., 2019). Furthermore, Gil-Lalaguna et al. (2022) reported that protein-containing livestock wastes can also be converted into pyrolysis char and used as a CO_2 adsorbent, although they exhibited a lower adsorption capacity than pure proteins. Albumen (egg whites) is closer to a pure amino acids chain than other sources of natural amino acids and could offer immense potential as a surface modifying agent. Some bakery and cosmeceutical industries discard large amounts of egg white, normally during pastry making and antibody cultivation (Lu et al., 2022). From this perspective, repurposing egg white waste might not only promote the circular economy but also help in addressing two environmental issues at once (waste management and climate warming).

This paper presents a preliminary investigation into the CO_2 adsorption performance and characteristics of palm shell-based activated carbon after impregnation with 50 wt.% of egg white solution. In comparison to raw activated carbon, the egg white-impregnated activated carbon was characterised using a field emission scanning electron microscope with energy-dispersive x-ray (FESEM-EDX), while a surface area and pore volume analyser was used to examine the changes in surface physical properties and elemental compositions. To determine the chemical properties, Fourier transform infrared (FTIR) spectroscopy was performed to analyse the functional groups of the adsorbent. The thermal stability of the adsorbent was also inspected using a simultaneous thermal analyser (STA) before the CO_2 adsorption test using a packed-bed column. Two fundamental parameters pertaining to CO_2 adsorption performance are the breakthrough time and CO_2 adsorption capacity, which were also measured.

2. Experiment

2.1 Materials

Fresh chicken eggs were purchased from a local supermarket, while palm kernel shell-based activated carbon (C2889, Sigma-Aldrich) was purchased from the supplier. The purified carbon dioxide (99.8%) and nitrogen (99.995%) gases were supplied by Alpha Gas Solution Sdn. Bhd., Malaysia.

Preparation of egg white impregnated activated carbon

The activated carbon (AC) was initially washed and oven-dried overnight at 100-120 °C to remove impurities and fine particles. The dried AC was then kept in a desiccator until needed. An egg white (EW) concentration of 50 wt.% was selected as an initial study. To prepare the solution, EW was separated from the yolk before being diluted with deionised (DI) water to produce a solution with a 1:1 ratio in terms of weight. The solution was then added to the dried AC and left for 24 hours at room temperature (25 °C) before being oven-dried at 50 °C to allow the EW solution to disperse into the pore surfaces of the AC (Mohamed Hatta et al., 2023).

2.2 Characterisation

The impregnated AC was characterised using a field emission scanning electron microscope with energy-dispersive x-ray spectroscopy (FESEM-EDX) (Tescan Analytics, TESCAN VEGA3, Czech Republic) for the surface morphology and elemental composition analyses. Fourier transform infrared (FTIR) spectroscopy (Bruker, VERTEX 70v, USA) was used to analyse the changes in chemical bonds and functional groups present after the modification process. A Micromeritics accelerated surface area and porosity (ASAP) 2020 instrument was used to determine the surface area and pore volume. To ascertain the thermal decomposition of the sample, a simultaneous thermal analysis (STA) was performed under 20 mL/min of nitrogen (N_2) flow at a heating rate of 10 °C/min.

2.3 CO_2 adsorption test

The CO_2 adsorption performance of the EW-impregnated AC was evaluated using a system with a single packed-bed column under atmospheric pressure (1 atm). The test was conducted at a temperature of 25 °C and a flow rate of 200 mL/min (15 vol.% CO_2/N_2). The adsorption column filled with the sample was purged with the N_2 flow to remove other gases from the column and those that were readily adsorbed on the sample. The adsorption was started, and the concentration of CO_2 leaving the adsorption column was recorded using a digital logger at one-minute intervals. The CO_2 concentration profile was presented in the form of C_t/C_0 against time. The breakthrough time is defined as the time when CO_2 reaches the end of the column and leaves with the other gas effluent (Gabelman, 2017), commonly determined at a 5% concentration (C_t/C_o = 0.05). The CO_2 adsorption capacity was then calculated.

3. Results and discussion

3.1 FESEM-EDX analysis

Figure 1 shows the results obtained from the FESEM-EDX analysis of the AC before and after the impregnation with 50 wt.% EW solution. Figure 1 (a and c) indicates that the surface and pores of the impregnated AC were partially covered by a thick layer, of what were assumed to be EW particles. This accumulation of EW particles on the AC surface and pores could be due to the use of a relatively high concentration of EW solution and the poor dispersion of the solution during impregnation. As a result, partially complete pore blocking was observed, as indicated by the apparent size of the surface pore openings reducing from a range of 4–10 µm to a range of 4–6 µm.

Conversely, the result of the EDX analysis shown in Figure 1 (b and d) reveals that the relative percentage composition of the oxygen (O) element in the EW-impregnated AC increased from 7.4 wt.% to 13.5 wt.%, and a new element was present (2.1 wt.% nitrogen (N)). This suggests that the EW was successfully impregnated onto the AC. Furthermore, the N element was prominently observed, which could aid the CO_2 adsorption, although this depends on the type of N-functionalities (Saha &

DOI: https://doi.org/10.22452/mjs.vol43sp1.4
Malaysian Journal of Science 43 (Special Issue 1): 20-25 (July 2024)

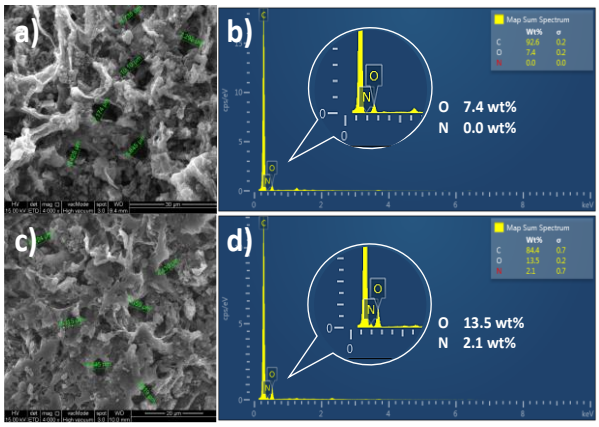

Figure 1. Results of FESEM-EDX analysis of palm shell-based activated carbon before (a and b) and after impregnation with 50 wt.% egg white solution (c and d).

Kienbaum, 2019). Further analysis is needed to validate this assumption.

3.2 Surface area and pore volume

The BET surface area analysis result revealed that the AC impregnated with 50 wt.% EW decreased in total surface area from 679 to 565 m^2/g. The t-plot micropore area also showed a reduction from 441 to 363 m^2/g. Meanwhile, the t-plot micropore volume decreased from 0.1798 to 0.1481 cm^3/g after the impregnation. However, all the reductions were below 18%, despite the higher concentration of EW used leading to the deposition of a thick layer of EW on the AC surfaces, thus blocking some of the micropores. These results agreed with the FESEM-EDX analysis.

3.3 FTIR analysis

Figure 2 displays the infrared spectra of palm shell AC before (top) and after (bottom) impregnation with 50 wt.% EW. All the absorption bands between 2662 cm^{-1} and 1589 cm^{-1} generated by both samples generally represent the peaks for the C-H stretching and aromatic ring vibration stretching (C≡C, C=C, C–O and C=O) of the AC (Rugayah, 2014). Meanwhile, the peaks between 3740 cm^{-1} and 3660 cm^{-1} may be attributed to the O-H stretching in hydroxyl groups or adsorbed water in the AC (Rugayah, 2014), which could be due to incomplete moisture removal during the analysis. Remarkably, the EW-impregnated AC revealed the presence of new peaks at 3557 cm^{-1}, 2957 cm^{-1}, and within a range of 1642 to 1514 cm^{-1}, confirming the existence of amide compounds in this EW-impregnated AC. The first two peaks from 1650 cm^{-1} to 1620 cm^{-1} were probably linked to C=O absorption of amide I and NH_2 deformation of amide II in primary amide, respectively (Parker, 1971). The peak near 1514 cm^{-1} could relate to the secondary noncyclic amide (amide II), while the peak at 3557 cm^{-1} indicates the stretching of free N-H of primary amide (Parker, 1971). Although the peak at 2957 cm^{-1} commonly represents the C-H stretching, it could also be interpreted as the band in free amines (Sashina et al., 2015). These findings confirmed that the EW was impregnated onto the AC. However, it is unclear whether this functional group was attached to the AC surface physically or chemically, unlike with the grafting method which is known to form covalent bonding with the grafted compound, but this would require a more advanced characterisation method.

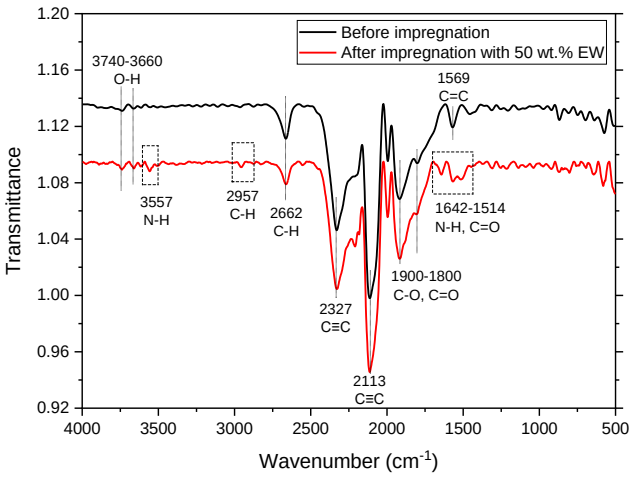

Figure 3. FTIR spectra of palm shell-based activated carbon before and after impregnation with 50 wt.% egg white solution.

3.4 Thermal analysis

Generally, the thermal properties of an adsorbent depend strongly on the stability of the material under heat treatment, and any modification to the material could alter its original properties. Therefore, thermal decomposition analysis can provide insightful information on the type of suitable application for which the material can be applied at its maximum allowable temperature. Figure 3 shows the thermal decomposition analysis of the 50 wt.% EW-impregnated AC. The initial weight loss of approximately 5% below 100 °C was due to the moisture loss of the sample. Depending on the type of feedstock, AC derived from biomass typically has high thermal stability above 500 °C (Sharma et al., 2021). In this study, the EW-impregnated AC lost 50% of its weight at 302 °C, as indicated by the onset degradation of the thermogravimetric curve (black) coinciding with a medium peak of the heat flow curve (blue) and the maximum endothermic peak

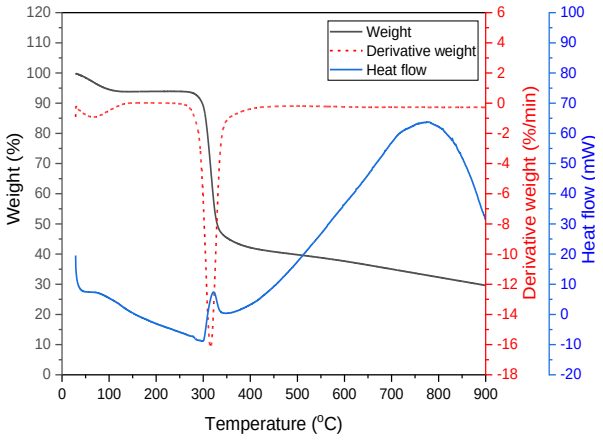

Figure 2. Thermal analysis of palm shell-based activated carbon after impregnation with 50 wt.% egg white solution.

DOI: https://doi.org/10.22452/mjs.vol43sp1.4
Malaysian Journal of Science 43 (Special Issue 1): 20-25 (July 2024)

of the derivative weight curve (red). This could be attributed to the amino acids of the EW decomposing, which was reported between temperatures of 178 and 344 °C (Sashina et al., 2015). Similar results were observed in previous studies related to amino acid-incorporated adsorbents (Philip & Henni, 2023; Suhaili et al., 2023). At temperatures over 350 °C, the sample continued to degrade slowly, and about 28% of the weight remained at the end of the analysis (900 °C).

3.5 CO_2 adsorption performance

Figure 4 displays the CO_2 breakthrough curve for the AC before and after impregnation with 50 wt.% of EW. The results illustrate that the breakthrough time for the EW-impregnated AC was slightly longer (8.4 min) than its original performance (6.4 min). Furthermore, the steeper curve slope suggested an efficient mass transfer rate of the adsorbate throughout the packed-bed column (Gabelman, 2017). Meanwhile, the CO_2 adsorption capacity of the AC remained similar, with a minimal drop from 0.3204 mmol/g to 0.3029 mmol/g, most likely attributed to the significant reductions in the surface area and micropore volume after impregnation. Theoretically, physical impregnation means simply mixing the support and solution, whereby the solution monomer/polymer diffuses into the pores of the support materials without significant pore blockages (Jahandar Lashaki et al., 2019). Therefore, the surface area and pore volume reductions were normal, as reported in an amine-impregnated adsorbent (Gholidoust et al., 2017). However, these reductions may have compensated for the improved adsorption performance because the pores filled with additional functional groups that could adsorb more CO_2. In contrast, a very high solution concentration could lead to aggregation of the dried solution particles. In this case, EW attached onto the AC surface and blocked the pores, thus reducing the CO_2 accessibility to the amino acid functionalities inside the pores (Jahandar Lashaki et al., 2019). This could further explain the improved of breakthrough time of the EW-impregnated AC and the insignificant decline in its adsorption capacity. The EW-impregnated AC exhibited the longest breakthrough time compared with other waste-derived ACs, although further investigations are required to improve its adsorption capacity (Table 1).

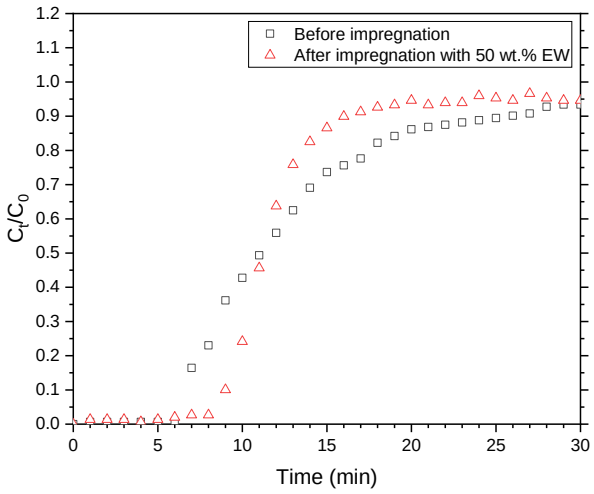

Figure 4. Breakthrough curve of CO_2 adsorption by palm shell-based activated carbon before and after impregnation with 50 wt.% egg white solution.

4. Conclusion

This study investigated CO_2 adsorption performance in correlation with the characteristics of palm shell-derived AC after impregnation with 50 wt.% of EW solution. The overall findings were promising, suggesting that EW could be an alternative green modifying agent to enhance the surface properties of AC. The successful impregnation of EW was clearly observed from the FTIR analysis results, with the presence of new peaks assigned to amide bands supported further by a 31% improvement in adsorption performance in terms of breakthrough time compared

Table 1. Comparison of CO_2 adsorption performance with other biomass/waste-derived activated carbons.

Adsorbent	Operating condition	Activation agent	Breakthrough time (min)	CO_2 adsorption capacity (mmol/g)	Reference
Palm kernel shell activated carbon	25°C, 1 bar	-	6.4	0.32	This study
	15% CO_2	50 wt.% egg white	8.4	0.30	
Palm kernel shell activated carbon	4 bar	-	< 0.1	0.54	Abdul Rani and Muda (2017)
	10% CO_2	10 wt.% CeO_2	5.8	0.63	
PET waste derived activated carbon	30°C, 1 bar	-	< 0.1	~0.55 (12.5% CO_2)	Kaur et al. (2019)
	5% CO_2	KOH to carbon (3:1)	3.2	0.55 1.33 (12.5% CO_2)	
Plastic derived activated carbon	15°C, 1 bar	-	< 0.1	0.14	Ligero et al. (2023)
	10% CO_2	KOH to carbon (2:1)	0.6	0.62 0.38 (30°C)	

DOI: https://doi.org/10.22452/mjs.vol43sp1.4
Malaysian Journal of Science 43 (Special Issue 1): 20-25 (July 2024)

to raw AC. Thermal analysis also revealed that almost half the impregnated AC was decomposed at temperatures above 300 °C, which was related to the decomposition temperature of amino acid compounds. In terms of CO_2 adsorption capacity, the EW-impregnated AC performance was similar to that of raw AC, as inferred from the surface area and pore volume results, as well as the FESEM-EDX analyses. The surface area and pore volume reductions confirmed that the EW solution was filling the pores and deposited on the surface of AC surface; however, this was also found to cause a pore blockage phenomenon. While newly added amide functional groups of EW were successfully impregnated, as indicated by the FTIR analysis, some might have been completely blocked inside the AC pores. This left the remainder attached onto the outer surface layer of the AC and led to constant instead of improved adsorption capacity. Regardless, the EW-impregnated AC could still retain the CO_2 adsorbed on its surfaces for longer than the raw AC and other waste-derived activated carbons from the literature, indicating its potential as a new eco-friendly adsorbent. Future research could examine how to refine the method to optimise the adsorption capacity and the possible interaction mechanisms between this adsorbent and CO_2.

5. Acknowledgement

This research was funded by the Ministry of Higher Education, Malaysia, under Fundamental Research Grant Scheme (FRGS/1/2020/TK0/SYUC/01/2). The first author (Mohamed Hatta, N.S.) would like to thank Sunway University for providing the PhD scholarship for her postgraduate study.

6. References

Abdul Rani, N. H., & Muda, N. (2017). Impregnated Palm Kernel Shell Activated Carbon for CO_2 Adsorption by Pressure Swing Adsorption. *Indian Journal of Science and Technology,* 10. https://doi.org/10.17485/ijst/2017/v10i2/110377

Allangawi, A., Alzaimoor, E. F. H., Shanaah, H. H., Mohammed, H. A., Saqer, H., El-Fattah, A. A., & Kamel, A. H. (2023). Carbon Capture Materials in Post-Combustion: Adsorption and Absorption-Based Processes. *C, 9*(1), 17. https://doi.org/10.3390/c9010017

Balsamo, M., Erto, A., Lancia, A., Totarella, G., Montagnaro, F., & Turco, R. (2018). Post-combustion CO_2 capture: On the potentiality of amino acid ionic liquid as modifying agent of mesoporous solids. *Fuel, 218,* 155-161. https://doi.org/10.1016/j.fuel.2018.01.038

Chen, Y.-S., Ooi, C. W., Show, P. L., Hoe, B. C., Chai, W. S., Chiu, C.-Y., . . . Chang, Y.-K. (2022). Removal of Ionic Dyes by Nanofiber Membrane Functionalized with Chitosan and Egg White Proteins: Membrane Preparation and Adsorption Efficiency. *Membranes, 12*(1), 63. https://doi.org/10.3390/membranes12010063

U.S. EPA. (2023). Global Greenhouse Gas Emissions Data https://www.epa.gov/ghgemissions/global-greenhouse-gas-emissions-data (accessed August 28, 2023).

Gabelman, A. (2017). Adsorption Basics: Part 1. Chemical Engineering Progress. https://www.aiche.org/resources/publications/cep/2017/july/adsorption-basics-part-1 (accessed July 4, 2023)

Gholidoust, A., Atkinson, J. D., & Hashisho, Z. (2017). Enhancing CO_2 Adsorption via Amine-Impregnated Activated Carbon from Oil Sands Coke. *Energy & Fuels*, *31*(2), 1756-1763. https://doi.org/10.1021/acs.energyfuels.6b02800

Gil-Lalaguna, N., Navarro-Gil, Á., Carstensen, H.-H., Ruiz, J., Fonts, I., Ceamanos, J., . . . Gea, G. (2022). CO_2 adsorption on pyrolysis char from protein-containing livestock waste: How do proteins affect? *Science of The Total Environment*, *846*, 157395. https://doi.org/10.1016/j.scitotenv.2022.157395

Imtiaz-Ul-Islam, M., Hong, L., & Langrish, T. (2011). CO_2 capture using whey protein isolate. *Chemical Engineering Journal*, *171*(3), 1069-1081. https://doi.org/10.1016/j.cej.2011.05.003

Jahandar Lashaki, M., Khiavi, S., & Sayari, A. (2019). Stability of amine-functionalized CO_2 adsorbents: a multifaceted puzzle. *Chemical Society Reviews*, *48*(12), 3320-3405. https://doi.org/10.1039/C8CS00877A

Kaur, B., Gupta, R. K., & Bhunia, H. (2019). Chemically activated nanoporous carbon adsorbents from waste plastic for CO_2 capture: Breakthrough adsorption study. *Microporous and Mesoporous Materials*, *282*, 146-158. https://doi.org/10.1016/j.micromeso.2019.03.025

Ketabchi, M. R., Babamohammadi, S., Davies, W. G., Gorbounov, M., & Masoudi Soltani, S. (2023). Latest advances and challenges in carbon capture using bio-based sorbents: A state-of-the-art review. *Carbon Capture Science & Technology*, *6*, 100087. https://doi.org/10.1016/j.ccst.2022.100087

Khan, U., Ogbaga, C. C., Abiodun, O.-A. O., Adeleke, A. A., Ikubanni, P. P., Okoye, P. U., & Okolie, J. A. (2023). Assessing absorption-based CO_2 capture: Research progress and techno-economic assessment overview. *Carbon Capture Science & Technology*, *8*, 100125. https://doi.org/10.1016/j.ccst.2023.100125

Le Quéré, C., Jackson, R. B., Jones, M. W., Smith, A. J. P., Abernethy, S., Andrew, R. M., . . . Peters, G. P. (2020). Temporary reduction in daily global CO_2 emissions during the COVID-19 forced confinement. *Nature Climate Change*, *10*(7), 647-653. https://doi.org/10.1038/s41558-020-0797-x

Ligero, A., Calero, M., Martín-Lara, M. Á., Blázquez, G., Solís, R. R., & Pérez, A. (2023). Fixed-bed CO_2 adsorption onto activated char from the pyrolysis of a non-recyclable plastic mixture from real urban residues. *Journal of CO_2 Utilization*, *73*, 102517. https://doi.org/10.1016/j.jcou.2023.102517

Lu, Y.-R., Chen, H.-C., Liu, K., Liu, M., Chan, T.-S., & Hung, S.-F. (2022). Turn the Trash into Treasure: Egg-White-Derived Single-Atom Electrocatalysts Boost Oxygen Reduction Reaction. *ACS Sustainable Chemistry & Engineering*, *10*(20),

DOI: https://doi.org/10.22452/mjs.vol43sp1.4
Malaysian Journal of Science 43 (Special Issue 1): 20-25 (July 2024)

6736-6742. https://doi.org/10.1021/acssuschemeng.2c00878

Mohamed Hatta, N. S., Hussin, F., Gew, L. T., & Aroua, M. K. (2023). Enhancing surface functionalization of activated carbon using amino acids from natural source for CO_2 capture. *Separation and Purification Technology*, *313*, 123468. https://doi.org/10.1016/j.seppur.2023.123468

Nazir, G., Rehman, A., Hussain, S., Mahmood, Q., Fteiti, M., Heo, K., . . . Aizaz Ud Din, M. (2023). Towards a sustainable conversion of biomass/biowaste to porous carbons for CO_2 adsorption: recent advances, current challenges, and future directions. *Green Chemistry*, *25*(13), 4941-4980. https://doi.org/10.1039/D3GC00636K

Parker, F. S. (1971). Amides and Amines. In F. S. Parker (Ed.), *Applications of Infrared Spectroscopy in Biochemistry, Biology, and Medicine* (pp. 165-172). Springer US. https://doi.org/10.1007/978-1-4684-1872-9_8

Philip, F. A., & Henni, A. (2023). Incorporation of Amino Acid-Functionalized Ionic Liquids into Highly Porous MOF-177 to Improve the Post-Combustion CO_2 Capture Capacity. *Molecules*, *28*(20), 7185. https://doi.org/10.3390/molecules28207185

Rasmussen, C. (2021). *Emission Reductions From Pandemic Had Unexpected Effects on Atmosphere* https://www.jpl.nasa.gov/news/emission-reductions-from-pandemic-had-unexpected-effects-on-atmosphere (accessed August 28, 2023)

Rugayah, A. F. A., A A; Norzita, N. (2014). Preparation and Characterisation of Activated Carbon from Palm Kernel Shell by Physical Activation with Steam. *Journal of Oil Palm Research*, *26*(3), 251-264.

Saha, D., & Kienbaum, M. J. (2019). Role of oxygen, nitrogen and sulfur functionalities on the surface of nanoporous carbons in CO_2 adsorption: A critical review. *Microporous and Mesoporous Materials*, *287*, 29-55. https://doi.org/10.1016/j.micromeso.2019.05.051

Sashina, E. S., Golubikhin, A. Y., & Susanin, A. I. (2015). Prospects for Producing New Biomaterials Based on Fibroin. *Fibre Chemistry*, *47*(4), 253-259. https://doi.org/10.1007/s10692-016-9675-8

Sharma, S., Kaur, M., Sharma, C., Choudhary, A., & Paul, S. (2021). Biomass-Derived Activated Carbon-Supported Copper Catalyst: An Efficient Heterogeneous Magnetic Catalyst for Base-Free Chan–Lam Coupling and Oxidations. *ACS Omega*, *6*(30), 19529-19545. https://doi.org/10.1021/acsomega.1c01830

Shu Hui, T., & Ahmad Zaini, M. A. (2015). Potassium hydroxide activation of activated carbon: A commentary. *Carbon Letters*, *16*, 275-280. https://doi.org/10.5714/CL.2015.16.4.275

Suhaili, N., Lim, L., Teh, L. P., Shahdan, S. N., & Manabu, Z. G. (2023). Effect of Arginine-Based Deep Eutectic Solvents on Supported Porous Sorbent for CO_2. *Sains Malaysiana*, *52*(5), 1419-1434. https://doi.org/10.17576/jsm-2023-5205-08

Vanda, H., Dai, Y., Wilson, E. G., Verpoorte, R., & Choi, Y. H. (2018). Green solvents from ionic liquids and deep eutectic solvents to natural deep eutectic solvents. *Comptes Rendus Chimie*, *21*(6), 628-638. https://doi.org/10.1016/j.crci.2018.04.002

Wang, Q., Lei, L., Wang, F., Chen, C., Kang, X., Wang, C., . . . Chen, Z. (2020). Preparation of egg white@zeolitic imidazolate framework-8@polyacrylic acid aerogel and its adsorption properties for organic dyes. *Journal of Solid State Chemistry*, *292*, 121656. https://doi.org/10.1016/j.jssc.2020.121656

You, C., & Kim, J. (2020). Quantitative risk assessment of an amine-based CO_2 capture process. *Korean Journal of Chemical Engineering*, *37*(10), 1649-1659. https://doi.org/10.1007/s11814-020-0567-5

Zhao, Y., Dong, Y., Guo, Y., Huo, F., Yan, F., & He, H. (2021). Recent progress of green sorbents-based technologies for low concentration CO_2 capture. *Chinese Journal of Chemical Engineering*, *31*, 113-125. https://doi.org/10.1016/j.cjche.2020.11.005

Zhu, Y., Fang, T., Hua, J., Qiu, S., Chu, H., Zou, Y., . . . Zeng, J.-L. (2019). Biomass-Derived Porous Carbon Prepared from Egg White for High-performance Supercapacitor Electrode Materials. *ChemistrySelect*, *4*(24), 7358-7365. https://doi.org/10.1002/slct.201901632

DOI: https://doi.org/10.22452/mjs.vol43sp1.4
Malaysian Journal of Science 43 (Special Issue 1): 20-25 (July 2024)

MALAYSIAN JOURNAL OF SCIENCE
MJS
ISSN 1394 - 3065

2nd Euro-Asia Conference on CO_2 Capture and Utilization (EACCO2CU2022)

Special issue

Malaysian Journal of Science 43 (Special Issue 1): 26-32 (July 2024)

https://mjs.um.edu.my

SYNTHESIS AND CHARACTERISATION OF 2-(METHYLAMINO)ETHANOL-BASED DEEP EUTECTIC SOLVENTS FOR CO_2 CAPTURE

Mohd Azlan Kassim[a1]*, Ameen Gabr Ahmed Alshaghdari[b2], Rozita Yusoff[b3] and Mohamed Kheireddine Aroua [b,c,d4]

Abstract: In recent years, deep eutectic solvents (DESs) have attracted the interest of many researchers for application in a wide range of industrial and scientific fields, including carbon dioxide (CO_2) capture. DESs exhibit favourable solvent properties for CO_2 removal applications; hence, they have become promising alternatives to common amine solutions and ionic liquids (ILs). In this context, a novel DES was synthesised by mixing 2 (methylamino)ethanol (2-MAE) as a hydrogen bond donor with choline hydroxide (ChOH) as a hydrogen bond acceptor with a molar ratio of ChOH:2-MAE of 1:1. The solubility of CO_2 in the prepared systems was determined and characterised before and after CO_2 absorption by measuring their physicochemical properties (density and viscosity) and analysing their FTIR spectra. The results showed that the DES and 2M DES aqueous solutions exhibited CO_2 absorption capacities comparable to those of other reported DESs. These physicochemical properties were comparable to those reported in the literature. Besides, the FTIR analysis of the studies systems after absorption indicates the formation of carbamate.

Keywords: Deep eutectic solvents, 2 (methylamino)ethanol, choline hydroxide, physiochemical properties, CO_2 solubility.

1. Introduction

One of the primary factors in global warming and climate change is seen to be the growing and continuous emission of the greenhouse gas carbon dioxide into the atmosphere as a result of the increased demand for fossil fuels in the industrial activity and automation era. (Dincer & Abu-Rayash, 2020). According to reports, carbon dioxide (CO_2), which accounts for 60% of all greenhouse gases released into the environment, is primarily produced by the steel, cement, petrochemical, energy, and transportation industries (IEA, 2023; Kassim, Sairi, Yusoff, Alias, & Aroua, 2016). In 2019, the combustion of fossil fuels in the United States was responsible for around 80% of all greenhouse gas emissions (Agency, 2021, April 14). According to Earth System Models (ESMs), the average results of ESMs predict that the temperature will rise by between 1.0 and 3.7 °C in the twenty-first century (Anderson, Hawkins, & Jones, 2016). These increasing signs thus necessitate action to create effective and affordable technology to reduce carbon dioxide emissions at their source.

Authors information:

[a]Green Solvent and Processes Team, Research Centre of Carbon Dioxide Capture and Utilisation (CCDCU), School of Engineering and Technology, Sunway University, Bandar Sunway, 47500 Petaling Jaya, Malaysia. Email:azlanka@sunway.edu.my[1], kheireddinea@sunway.edu.my[4]

[b]Chemical Engineering Department, Faculty of Engineering, University of Malaya, 50603 Kuala Lumpur, MALAYSIA. Email: ameenalshagdari@gmail.com[2], ryusoff@um.edu.my[3]

[c]Sunway Materials Smart Science & Engineering Research Cluster (SMS2E), Sunway University, No. 5 Jalan Universiti, Bandar Sunway, 47500 Petaling Jaya, Selangor, Malaysia. Email: kheireddinea@sunway.edu.my [4]

[d]Department of Engineering, Lancaster University, Lancaster LA1 4YW, UK. Email: kheireddinea@sunway.edu.my [4]

*Corresponding Author: azlanka@sunway.edu.my

Since the first decade of the 20th century, much research has been done to create effective methods for capturing and storing carbon dioxide. Numerous developments for CO_2 collection, including physicochemical and biological methods, have undergone extensive research (Nanda, Reddy, Mitra, & Kozinski, 2016; Zubeir, Lacroix, Meuldijk, Kroon, & Kiss, 2018). Today, the majority of CO_2 is removed or collected by physical and chemical absorption employing solvents including aqueous ammonia amines, ionic liquids, amino acid salts, and deep eutectic solvents (P.-C. Chen & Lin, 2018). Ionic liquids (ILs) and deep eutectic solvents (DESs) are two solvents that can be developed to be utilised broadly, effectively, and efficiently in large-scale applications. They are among the most promising, new, and environmentally friendly solvents (Suzuki, 2018; Zhang, De Oliveira Vigier, Royer, & Jérôme, 2012).

Since their potential was found, research on amine solvents and ionic liquids (ILs) has increased during the past 20 years. Deep eutectic solvents (DESs) were designed to address the shortcomings of traditional ionic liquids (ILs), including their high cost of synthesis, toxicity, and poor biodegradability. DESs were presented and classed as a unique type of ionic liquid (C.-C. Chen et al., 2021; Zurob et al., 2020). DESs are defined as a combination of two to three inexpensive, safe, and mostly quaternary ammonium salts or halide salts with hydrogen bond donor (HBD) components (Smith, Abbott, & Ryder, 2014). These mixes mostly consist of nonsymmetric ions, which have low melting temperatures due to their low lattice energy. As a result, the creation of DES is easier than that of ILs; in fact, nearly all DESs may be synthesised by combining a hydrogen bond acceptor (HBA) and a hydrogen bond donor (HBD) (Tomé, Baião, da Silva, & Brett, 2018; Zhang et al., 2012).

Received: February 7, 2024
Accepted: May 7, 2024
Published: July 31, 2024

DOI: https://doi.org/10.22452/mjs.vol43sp1.5
Malaysian Journal of Science 43 (Special Issue 1): 26-32 (July 2024)

Among all DES's potential uses, absorbing CO_2 appears to provide the best prospects for sustainability and effectiveness (Smith et al., 2014; Zurob et al., 2020). However, a large variety of these solvents may be generated due to the ease with which DESs can be made utilising HBD and salts as HBA. As a result, there will be much interest in the use of these solvents in CO_2 absorption in the future years.

Numerous studies have been conducted to develop efficient technology, to tackle CO_2 emissions from its sources, such as using novel green solvents such as deep eutectic solvents (DESs). Several studies have been conducted on absorbing CO_2 using an aqueous mixture of 2- (methylamino)ethanol (2-MAE), and good gas solubility was observed in certain conditions. Therefore, the great performance of 2- (methylamino)ethanol (2-MAE) shows potential to be used as a hydrogen bond donor (HBD) and different types of salts as hydrogen bond acceptor HBA. However, up to our knowledge, the scope of some of these studies was limited to certain types of hydrogen bond acceptors and certain absorbing conditions. Therefore, this work aims to synthesise and characterise 2 (methylamino)ethanol (2-MAE)-Based DES and 2M DES aqueous solution as well as to evaluate their performance on the capacity of CO_2 absorption.

2. Materials and methods

2.1 Materials and Synthesis

Materials used in this work are 2- (methylamino)ethanol (2-MAE), choline chloride (ChCl), choline hydroxide solution 46 wt. % in H_2O were purchased from Sigma-Aldrich. Carbon dioxide (CO_2) was purchased from Alpha Gas Solution. All materials were used without further purification.

2.2 Synthesis of DES

ChOH:2-MAE was synthesised according to the literature (Hussin, Aroua, & Yusoff, 2021). An equimolar mixture of 45 wt% ChOH in methanol and 2-MAE was mixed in a round bottom flask with heating and stirring at 353.15 K for 30 minutes. Then, the solvent removal takes place in a rotary evaporator for 2 hours under reduced pressure. The sample was then dried in a vacuum oven overnight with 70 mbar pressure to remove excess moisture and the acquired DES was obtained and kept in tightly sealed bottles.

2.3 Sample preparation

2M DES aqueous mixtures were prepared by weighing each compound using a calibrated single pan digital balance (HR-250AZ, A&D Japan) with an accuracy of 0.1 mg. To reduce moisture absorption from the environment, all mixes were maintained in tightly sealed bottles.

2.4 DES and aqueous solutions characterisation

The DES and its 2M aqueous solutions were characterised by measuring their physicochemical properties before and after CO_2 absorption (density and viscosity). The density measurements were conducted using Anton Paar DMA 4200 M, at 30 °C and ambient pressure. Viscosity was measured using a BROOKFIELD viscometer at 30, 40 and 50 °C and ambient pressure. The systems were further characterised using FTIR to identify the functional groups and the DES formation.

2.5 CO_2 solubility measurements

The performance evaluation of DESs in absorbing CO_2 was accomplished by the method described by (Kassim et al., 2016). The experimental setup for measuring CO_2 uptake is illustrated in Figure 1. The schematic diagram mainly consists of an air vent tube, a welded stirrer assembly, an inlet gas tube, and a thermocouple. The experiment is initiated by flushing CO_2 through the system to purge the air out of the gas reservoir. Once the reservoir is purified, it is filled with pure CO_2 from the gas tank after that CO_2 is heated and pressurized into the required experimental conditions. The thermostated high-pressurized reactor is filled with a known volume of fresh solutions or DES (20 mL).

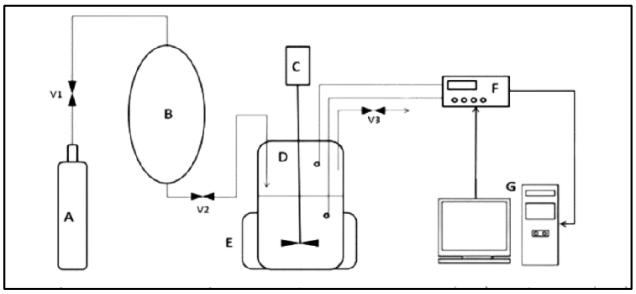

Figure 1. Schematic diagram of the experimental set-up for measuring the CO_2 solubility: A. Gas (CO_2) cylinder, B. Gas (CO_2) reservoir, C. Motor, D. High-pressure reactor vessel (equilibrium cell), E. Heater, F. Reactor controller, G. PC graphical user interface, V1. Control valve, V2. Needle valve, V3. Pressure relief valve.

3. Results and discussion

3.1 Characterisation of DES and its aqueous solution

3.1.1 Density

The densities of the synthesised systems were measured at 30 °C under ambient pressure. The uncertainties in the density data were within a range of ± 0.00001 $g.cm^{-3}$. Previous work data for other synthesised DESs were used for comparison with the values of this work, as shown in Figure 2. The density experimental data showed that the density decreased when HBD (amine or water) was added to the salt (ChOH or ChCl). Additionally, the density decreased as the molar ratio of HBD increased, as shown in the literature-reported data for the MTPB: GLY DES system (Shahbaz, Bagh, & Mjalli, 2013). This might be due to the increase in the repulsion forces between the salt and HBD, which leads to an increase in the volume of the solution as the HBD increases (Pishro, Murshid, Mjalli, & Naser, 2020). Comparing the densities of the studied system before and after carbonation, as shown in Figure 2, the density increased in all the synthesised systems after absorption, where the increase was

DOI: https://doi.org/10.22452/mjs.vol43sp1.5
Malaysian Journal of Science 43 (Special Issue 1): 26-32 (July 2024)

significant, up to approximately 11 % in the solvent that involved both chemical and physical absorption (ChOH: 2-MAE). However, the density increases in (ChOH (2M) and ChCl (2M)) were insignificant which was found to be less than around 2.0 %. This could be due to the chemical absorption influencing the packing or chemical structure of the DES; therefore, because the density depends on the packing or chemical structure of the DES, this can also be applied to explain the increase in density after absorption. In the case of the ChOH: 2-MAE system, the density data are comparable with other reported DESs (Murshid, Mjalli, Naser, Al-Zakwani, & Hayyan, 2019).

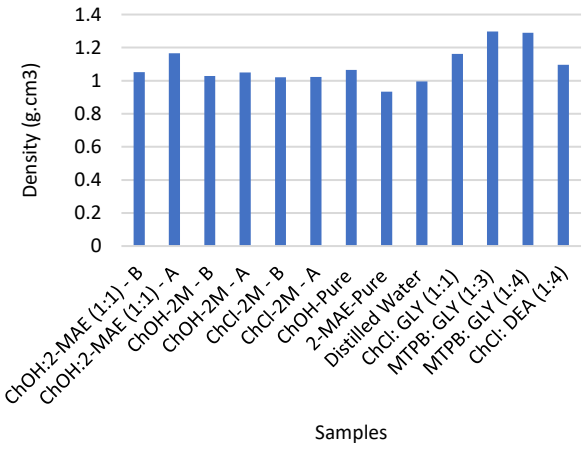

B: Before absorption; A: After absorption;

Figure 2: Density of the studied systems.

3.1.2 Viscosity

Viscosity is an essential solvent property for designing the equipment used in any absorption process. Therefore, the viscosity of 2-MAE-based DES and its aqueous solutions were measured before and after CO_2 absorption at three different temperatures and ambient pressures. The experimental results are listed in Table 1 and illustrated in Figure 3. Some other viscosities of reported DESs are used for comparison with the data of this work, and the viscosities of ChCl: DEA and TBAB: AP are estimated using the experimental models (Murshid et al., 2019; Nowosielski, Jamrógiewicz, Łuczak, Śmiechowski, & Warmińska, 2020).

Based on the reported and experimental results, the DES viscosity depends on the molar ratio, temperature, and type of salts and HBD used. The data showed an exponential decrease in the viscosities of all DESs and aqueous solutions as the temperature increased. This viscosity behaviour is due to the higher temperatures, which increase the kinetic energy of the molecules and ions and weaken the attractive forces between them, allowing the molecules to move easily, thereby decreasing the viscosity. Additionally, based on the reported binary DESs, the viscosity decreased as the molar ratio increased, as can be seen in the case of TBAB: AP DES, where the viscosity decreased by almost 40 % at 30 °C when the molar ratio increased from 1:4 to 1:8.

The viscosity of the solvents used in this study decreased after CO_2 absorption. The viscosities of ChOH: 2-MAE, ChOH, and ChCl decreased at 30 °C by approximately 32, 29, and 13 %, respectively. However, different analogous relations were observed where they reported an increase in the viscosity after absorption for binary and ternary ethanolamine-based DESs (Sarmad, Shokat, & Nikjoo, 2020). For example, the viscosity of ChCl: EA (1:7) increased at 25 °C by almost 16 times that before absorption. Moreover, comparing the studied DES viscosity with other reported DESs, ChOH:2-MAE (1:1) [B] has the second highest value after ChCl: DEA (1:4) [B] with a value of 290.5 cP at 30 °C while the lowest reported is ChCl: EA (1:7) [B] with a value of 32.480 cP at 30 °C. lastly, even though pure amine (2-MAE) has slightly better CO_2 absorption performance compared to ChOH: 2-MAE (1:1), 2-MAE is found to be highly viscous after absorption experiment and can not be measured with the available viscosity equipment in the lab.

Table 1: Viscosity of synthesised and reported DESs as a function of temperature.

Sample Name	Abbr.	Reference
ChOH:2-MAE (1:1)	DES 1 [B]	This work
ChOH:2-MAE (1:1)	DES 1 [A]	This work
ChOH-2M	Soln 1 [B]	This work
ChOH-2M	Soln 1 [A]	This work
ChCl-2M	Soln 2 [B]	This work
ChCl-2M	Soln 2 [A]	This work
ChOH-Pure	Soln 3 [B]	This work
2-MAE-Pure	Soln 4 [B]	This work
ChCl: EA (1:7)	DES 15 [B]	(S. Sarmad, Xie, Mikkola, & Ji, 2017)
TBAB: EA (1:6)	DES 16 [B]	
ChCl: DEA (1:4)	DES 17 [B]	(Murshid et al., 2019)
TBAB: AP (1:4)	DES 18 [B]	(Nowosielski et al., 2020)
TBAB: AP (1:8)	DES 19 [B]	

B: Before absorption; A: After absorption; EA: Ethanolamine; AP: 3-amino-1-propano; TBAB: Tetrabutylammonium bromide; DEA: Diethanolamine.

3.2 CO_2 solubility of DES and aqueous solutions

The solubility of CO_2 in the studied systems, of DES, pure 2-MAE, and 2M aqueous solutions of choline hydroxide, choline chloride, and DES, were determined at 30 °C under the pressure range of 50.0 – 150.0 psi. Figure 4 illustrates all the measured experimental data for all studied systems in mol CO_2/mol solvent. The solubility of CO_2 in DESs appears to be influenced by various factors, including pressure, the characteristics of the hydrogen bond donor (HBD), the alkyl chain length in both HBD and hydrogen bond acceptor (HBA), the properties of salts, the strength of hydrogen bonding within the solutions, the molar ratio, and the molecular weight of the components (S. Sarmad et al., 2017).

DOI: https://doi.org/10.22452/mjs.vol43sp1.5
Malaysian Journal of Science 43 (Special Issue 1): 26-32 (July 2024)

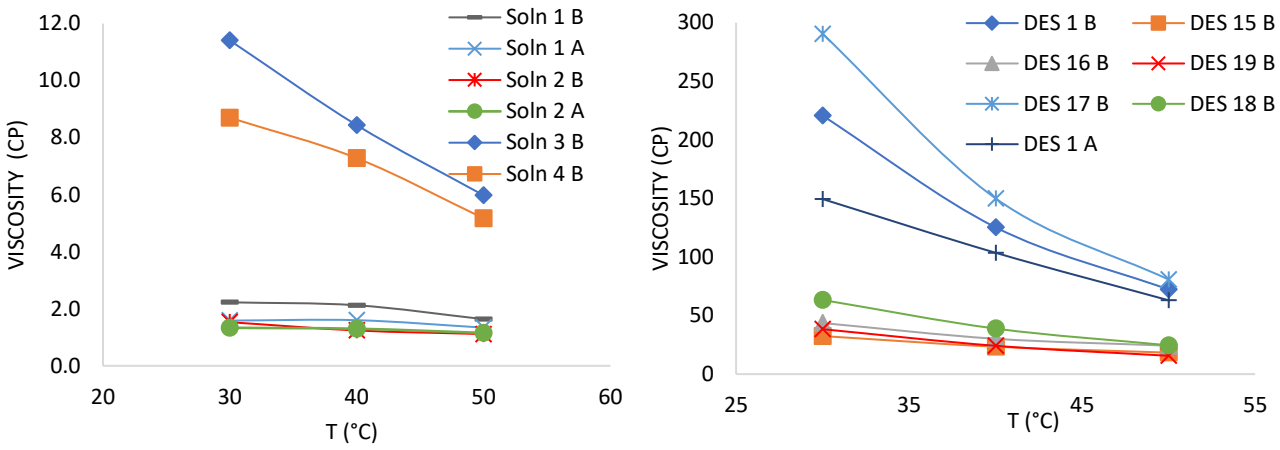

Figure 3: Viscosity of the studied systems and reported DESs as a function of temperature.

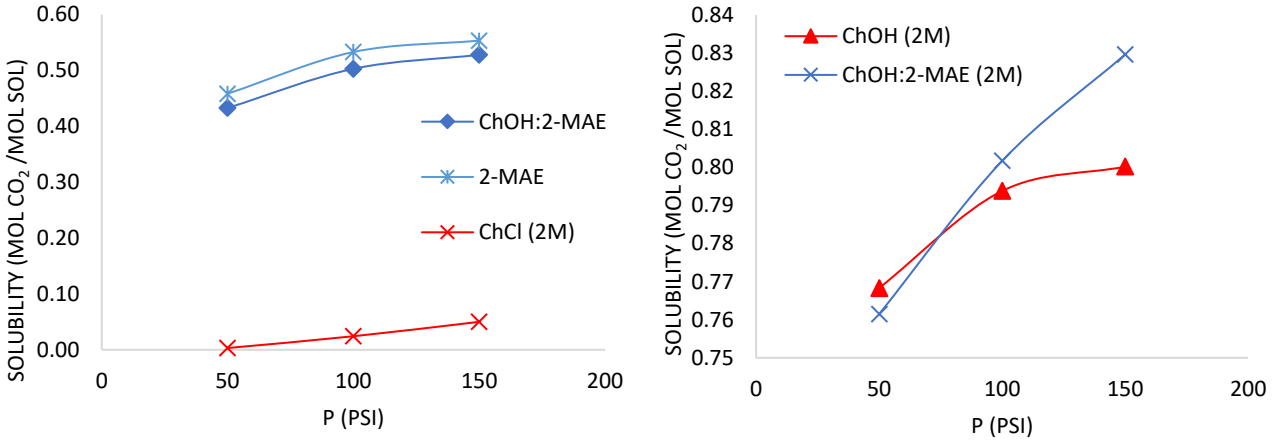

Figure 4: CO_2 solubility in terms of α_{CO2} as a function of pressure at T = 30 °C.

Table 2: Composition and molar ratio of studied DES and other reported DESs.

DES No.	HBA	HBD	Molar ratio (HBA: HBD)	Temperature °C	Reference
DES 1	ChOH	2-MAE	1:1	30	This work
DES 2	ATPPB[1]	DEG[1]	1:4	30	(Ghaedi et al., 2017)
DES 3	ATPPB	DEG	1:10	30	
DES 4	ATPPB	TEG[1]	1:4	30	
DES 5	ATPPB	TEG	1:10	30	
DES 6	ChCl	EA	1:7	25	(Sarmad et al., 2020)
DES 7	ChCl	EA: MDEA[1]	1:7:5	25	
DES 8	TBPB[1]	PhOH[1]	1:4	40	(Wang et al., 2019)
DES 9	ATPPB	PhOH	1:4	40	

ATPPB: Allyltriphenyl phosphonium bromide; EA: Ethanolamine; MDEA: Methyldiethanolamine; DEG: Diethylene glycol; TEG: Triethylene glycol; TBPB: Tetrabutylphosphonium bromide; PhOH: phenol.

DOI: https://doi.org/10.22452/mjs.vol43sp1.5
Malaysian Journal of Science 43 (Special Issue 1): 26-32 (July 2024)

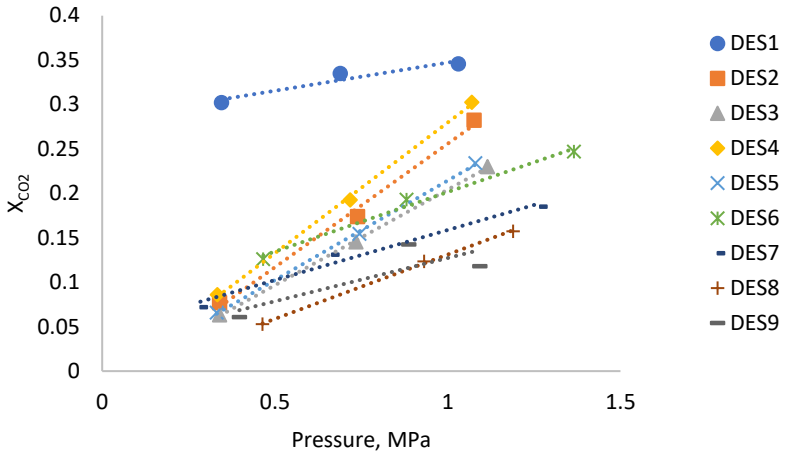

Figure 5: CO_2 solubility in mole fraction ($\mathbf{X_{CO2}}$) as a function of pressure in synthesized and reported DESs at T = 30 °C, 25 °C, and 40 °C.

The described findings demonstrate that the tested system's capability for CO_2 absorption maintains consistency at the observed temperature. As seen in the two figures, there is a linear trend between pressure increases and the solubility of CO_2 in all solvents. This trend shows that physical absorption is the prominent route by which CO_2 is absorbed by the solvents. The absorption of pure 2-MAE, amine-based DES, and its aqueous solution, on the other hand, is mediated by a mix of chemical and physical processes. Therefore, based on the measured experimental data of the systems studied, the performance order is ChOH: 2-MAE (2M) > ChOH (2M) > 2-MAE > ChOH: 2-MAE > ChCl (2M). It is worthwhile to compare the solubility of CO_2 between the studied DES (ChOH:2-MAE) and reported DESs. The absorption capacities of various DESs were studied based on different HBA and HBD. Table 2 and Figure 5 list and illustrate CO_2 solubility in mole fraction ($\mathbf{X_{CO2}}$) as a function of pressure. Hence, based on the tabulated data, the data reported corresponds with the literature finding where all DESs demonstrated an increase in the CO_2 absorption capacity as the pressure is increased. Additionally, it can be concluded that the studied DES (ChOH:2-MAE) has good performance compared with other reported DESs and it can be considered as a promising DES.

3.3 FTIR

Figure 6 (a) and (b) illustrate the FTIR spectra for 2M Choline chloride and 2M choline hydroxide solution before and after CO_2 absorption. The major peaks are tabulated and listed in Table 3. For both 2M Choline chloride and 2M choline hydroxide solutions, the broad absorption peak at 3302 cm^{-1} is characteristic of the O–H stretching vibration of choline hydroxide. The peak at 1481 cm^{-1} is due to the C–H bending vibration of alkanes. The peaks at 1296 and 1088 cm^{-1} were attributed to the C–N and C–O stretching vibrations, respectively. As shown in Figure 6 (a), no significant difference was observed in the spectra of the choline chloride solution before and after CO_2 absorption. In contrast, the spectrum for 2M choline hydroxide shows a peak at 1351 cm^{-1}, which is characterised by HCO_3^- formed during the CO_2 absorption process. Figure 6 (c) shows the FTIR spectra of pure 2-MEA before and after CO_2 absorption. Major peaks are tabulated and assigned in Table 3. The spectra show the presence of carbonate peaks that reflect the formation of the carbamate salt of 2-MAE after absorption of CO_2 at 1378, 1296, and 1259 cm^{-1}. Figure 6 (d) illustrates the FTIR spectra for pure ChOH:2-MAE; before and after CO_2 absorption. Major peaks are tabulated and assigned in Table 3. The spectra showed peaks that were found in the respective singular components; however, some peaks may overlap. Owing to the large number of absorbing species in the infrared spectra, it is difficult to accurately assign all absorption bands. Some bands were close to each other, very broad, and/or strongly overlapping.

4. Conclusion

In this study, we successfully synthesised a 2 (methylamino)ethanol (2-MAE)-based deep eutectic solvent (DES) and a corresponding 2M aqueous solution. Our evaluation focused on the CO_2 absorption capacity at 30 °C and pressures reaching 150 psi. Furthermore, we conducted comprehensive characterisations of both the prepared solutions and the DES, encompassing measurements of their physicochemical properties, density, viscosity, and FTIR analysis. The results revealed a linear correlation between the CO_2 absorption capacity and increasing pressure across all the solvents tested. Notably, compared to other reported DESs, ChOH:2-MAE exhibited a promising performance. Pre- and post-absorption measurements of the physicochemical properties of the studied systems were conducted, in addition to comparisons with other reported DESs. FTIR analysis of the studied systems after absorption indicated the formation of carbamate. This research highlights the promising performance of the studied DES compared with the conventional amine (2-MAE) solvent and other reported DESs.

5. Acknowledgement

The author would like to express acknowledgement to Sunway University for granting this project under Internal Grant Scheme (IGS) 2022 (GRTIN-IGS-CCDCU[2]-08-2022).

DOI: https://doi.org/10.22452/mjs.vol43sp1.5
Malaysian Journal of Science 43 (Special Issue 1): 26-32 (July 2024)

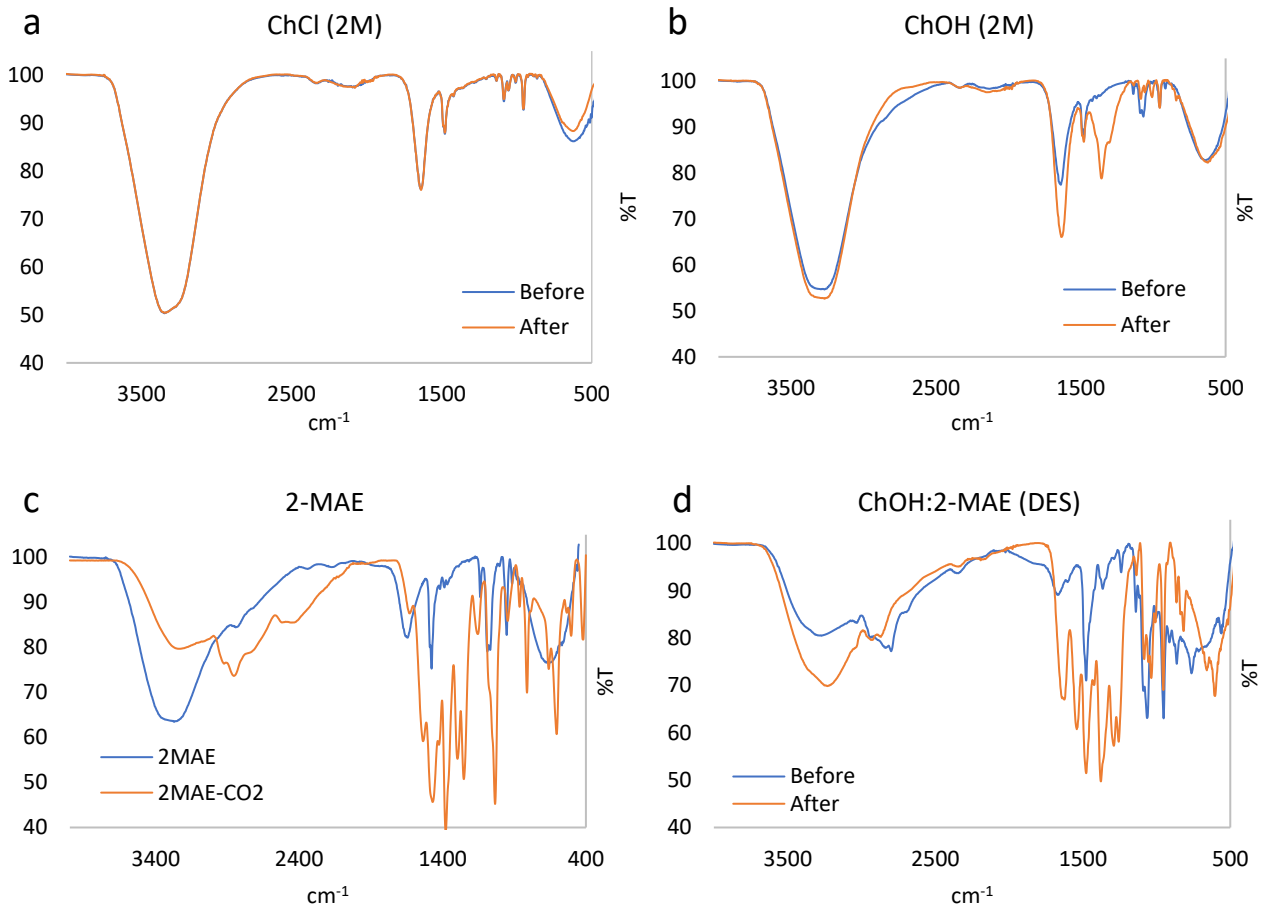

Figure 6: FTIR spectra of DES and 2M aqueous solutions; a: ChCl (2M); b: ChOH (2M); c: pure 2-MAE; c: ChOH:2-MAE (DES)

Table 3: IR peak assignment for the studied systems.

Assignment	ChCl (2M)		ChOH (2M)		2-MAE		ChOH:2-MAE	
	Peak	Frequency	Peak	Frequency	Peak	Frequency	Peak	Frequency
-OH, -NH stretching	50.5	3334	54.8	3278	64.0	3234	81.0	3227
-NH bending	76.2	1637	78.2	1631	84.3	1626	91.8	1621
-CH_2-OH bending	87.8	1479	87.5	1477	81.0	1470	71.1	1477
-C-N- bending	94.5	1085	-	-	-	-	-	-
-C-O- bending	97.1	1051	-	-	-	-	-	-
Carbonates band	-	-	78.9, 86.7	1356, 1304	-	-	-	-
Carbamates band	-	-	-	-	39.1	1378	49.8	1378
-CH_2-, -CH_3 stretching	-	-	-	-	84.7, 84.6	2896, 2847	80.0,8 0.1	2917, 2860
stretching of NCOO–	-	-	-	-	55.3, 54.0	1296, 1259	57.4,5 8.1	1287, 1256
-NH-CO_2	-	-	-	-	83.0	1153	-	-

DOI: https://doi.org/10.22452/mjs.vol43sp1.5
Malaysian Journal of Science 43 (Special Issue 1): 26-32 (July 2024)

6. References

Agency, E. P. (2021, April 14). *Overview of Greenhouse Gases*. Retrieved from https://www.epa.gov/ghgemissions/overview-greenhouse-gases

Anderson, T. R., Hawkins, E., & Jones, P. D. (2016). CO_2, the greenhouse effect and global warming: from the pioneering work of Arrhenius and Callendar to today's Earth System Models. *Endeavour, 40*(3), 178-187.

Chen, C.-C., Huang, Y.-H., Hung, S.-M., Chen, C., Lin, C.-W., & Yang, H.-H. (2021). Hydrophobic deep eutectic solvents as attractive media for low-concentration hydrophobic VOC capture. *Chemical Engineering Journal, 424*, 130420.

Chen, P.-C., & Lin, S.-Z. (2018). Optimization in the Absorption and Desorption of CO_2 Using Sodium Glycinate Solution. *Applied Sciences, 8*, 2041.

Dincer, I., & Abu-Rayash, A. (2020). Chapter 1 - Fundamental aspects of energy, environment, and sustainability. In I. Dincer & A. Abu-Rayash (Eds.), *Energy Sustainability* (pp. 1-18): Academic Press.

Ghaedi, H., Ayoub, M., Sufian, S., Shariff, A. M., Hailegiorgis, S. M., & Khan, S. N. J. J. o. M. L. (2017). CO_2 capture with the help of Phosphonium-based deep eutectic solvents. *243*, 564-571.

Hussin, F., Aroua, M. K., & Yusoff, R. (2021). Adsorption of CO_2 on palm shell based activated carbon modified by deep eutectic solvent: Breakthrough adsorption study. *Journal of Environmental Chemical Engineering, 9*(4), 105333.

IEA, C. (2023). *Net Zero Roadmap: A Global Pathway to Keep the 1.5 °C Goal in Reach, IEA, Paris*. Retrieved from https://www.iea.org/reports/net-zero-roadmap-a-global-pathway-to-keep-the-15-0c-goal-in-reach

Kassim, M. A., Sairi, N. A., Yusoff, R., Alias, Y., & Aroua, M. K. (2016). Evaluation of 1-Butyl-3-methylimidazolium Bis(trifluoromethylsulfonyl)imide–Alkanolamine Sulfolane-Based System as Solvent for Absorption of Carbon Dioxide. *Industrial & Engineering Chemistry Research, 55*(29), 7992-8001.

Murshid, G., Mjalli, F. S., Naser, J., Al-Zakwani, S., & Hayyan, A. (2019). Novel diethanolamine based deep eutectic mixtures for carbon dioxide (CO_2) capture: synthesis and characterisation. *Physics and Chemistry of Liquids, 57*(4), 473-490.

Nanda, S., Reddy, S. N., Mitra, S. K., & Kozinski, J. A. (2016). The progressive routes for carbon capture and sequestration. *4*(2), 99-122.

Nowosielski, B., Jamrógiewicz, M., Łuczak, J., Śmiechowski, M., & Warmińska, D. (2020). Experimental and predicted physicochemical properties of monopropanolamine-based deep eutectic solvents. *Journal of Molecular Liquids, 309*, 113110.

Pishro, K. A., Murshid, G., Mjalli, F. S., & Naser, J. (2020). Investigation of CO_2 solubility in monoethanolamine hydrochloride based deep eutectic solvents and physical properties measurements. *Chinese Journal of Chemical Engineering, 28*(11), 2848-2856.

Sarmad, Shokat, & Nikjoo. (2020). Amine functionalized deep eutectic solvent for CO_2 capture: Measurements and modeling. *Journal of Molecular Liquids,* 309, 113159.

Sarmad, S., Xie, Y., Mikkola, J.-P., & Ji, X. (2017). Screening of deep eutectic solvents (DESs) as green CO_2 sorbents: from solubility to viscosity. *New Journal of Chemistry, 41*(1), 290-301.

Shahbaz, Bagh, & Mjalli. (2013). Prediction of refractive index and density of deep eutectic solvents using atomic contributions. *Fluid Phase Equilibria, 354*, 304-311.

Smith, E. L., Abbott, A. P., & Ryder, K. S. (2014). Deep Eutectic Solvents (DESs) and Their Applications. *Chemical Reviews, 114*(21), 11060-11082.

Suzuki, Y. (2018). Asymmetric Michael Addition Mediated by Chiral Ionic Liquids. *Mini-reviews in organic chemistry, 15*(3), 236-245.

Tomé, L. I. N., Baião, V., da Silva, W., & Brett, C. M. A. (2018). Deep eutectic solvents for the production and application of new materials. *Applied Materials Today, 10*, 30-50.

Wang, J., Cheng, H., Song, Z., Chen, L., Deng, L., & Qi, Z. (2019). Carbon Dioxide Solubility in Phosphonium-Based Deep Eutectic Solvents: An Experimental and Molecular Dynamics Study. *Industrial & Engineering Chemistry Research, 58*(37), 17514-17523.

Zhang, Q., De Oliveira Vigier, K., Royer, S., & Jérôme, F. (2012). Deep eutectic solvents: syntheses, properties and applications. *Chemical Society Reviews, 41*(21), 7108-7146.

Zubeir, L. F., Lacroix, M. H. M., Meuldijk, J., Kroon, M. C., & Kiss, A. A. (2018). Novel pressure and temperature swing processes for CO_2 capture using low viscosity ionic liquids. *Separation and Purification Technology, 204*, 314-327.

Zurob, E., Cabezas, R., Villarroel, E., Rosas, N., Merlet, G., Quijada-Maldonado, E., . . . Plaza, A. (2020). Design of natural deep eutectic solvents for the ultrasound-assisted extraction of hydroxytyrosol from olive leaves supported by COSMO-RS. *Separation and Purification Technology, 248*, 117054.

DOI: https://doi.org/10.22452/mjs.vol43sp1.5
Malaysian Journal of Science 43 (Special Issue 1): 26-32 (July 2024)

MALAYSIAN JOURNAL OF SCIENCE
MJS
ISSN 1394 - 3065

2nd Euro-Asia Conference on CO_2 Capture and Utilization (EACCO2CU2022) Special issue

Malaysian Journal of Science 43 (Special Issue 1): 33-37 (July 2024) https://mjs.um.edu.my

PRELIMINARY STUDY ON PERFORMANCE OF Zn-DOPED ZEOLITE IN LOW-TEMPERATURE CO_2 ADSORPTION

Ang Gaun Yu[1a], Zhi Hua Lee[2ab*], Chee Yung Pang[3a] and Gulnaziya Issabayeva[4ab]

Abstract: Zeolite has been identified as a potential low-temperature CO_2 adsorbent with the highest adsorption capacity among adsorbents in its category. However, its adsorption capacity remains relatively low, limiting its industrial application for CO_2 adsorption. Additionally, there is a need to increase the optimal adsorption temperature of this porous material to effectively adsorb CO_2 emitted from flue gas, which has an average temperature of 100 - 125°C. To address these challenges, a preliminary study on Zn-doped zeolite has been conducted. This study aims to investigate the ability of Zn-doped zeolite to enhance CO_2 adsorption capacity and its effect on the optimal temperature for CO_2 adsorption. Zinc-doped zeolite was synthesized by doping zinc oxide into natural zeolite using a zinc ion exchange method at different doping concentrations (0.2 M & 1.0 M). Undoped natural zeolite was studied as a benchmark. Their CO_2 adsorption performance was tested using TGA at 30°C, 50°C, and 100°C. The effects of temperature and doping concentration on adsorption capacity were investigated. The adsorbent samples were characterized using X-ray Diffraction (XRD) and Scanning Electron Microscopy (SEM) with Energy Dispersive X-ray (EDX) analysis. It was found that increasing the temperature from 30°C to 50°C increased the CO_2 adsorption capacity, but the capacity decreased when the temperature was further increased to 100°C. Furthermore, increasing the doping concentration tended to enhance the CO_2 adsorption capacity. The highest adsorption capacity of 0.0281 g CO_2/g sorbent was observed in zinc-doped zeolite with a 1.0 M doping concentration at 50°C. The improvement was mainly attributed to the zinc oxide doped on the zeolite, which provided a functional group that formed chemical bonds with CO_2. This study also found that the adsorption rate of CO_2 was predominantly influenced by temperature, while the effect of doping concentration was less significant. All testing and characterization results suggested that the zinc-ion exchange method improved the CO_2 adsorption capacity of zeolite.

Keywords: Zeolite, CO_2 adsorption, adsorption capacity, low temperature.

1. Introduction

Global warming has become a serious global threat, primarily caused by the greenhouse effect, where greenhouse gases accumulate in the atmosphere, increasing the Earth's average surface temperature (Klugmann-Radziemska, 2022). Approximately 400 million tons of carbon dioxide (CO_2) are emitted annually from human activities, making it the primary greenhouse gas (Sharma et al., 2022). To address global warming, CO_2 capture has emerged as a direct approach to mitigate its adverse effects on ecosystems and human societies.

Zeolite has been identified as a potential CO_2 adsorbent due to its low cost, mild regeneration conditions, and stability during the adsorption process (Rajakrishnamoorthy et al., 2023). It possesses excellent properties, including a very high BET surface area, thermal stability (Pham et al., 2016), and a tunable structure (Jha & Singh, 2016) suitable for various applications. Notably, zeolite has the highest adsorption capacity among low-temperature range CO_2 adsorbents, such as activated carbon. Research has shown that zeolite achieves its highest adsorption capacity at 25°C, suggesting its suitability for low-temperature CO_2 capture (Chen et al., 2023).

However, its adsorption capacity remains relatively low compared to high-temperature range adsorbents like calcium oxide, limiting its industrial application for CO_2 adsorption. This porous material needs to increase the optimal adsorption temperature for adsorbing CO_2 emitted from flue gas, which averages 100 - 125°C. Given the tunable properties of zeolite, this study investigates zeolite doped with zinc oxide. Zinc was selected as the metal-based dopant due to its low cost, non-toxicity, high stability, and wide availability (Munawar et al., 2020). Additionally, zinc-doped zeolitic imidazolate framework-67 (ZIF-67) has shown enhanced water stability (Qian et al., 2018), an important characteristic for CO_2 adsorbents used in flue gas containing water vapor. Zn-doped CHA-type zeolite has demonstrated better kinetics and absorbability for low-concentration (400 ppm) CO_2 adsorption compared to 13X-zeolites (Fu et al., 2022).

In this paper, a preliminary study was conducted on Zn-doped zeolite for pure CO_2 adsorption. Undoped zeolite was

Authors information:
[a]Department of Chemical Engineering, Lee Kong Chian Faculty of Engineering and Science, Universiti Tunku Abdul Rahman (Sungai Long Campus), Bandar Sungai Long, Cheras, 43000 Kajang, Selangor Darul Ehsan, MALAYSIA. E-mail: yuanggaun@1utar.my[1]; pcy1997@1utar.my[3]
[b]Centre for Advanced and Sustainable Materials Research (CASMR), Universiti Tunku Abdul Rahman (Sungai Long Campus), Bandar Sungai Long, Cheras, 43000 Kajang, Selangor Darul Ehsan, MALAYSİA. E-mail: gulnaziya@utar.edu.my[4]

*Corresponding Author: leezh@utar.edu.my[2]

Received: February 7, 2024
Accepted: May 7, 2024
Published: July 31, 2024

DOI: https://doi.org/10.22452/mjs.vol43sp1.6
Malaysian Journal of Science 43 (Special Issue 1): 33-37 (July 2024)

used as a benchmark. The study aims to investigate the ability of Zn-doped zeolite to enhance CO_2 adsorption capacity and its effect on the optimal temperature for CO_2 adsorption. Natural zeolite was used, and the scope includes examining the effects of temperature and Zn-doping concentration on the CO_2 adsorption capacity of the adsorbents.

2. Materials and methods

Natural zeolite in granular form and zinc hydroxide were supplied by R & M Chemicals and Bendosen, respectively. These chemicals were used without further purification or treatment. Zinc hydroxide solutions at different concentrations (0.2 M and 1.0 M) were prepared by dissolving zinc hydroxide in distilled water.

2.1 Sample Preparation

In total, 5 g of zeolite was mixed with 100 ml of 0.2 M zinc hydroxide solution. The mixture was stirred and heated at 70°C for 2 hours to increase the diffusion rate of the zinc ion into the zeolite structure for ion exchange. The mixture was then filtered to separate the treated zeolite in solid form from the solution, followed by continuous rinsing with distilled water. The wet treated zeolite was dried in an oven at 80°C overnight. After drying, the zeolite was calcined in a furnace at 270°C for 4 hours. The synthesis procedure was repeated using a 1.0 M zinc hydroxide solution. This study treated natural zeolite with zinc hydroxide at two different concentrations: 0.2 M and 1.0 M.

2.2 CO_2 Adsorption Performance

To examine the adsorption performance of the natural and zinc-doped zeolite, CO_2 adsorption experiments were conducted using a thermogravimetric analyzer (TGA, Perkin Elmer Simultaneous Thermal Analyzer 8000). TGA combines a microbalance and a furnace chamber, allowing the weight change of a sample placed in the furnace chamber to be recorded with changes in temperature and time under a specific gas flow. In this study, the adsorbent sample was held at a preset adsorption temperature under the flow of pure CO_2. The weight change of the adsorbent samples was recorded until stabilization. The experimental testing flow diagram is illustrated in Figure 1.

Approximately 20 mg ± 0.5 mg of the sample was loaded into the TGA. The sample was heated from ambient temperature to 500°C at 10°C/min under a 30 mL/min flow of pure NO_2 and held for 10 minutes as a pre-treatment to remove any water vapor and impurities. The sample was then cooled to the adsorption temperature at a rate of 20°C/min, and CO_2 flow was initiated upon reaching the desired adsorption temperature. The temperature was held at 100°C for 2 hours. The weight changes in the adsorbent during the adsorption process were recorded. Since zeolite-based adsorbents adsorb CO_2 without losing weight by forming by-products, the CO_2 adsorption capacity was determined by calculating the sample's weight percentage increase. The unit of adsorption capacity was converted to g/g by dividing the initial weight percentage, as shown in Eq (1).

$$Adsorption\ Capacity\ \left(\frac{g}{g}\right) = \frac{Final\ Weight\ \% - Initial\ Weight\ \%}{Initial\ Weight\ \%} \quad (1)$$

To determine the optimum CO_2 adsorption temperature, the sample was analysed over different temperatures at which CO_2 started to flow in at 30°C, 50°C and 100°C.

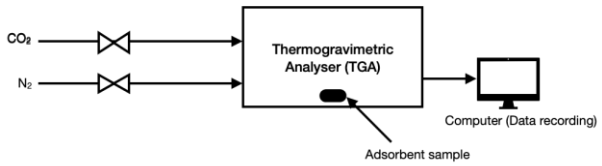

Figure 1 Schematic diagram of thermogravimetric analyzer setup in CO_2 adsorption performance testing.

2.3 Characterisation

The sample's surface morphology and element composition were derived using Hitachi S-3400N SEM with an accelerating voltage of 15 kV. The XRD pattern of the sample was recorded at room temperature using Shimadzu 6000. The analysis was conducted in the 2θ range of 20° to 80° using Cu-Kα radiation. The XRD pattern was interpreted to determine the presence of zinc oxide and its intensity.

3. Results and discussion

3.*1 Effect of Adsorption Temperature*

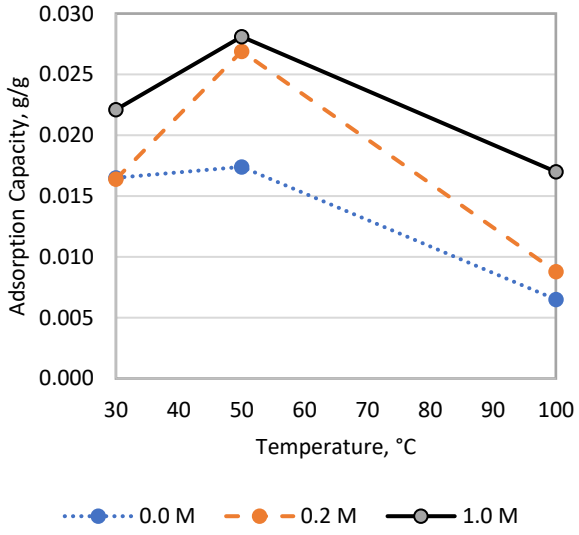

Figure 2. CO_2 adsorption capacities of undoped natural zeolite (0.0 M), doped natural zeolite treated with 0.2 M and 1.0 M of zinc hydroxide solution.

The adsorption capacities of the undoped natural zeolite and zinc-doped natural zeolite treated with 0.2 M and 1.0 M zinc hydroxide solutions are depicted in Figure 2. All adsorbent samples exhibited a similar trend: adsorption capacities increased with the initial rise in adsorption temperature, then decreased when the temperature was further increased to

DOI: https://doi.org/10.22452/mjs.vol43sp1.6
Malaysian Journal of Science 43 (Special Issue 1): 33-37 (July 2024)

100°C. Additionally, the increment in the adsorption capacity of untreated natural zeolite from 30°C to 50°C was not significant.

Theoretically, zeolite is a physical adsorbent that adsorbs CO_2 through van der Waals forces. Physical adsorbents have higher adsorption capacities at lower temperatures because higher temperatures weaken van der Waals forces (Zhang et al., 2023). This can be observed in the adsorption curve of natural zeolite in Figure 2. It has the highest adsorption capacity at low temperatures, with a slight increase at 50°C, but its adsorption capacity decreased to around 0.0065 g/g when the temperature was raised to 100°C.

However, doping natural zeolite with zinc oxide introduces chemical adsorption (chemisorption) as a contributing factor to CO_2 adsorption (Kusumastuti et al., 2019). Chemisorption requires slightly higher temperatures to gain enough activation energy for zinc oxide to form chemical bonds with CO_2 (Hagen, 2015). This explains why the increments in adsorption capacity from 30°C to 50°C for zinc-doped zeolite, as observed in Figure 2, are more significant and higher than those of natural zeolite. When the temperature further increased to 100°C, the van der Waals forces and the chemical interaction between zeolite and CO_2 weakened, decreasing adsorption capacity (Kusumastuti et al., 2019).

Since the activation energy for physisorption is low, the increase in the adsorption capacity of undoped natural zeolite from 30°C to 50°C is not significant. This minor increment can be attributed to the temperature difference not being large enough to substantially weaken the van der Waals forces.

3.2 Effect of Doping Concentration

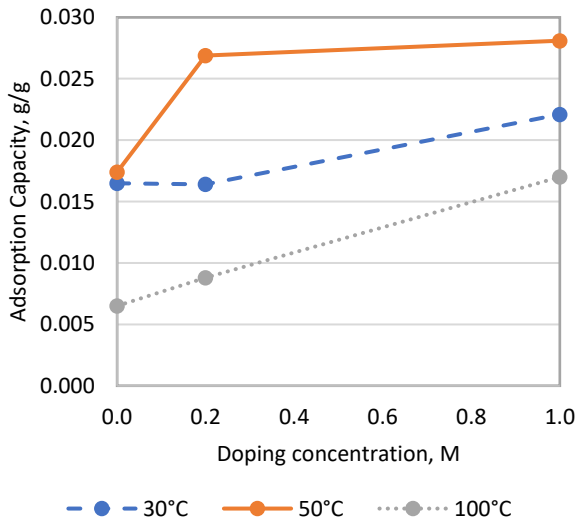

Figure 3. Comparison graph of adsorption capacity and doping concentration of the zeolite-based adsorbent samples.

Besides the effect of temperature, the CO_2 adsorption capacity is also influenced by the doping concentration. Figure 3 illustrates the relationship between adsorption capacity and doping concentration for the zeolite-based adsorbent samples.

According to Figure 3, the CO_2 adsorption capacity increases with doping concentration. This is because a higher doping concentration results in more zinc ions binding to the zeolite as extra-framework cations, which increases the amount of zinc oxide formed during calcination (Huong & Lee, 2017). Zinc oxide then forms chemical bonds with CO_2 (Gankanda et al., 2016), leading to an increased adsorption capacity as more CO_2 is adsorbed.

Additionally, Figure 3 shows that the increase in adsorption capacity for zinc-doped zeolite at 50°C was relatively low compared to 30°C and 100°C after the doping concentration of 0.2 M. As previously mentioned, CO_2 adsorption on zinc-doped zeolite is a combination of physisorption and chemisorption. At 50°C, both physisorption and chemisorption contribute significantly to CO_2 adsorption. When the doping concentration increases, the amount of zinc oxide doped onto the zeolite also increases, which can be confirmed by XRD and SEM results. However, when the amount of zinc oxide reaches a certain level, excess zinc oxide can lead to pore blockage, creating diffusion resistance and preventing CO_2 from being adsorbed (Bezerra et al., 2014). This results in a plateau in CO_2 adsorption capacity, as the contribution from physisorption ceases. Therefore, further increases in doping concentration at 50°C only yield minor improvements in CO_2 adsorption capacity.

This phenomenon was observed only at 50°C because it is the optimum temperature for CO_2 adsorption on zinc-doped zeolite. At this temperature, zinc-doped zeolite exhibited a higher CO_2 adsorption capacity compared to other temperatures, so the increase in adsorption capacity from 0.2 M to 1.0 M was not as significant as at other temperatures.

3.3 Characterisation

3.3.1 X-ray Diffraction (XRD)

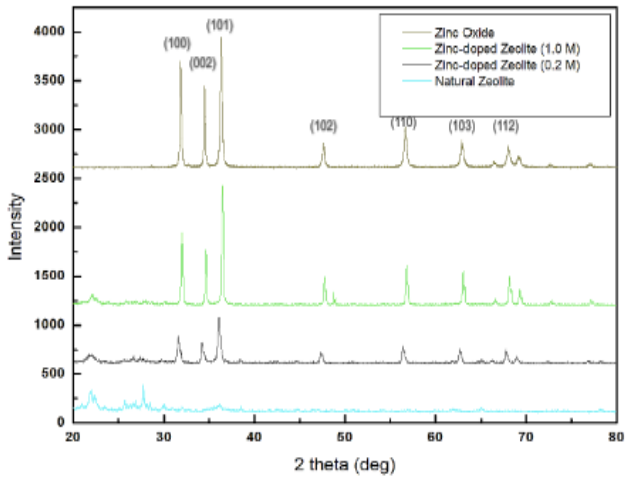

Figure 4. XRD diffractogram of zeolite-based adsorbent samples studied and pure ZnO.

The results of XRD are represented by the XRD diffraction patterns shown in Figure 4. The peaks observed in the zinc-doped zeolite (0.2 M and 1.0 M) XRD patterns are almost identical to the peaks found in the raw zinc oxide XRD pattern

DOI: https://doi.org/10.22452/mjs.vol43sp1.6
Malaysian Journal of Science 43 (Special Issue 1): 33-37 (July 2024)

(RRUFF Project, 2018). The major characteristic peaks attributed to zinc oxide appear at 2θ values of 31.8°, 34.5°, 36.3°, 47.6°, 56.6°, 62.9°, 66.4°, 68.0°, and 69.1°. This indicates that zinc oxide was successfully doped onto the zeolite structure through zinc ion exchange.

Additionally, comparing the patterns of 0.2 M and 1.0 M zinc-doped zeolite reveals that the peak intensity of 1.0 M zinc-doped zeolite is higher than that of 0.2 M zinc-doped zeolite. This is because a higher doping concentration leads to more zinc oxide formation, resulting in higher peak intensity. Consequently, the higher peak intensity in 1.0 M zinc-doped zeolite indicates a greater amount of zinc oxide, which provides more functional groups for CO_2 adsorption, thereby resulting in higher CO_2 adsorption capacity (Gankanda et al., 2016).

3.3.2 Scanning Electron Microscopy (SEM)

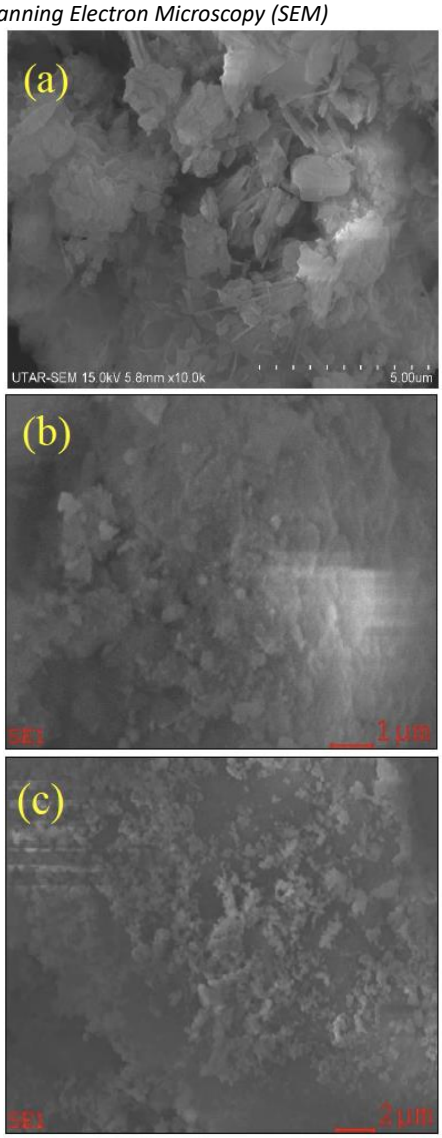

Figure 5. SEM Image of (a) Natural Zeolite, (b) 0.2 M Zinc-doped Zeolite and (c) 1.0 M Zinc-doped Zeolite

Figure 5 exhibits the SEM images of natural zeolite and zinc-doped zeolite. Natural zeolite displays a needle-like morphology with agglomerates, explaining its low adsorption capacity due to the limited number of pores and low pore size. In contrast, zinc-doped zeolite shows a granular morphology with numerous clusters. Additionally, many small granules are visibly distributed over the surface of the structure, suggesting that zinc oxide particles have been successfully doped onto the zeolite.

3.3.4 Energy Dispersive X-ray (EDX)

The EDX results, detailing the elemental composition of O, Al, Si, K, and Zn for all samples, are shown in Table 1. These results confirm the successful doping of zinc oxide into the raw zeolite through zinc ion exchange, evidenced by the atomic percentage of zinc (Zn). While natural zeolite contains no zinc, zinc-doped zeolite with 0.2 M and 1.0 M doping concentrations contain 3.74 at% and 8.46 at%, respectively.

Additionally, the atomic percentage of silicon (Si) decreased following zinc doping, indicating that the doping process primarily involved the exchange of silicon ions with zinc ions. Silicon ions at the center of the zeolite structure are not exposed to CO_2 molecules and thus do not contribute to CO_2 adsorption (Huong & Lee, 2017). By exchanging Si ions with Zn ions, the zinc ions present within the zeolite facilitate zinc oxide formation on the surface during calcination, providing functional groups for chemical bonding with CO_2 (Gankanda et al., 2016). Consequently, the CO_2 adsorption capacity of zinc-doped zeolite is higher compared to natural zeolite.

Table 1. EDX analysis of the adsorbent samples

	Element, at%					
Adsorbent Samples	**O**	**Al**	**Si**	**K**	**Zn**	**Si/Al ratio**
Natural zeolite	61.18	4.43	32.94	0.95	0	7.4
0.2 M Zinc-doped zeolite	57.45	6.68	30.71	1.42	3.74	4.6
1.0 M Zinc-doped zeolite	55.99	4.97	29.71	0.86	8.46	6.0

By comparing their Si/Al ratio, natural zeolite has the highest ratio of 7.4. A high Si/Al ratio is preferable, since the higher the ratio, the higher thermal stability and hydrophobicity (Jha & Singh, 2016). Natural zeolite is more resistant to thermal degradation and moisture than zinc-doped zeolite.

4. Conclusion

Zinc-doped zeolite was successfully synthesized, tested, and characterized as a CO_2 adsorbent. The CO_2 adsorption capacity of zinc-doped zeolite increased as the temperature rose from 30°C to 50°C but decreased when the temperature further increased to 100°C. Compared to natural zeolite, there was a significant improvement in CO_2 adsorption capacity for zinc-doped zeolite. The highest adsorption capacity of 0.0281 g CO_2/g sorbent was observed in zinc-doped zeolite with 1 M doping concentration at 50°C. This capacity was approximately 1.6 times higher than natural zeolite and 1.04 times higher than 0.2 M zinc-doped zeolite, indicating that higher doping concentrations lead to increased adsorption capacity. The improvement in CO_2

DOI: https://doi.org/10.22452/mjs.vol43sp1.6
Malaysian Journal of Science 43 (Special Issue 1): 33-37 (July 2024)

adsorption capacity was primarily due to the additional chemical interactions after doping zeolite with zinc oxide. The optimum temperature and doping concentration for the highest adsorption capacity were 50°C and 1.0 M, respectively.

Additionally, the adsorption kinetics of zeolite were studied. It was found that the adsorption rate of natural zeolite decreased as the temperature increased due to its physisorption nature. Conversely, the adsorption rate of zinc-doped zeolite increased as the temperature rose from 30°C to 50°C but decreased when the temperature reached 100°C. This behavior is attributed to the combination of physisorption and chemisorption in CO_2 adsorption. The difference in adsorption rate between 0.2 M and 1.0 M doping concentrations was insignificant, indicating that the adsorption rate was influenced by temperature but not significantly affected by doping concentration. In conclusion, although the improvement in CO_2 adsorption capacity through zinc ion exchange is still insufficient for industrial application, this novel approach shows promise and can be utilized for further research.

5. Acknowledgement

The authors would like to acknowledge for the financial support given by Universiti Tunku Abdul Rahman Research Fund (UTARRF) (Project No.: IPSR/RMC/UTARRF/2022-C2/L02).

6. References

Bezerra, D. P., Silva, F. W. M. da, Moura, P. A. S. de, Sousa, A. G. S., Vieira, R. S., Rodriguez-Castellon, E., & Azevedo, D. C. S. (2014). CO_2 adsorption in amine-grafted zeolite 13X. Applied Surface Science 314 : 314–321.

Chen, C., Yu, J., Song, G., & Che, K. (2023). Desorption performance of commercial zeolites for temperature-swing CO_2 capture. Journal of Environmental Chemical Engineering 11(3): 110253.

Fu, D., Park, Y., & Davis, M. E. (2022). Zinc Containing Small-Pore Zeolites for Capture of Low Concentration Carbon Dioxide. Angewandte Chemie International Edition 61(5): e202112916.

Gankanda, A., Cwiertny, D. M., & Grassian, V. H. (2016). Role of Atmospheric CO_2 and H_2O Adsorption on ZnO and CuO Nanoparticle Aging: Formation of New Surface Phases and the Impact on Nanoparticle Dissolution. The Journal of Physical Chemistry C 120(34): 19195–19203.

Hagen, J. (2015). Industrial Catalysis: A Practical Approach. 3rd ed. New Jersey: John Wiley & Sons.

Hauchhum, L., & Mahanta, P. (2014). Carbon dioxide adsorption on zeolites and activated carbon by pressure swing adsorption in a fixed bed. International Journal of Energy and Environmental Engineering 5(4): 349-356.

Huong, P.-T. & Lee, B.-K. (2017). Improvement of selective separation of CO_2 over N_2 by transition metal–exchanged. Microporous and Mesoporous Materials 241: 155-164.

Jha, B. & Singh, D. N. (2016). Advanced Structured Materials. 1st ed. Singapore: Springer.

Klugmann-Radziemska, E. (2022). 9.10 - The Environmental Benefits of Photovoltaic Systems: The Impact on the Environment in the Production of Photovoltaic Systems: With a Focus on Metal Recovery. In T. M. Letcher (Ed.), Comprehensive Renewable Energy (Second Edition), pp. 140–151. Oxford: Elsevier.

Kusumastuti, R., Sriyono, Pancoko, M., Butar-Butar, S-L., Putra, G.E., and Tjahjono, H. (2019). Study on the mechanism of CO_2 adsorption process on zeolite 5A as a molecular sieve in RDE system: An infrared investigation. Journal of Physics: Conference Series 1198: 032009.

Munawar, K., Mansoor, M.A., Olmstead, M.M., Zaharinie, T., Zubir, M.N.M., Haniffa, M., Basirun, W.J., & Mazhar, M. (2020). Fabrication of Ag-ZnO composite thin films for plasmonic enhanced water splitting. Materials Chemistry and Physics 255: 123220.

Pham, T.-H., Lee, B.-K., & Kim, J. (2016). Novel improvement of CO_2 adsorption capacity and selectivity by ethylenediamine-modified nano zeolite. Journal of the Taiwan Institute of Chemical Engineers 66: 239-248.

Qian, X., Ren, Q., Wu, X., Sun, J., Wu, H., & Lei, J. (2018). Enhanced water stability in Zn-doped zeolitic imidazolate framework-67 (ZIF-67) for CO_2 capture applications. Chemistry Select 3: 657.

Rajakrishnamoorthy, P., Saravanan, C.G., Natarajan, R., Karthikeyan, D., Sasikala, J., Josephin, J.S.F., Vikneswaran, M., Sonthalia, A., & Varuvel, E.G. (2023). Exhaust emission control of SI engines using ZSM-5 zeolite supported bimetals as a catalyst synthesized from coal fly ash. Fuel 340: 127380.

Sharma, K., Park, Y-K., Nadda, A.K., Banerjee, P., Singh, P., Raizada, P., Banat, F., Bharath, G., Jeong, S.M., & Lam, S.S. (2022). Emerging chemo-biocatalytic routes for valorization of major greenhouse gases (GHG) into industrial products: A comprehensive review. Journal of Industrial and Engineering Chemistry 109: 1-20.

Zhang, J., Huang, D., Shao, J., Zhang, X., Zhang, S., Yang, H., & Chen, H. (2023). A new nitrogen-enriched biochar modified by ZIF-8 grafting and annealing for enhancing CO_2 adsorption. Fuel Processing Technology 231: 107250.

DOI: https://doi.org/10.22452/mjs.vol43sp1.6
Malaysian Journal of Science 43 (Special Issue 1): 33-37 (July 2024)

MALAYSIAN JOURNAL OF SCIENCE
MJS
ISSN 1394 - 3065

2nd Euro-Asia Conference on CO_2 Capture and Utilization (EACCO2CU2022) Special issue

Malaysian Journal of Science 43 (Special Issue 1): 38-43 (July 2024) https://mjs.um.edu.my

MORINGA OLEIFERA (MO) SEED SHELL BASED ADSORBENT FOR POTENTIAL CO_2 CAPTURE: A CHARACTERIZATION STUDY

Amina Tahreen[1a], Mohammed Saedi Jami[2a*], Fathilah Ali[3a] and Zahangir Alam[4a]

Abstract: This study characterizes activated carbon synthesized from *Moringa oleifera (MO)* seed husk with a greener activating agent, namely sodium carbonate, (Na_2CO_3) compared to traditional activating agent, potassium hydroxide (KOH). Synthesized in a conventional tube furnace with nitrogen supply, the resulting activated carbon after cooling and washing, were characterized for Brunauer-Emmett-Teller (BET), Fourier-Transform Infrared Spectroscopy (FTIR), X-ray Diffraction (XRD) and Scanning Electron Microscope (SEM) analyses and compared with that produced with KOH activation. Although fewer and larger mesoporous activated carbon with smaller BET surface area (18.4659 m^2/g) were formed with Na_2CO_3 activation), compared to that of KOH activation (235.6034 m^2/g), this study highlights the ability and potential of the greener activating agent (Na_2CO_3) to utilize biomass waste and successfully produce activated carbon with minimum environmental hazards. The synthesized adsorbent can be explored for CO_2 capture applications in future studies.

Keywords: Adsorbent synthesis, Moringa oleifera (MO), greener activating agent.

1. INTRODUCTION

The growing concerns regarding greenhouse gas emissions on a global scale has prompted significant research and development efforts towards mitigating the effects through greener approaches. One prominent greenhouse gas is carbon dioxide (CO_2), which is largely generated through the combustion of fossil fuels. To combat the increasing CO_2 levels in the atmosphere, the development of effective and sustainable carbon capture technologies has become vital. Furthermore, as finite natural resources like fossil fuels diminish, and the combustion of coke generates CO_2 emissions, there is a demand for improved approaches to handle and utilize stockpiled coke. Converting biomass waste into activated carbon presents a resolution to address both waste management concerns and the necessity for CO_2 capture (Serafin et al., 2021). Activated carbon, with its exceptional adsorption properties, has emerged as a possible promising material for CO_2 capture (Abuelnoor et al., 2021; Varma, 2019). Its high surface area and pore structure provide ample opportunities for gas molecules, including CO_2, to be adsorbed, thereby, reducing their concentration in the atmosphere.

However, the conventional production methods of activated carbon often involve energy-intensive processes and the use of non-renewable resources, limiting their environmental viability. Hence, in this paper, a sustainable approach towards preparing a green activated carbon is proposed, focusing not only on the activation agent but also on the precursor material. *Moringa oleifera (MO),* a fast-growing tree found in tropical and subtropical regions, produces seeds, the husks of which are typically discarded as biomass waste. The use of *MO* seed husk as a raw material offers several environmental benefits (Yamaguchi et al., 2021). By repurposing this agricultural waste, the pressure on landfills and the need for conventional raw materials such as wood or coal, can be minimized. Additionally, *MO* seed husk (as shown in Figure 1) contains natural cellulose and lignin, which can serve as precursors for the carbonization process, ensuring the formation of a porous structure in the resulting activated carbon (González-García, 2018).

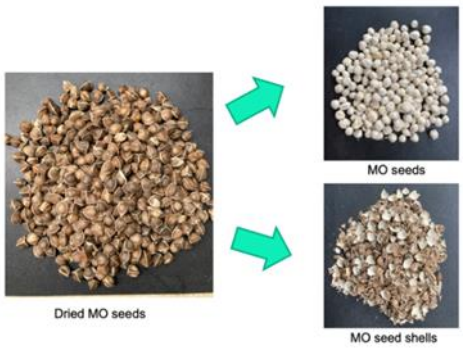

Figure 1. Dried *MO* seeds and separated husk.

However, the current strategies for producing activated carbons involve use of corrosive and hazardous chemical activating agents, typically potassium hydroxide (KOH) (Sevilla et al., 2021) and phosphoric acid (H_3PO_4) (Raji et al., 2023), limiting environmental safety in industrial applications. Hence, this study explores utilizing this sustainable precursor material with sodium carbonate (Na_2CO_3) as the green activation agent, which is a sodium based activating agent in terms of health hazard (Sevilla et al., 2021). The combination of a renewable precursor and an

Authors information:
[a]Department of Chemical Engineering and Sustainability, International Islamic University Malaysia, Kuala Lumpur, Malaysia. E-mail: aminatahreen@gmail.com[1], saedi@iium.edu.my[2], fathilah@iium.edu.my[3], zahangir@iium.edu.my[4]

*Corresponding Author: saedi@iium.edu.my

Received: February 7, 2024
Accepted: May 7, 2024
Published: July 31, 2024

DOI: https://doi.org/10.22452/mjs.vol43sp1.7
Malaysian Journal of Science 43 (Special Issue 1): 38-43 (July 2024)

eco-friendly activation aligns with the principles of sustainable development, fostering a circular economy approach while contributing towards the mitigation of climate change.

The objective of this study is to explore the potential of *MO* seed husk as a raw material for activated carbon synthesis, investigating its carbonization and activation characteristics with a Na_2CO_3. The results of this study will contribute to the ongoing efforts to develop environmentally friendly carbon capture technologies, incorporating sustainable raw materials into the production process. By utilizing *MO* seed husk, not only biomass waste can be reduced but also the sustainable utilization and transformation of biomass waste to wealth is promoted. This research has the potential to provide valuable insights into the feasibility of utilizing *MO* seed husk to produce activated carbon.

2. Method

Sun dried *MO* seeds were separated from their husks as shown in Figure 1. Next, the seed husk was grinded to powder form using a regular grinder. Following the approach of (Nedjai et al., 2021; Santos et al., 2020), *MO* seed powder was converted to activated carbon by chemical activation and thermal activation at 500 °C with a nitrogen flow of 0.2 L per minute in a lab scale furnace reactor. The pyrolysis time was 60 minutes (after the reactor reached the pyrolysis temperature) with a constant heating rate of 10 °C per minute. The reactor was heated with a custom heating mantle, and the temperature was checked with a type K thermocouple located inside the reactor. Before the pyrolysis process, chemical activation was performed on the ground *MO* seed shell powder (*MOSSP*), using KOH and Na_2CO_3 as activating agents with 1:1 impregnation ratio. The resulting chemically activated products are shown in Figure 2. The obtained carbon was dried in an oven at 105°C overnight. The mixture was then heated to the thermal activation temperature of 500˚C for 1 hour. The activated carbon produced after thermal activation is presented in Figure 3. After cooling, the resulting products underwent a thorough rinsing process using a 0.1 M HCl solution and warm distilled water until the pH reached 7.0. This rinsing procedure was employed to eliminate any residual activating agents and other inorganic substances that may have formed during the process. During the washing phase, the activated carbon was separated using Whatman filter paper. Subsequently, the obtained carbon was subjected to drying at 105°C until it achieved complete dryness, after which it was securely stored in tightly sealed centrifuge bottles for subsequent analysis. They

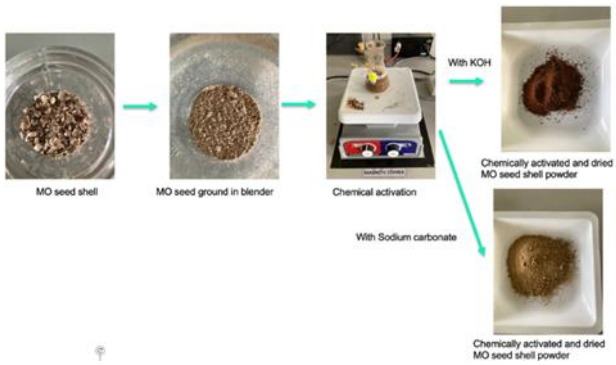

Figure 2. Summary of chemical activation process.

were analyzed for Brunauer-Emmett-Teller (BET), Fourier-Transform Infrared Spectroscopy (FTIR), X-ray Diffraction (XRD) and Scanning Electron Microscope (SEM) analyses.

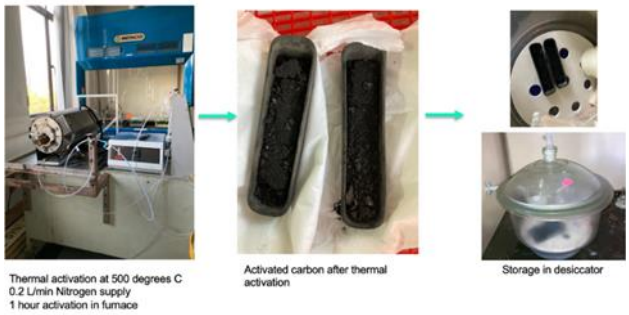

Figure 3. Thermal activation in furnace.

3. Results and discussion

This section discusses the resulting activated carbon properties in terms of SEM, FTIR, XRD and BET analyses.

3.1 SEM Analysis

The *MO* seed shell powder (*MOSSP*) was viewed under SEM, as shown in Figure 4 at x2000 magnification. Although most surfaces showed flat sheet type surfaces, some porous surfaces were observed as well. Having few porous structures before any chemical or thermal activation suggests potential inherent adsorptive ability of the seed husk powder. The SEM image depicts the morphology of the *MOSSP* in its natural form without any activation. Similar observation was made by Khalfaoui et al. (2022).

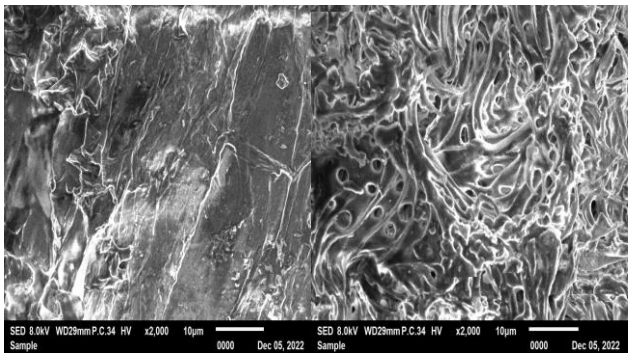

Figure 4. SEM images of raw *MO* seed shell powder at magnification x2000.

However, after chemical and thermal activation, more distinct porous structures were observed for both KOH and Na_2CO_3 based activation, as seen in Figures 5 and 6. *MOSSP* activated with Na_2CO_3 showed a pattern of mesopores inside circular fibrous structures (lignin), more prominently observed in x2000 magnification. This structure can potentially provide a good surface area for CO_2 adsorption, through the pores in the network of circular structures. By modifying the precursor surface, Nguyen et al. (2016) was able to produce mesoporous carbon with high CO_2 uptake with the largest mesoporous areas of the adsorbent.

DOI: https://doi.org/10.22452/mjs.vol43sp1.7
Malaysian Journal of Science 43 (Special Issue 1): 38-43 (July 2024)

With KOH activation, no fibrous structures were noted in the activated carbon, which is an indicator that KOH activation is strong enough to create smaller pores with higher density, while disintegrating all lignin from the *MOSSP*. The mild activating intensity of Na_2CO_3 resulted in the incomplete disintegration of the fibrous structures and hence, were still visible after activation at x1000 magnification (shown in Figure 5). The pores were further zoomed in with x2000 magnification in Figure 6. Notably, KOH activation produced smaller porous structures compared to Na_2CO_3 activation. KOH was able to produce smaller mesopores with higher BET surface area and pore volume in *MOSSP* compared to Na_2CO_3. The difference in mesopore development between KOH and Na_2CO_3 as activating agents for producing activated carbon can be attributed to their distinct activation mechanisms and chemical properties. KOH, being a strong activating agent, tends to promote more extensive and aggressive gasification and pore formation during activation (Sevilla et al., 2021). Its high reactivity leads to the creation of a larger number of mesopores within the activated carbon structure. In contrast, Na_2CO_3, while still effective, exhibits a more moderate activation strength, resulting in the formation of fewer but larger mesopores.

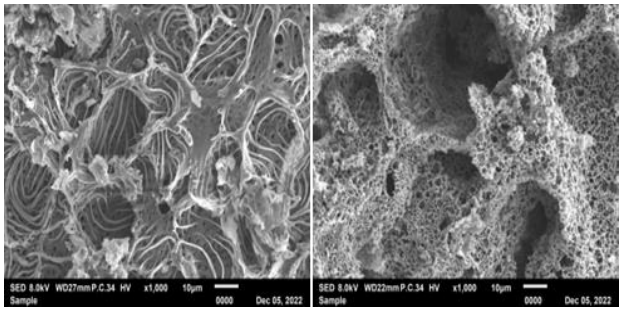

Figure 5. SEM image of *MO* seed shell synthesized with Na_2CO_3 (left) and KOH (right) activation at x1000 magnification.

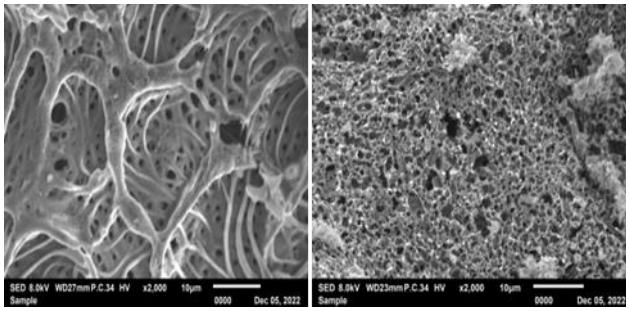

Figure 6. SEM image of *MO* seed shell synthesized with Na_2CO_3 (left) and KOH (right) activation at x2000 magnification.

3.2 XRD Analysis

X-ray diffraction (XRD) is vital for characterizing the prepared activated carbons, to identify their crystalline phases, detect impurities, and indirectly provide insights into pore structure that influences its adsorption capacity. It can spot defects in the material, quantify crystalline phases, reveal structural parameters, and guide process optimization and material development for various applications. Figure 7 depicts the X-ray diffractogram of *MOSSP* before (green) and after activation with KOH (red) and Na_2CO_3 (blue) activation. The broad peak (2θ) at 23° depicts the amorphous structure of the *MOSSP* and produced activated carbon (Prakash et al., 2020), which slightly shifted to 25° after conversion to activated carbon using both KOH and Na_2CO_3 activating agents. The peak shift observed in the XRD pattern of *MOSSP* after chemical and thermal activation are reflective of the changes occurring in the material's structure and composition. These changes are responsible for the development of a porous and highly adsorptive activated carbon material, making it suitable for various applications such as water treatment and CO_2 adsorption. Besides peak shift, there was an elevation of peak intensities after activated carbon production. Activation created a vast network of micro and mesopores within the activated carbon material. These pores provide additional scattering centres for X-rays, contributing to the increased intensity of the XRD peaks. The abundance of pores enhanced the diffraction efficiency of the activated carbon sample. However, a sharp peak at 27° for KOH activated carbon and 68.5° for Na_2CO_3 denotes the presence of possible impurities in the final activated carbon.

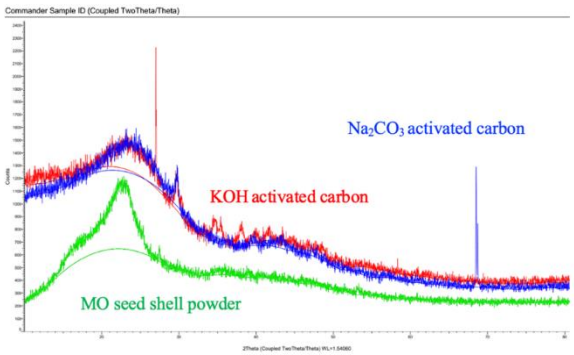

Figure 7. XRD graphs of *MOSSP* (green), *MO* activated carbon with KOH (red) and Na_2CO_3 (blue).

The sharp peaks in the XRD diffractogram of activated carbon can happen due to the presence of well-ordered crystalline regions within the material. During the activation process, certain conditions or precursor materials may lead to the development of these crystalline carbon regions. This occurs through processes like graphitization, where carbon atoms are arranged in repeating graphene layers, forming small crystallites (Zhang et al., 2022). Additionally, the presence of impurities or inorganic materials introduced during the activation process can also contribute to the appearance of sharp diffraction peaks. Overall, the sharp peaks were indicative of the structural complexity of the activated carbon, with crystalline regions providing additional adsorption sites and impurities potentially influencing its adsorption behaviour. Understanding the reasons for the sharp peaks helps in characterizing and optimizing activated carbon for various applications.

3.3 FTIR Analysis

FTIR analysis was conducted to characterize the prepared activated carbons by detecting surface functional groups and chemical bonds, evaluating composition and purity, and investigating the impact of surface modifications. Figure 8 shows the FTIR spectra of *MOSSP* alongside of KOH and Na_2CO_3-AC activated carbons. Overall, the *MOSSP* spectrum exhibited more

DOI: https://doi.org/10.22452/mjs.vol43sp1.7
Malaysian Journal of Science 43 (Special Issue 1): 38-43 (July 2024)

absorption peaks compared to the KOH-AC and Na_2CO_3-AC spectra. Upon activation, several peaks present in the *MOSSP* disappeared in the activated carbon spectra, indicating structural changes resulting from the activation process. This was due to the elimination of heat-sensitive functional groups at high temperatures and volatiles (Nedjai et al., 2021).

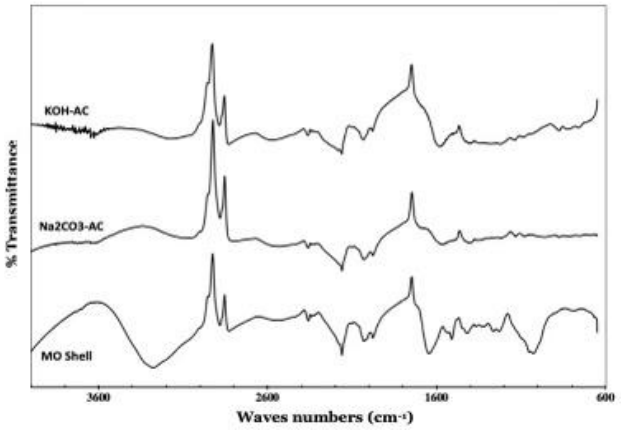

Figure 8. Fourier Transform Infra-Red Spectra for *MO* shell and KOH and Na_2CO_3 activated carbons.

For the *MOSSP* (not activated), the broad band at 3278 cm^{-1} is a characteristic of a stretching vibration of hydrogen-bonded (O-H) hydroxyl groups. The peaks appearing at 2881 and 2828 cm^{-1} are described to (C–H) symmetric stretching and ($–CH_2$) alkyl groups. The bands observed at 2160 cm^{-1} and 2029 cm^{-1} were due to the presence of (C≡N) stretching (Prahas et al., 2008; Vunain & Biswick, 2019). Another peak noted at 2358 cm^{-1} is related to the (C≡N) stretching vibration. The band at around 1644 cm^{-1} is the (C=O) stretching vibration due to the bonds of esters and phenols (Jawad & Abdulhameed, 2020), which disappeared in KOH-AC and Na_2CO_3-AC. The peak observed at 1509 cm^{-1} corresponds to the secondary amine group. Other bands, recorded at 1422 cm^{-1} and 1229 cm^{-1} are attributed to CH_3 asymmetric bending and C-O stretching, respectively. A peak situated at around 1027 cm^{-1} depicted the characteristics of anhydrides (C–O), which also disappeared completely after the chemical activation.

For Na_2CO_3-AC, the FTIR spectroscopic analysis indicated the presence of different peaks at 3055 cm^{-1}, 2881 cm^{-1}, 2529 cm^{-1}, 1556 cm^{-1}, 1408 cm^{-1} which were the characteristics of O–H (hydroxyls), C–H (alkyls), C≡C (alkyne), C–O–C (ester, ether and phenol) and CH_3 asymmetric bending, respectively. On the other hand, the FTIR spectrum of KOH-AC depicted broad weak peaks around 3897–3564 cm^{-1} and other peaks around 3175 cm^{-1}, 2885 cm^{-1}, 2574 cm^{-1}, 1574 cm^{-1}, 1225 cm^{-1}, and 847 cm^{-1}. These are the characteristics of O–H (hydroxyls), C–H (alkyls), C≡C (alkyne), C–O–C (ester, ether and phenol), C-O stretching, and C-H bending, respectively. The main functional groups in prepared activated carbons were, therefore, hydroxyl groups, carbonyl groups, and carboxyl groups, which indicated that the functional groups have been successfully stepped onto the surface of the activated carbons and contain binding sites of various natures.

3.4 BET Analysis

BET analysis was carried out on the prepared activated carbons to quantify their surface area and pore structure, to provide insights into the activated carbon's adsorption capabilities. Table 1 presents the results of the BET analysis for the three samples: KOH-AC, Na_2CO_3-AC, and *MOSSP* (no activation). It is evident that pore size plays a significant role in determining the CO_2 capture ability of Na_2CO_3-AC. While KOH-AC exhibited a smaller average pore diameter (5.8482 nm) and a higher BET surface area, Na_2CO_3-AC demonstrated larger average pore diameter (14.8646 nm). This difference in pore size indicated that Na_2CO_3-AC was characterized by larger mesopores and macropores, which are advantageous for capturing CO_2 molecules. These larger pores provide sufficient space and accessibility for CO_2 adsorption, enabling Na_2CO_3-AC to effectively capture and store CO_2. Although Na_2CO_3-AC has a lower BET surface area (18.4659 m^2/g) compared to KOH-AC (235.6034 m^2/g), its ability to accommodate CO_2 within its larger pores can potentially compensate for the surface area difference. Hence, the pore size distribution of Na_2CO_3-AC may contribute to its CO_2 capture ability, showcasing the importance of pore structure in determining the performance of green activated carbon materials.

Table 1. Summary of BET analysis results.

Sample	S_{BET}[a]	D_{Pore}[b]	V_t[c]
KOH-AC	235.6034 m^2/g	5.8482 nm	0.163380 cm^3/g
Na_2CO_3-AC	18.4659 m^2/g	14.8646 nm	0.041413 cm^3/g
MOSSP	0.9332 m^2/g	23.9764 nm	0.001688 cm^3/g

[a] BET surface Area
[b] Adsorption average pore diameter
[c] Single point adsorption total pore volume of pores

DOI: https://doi.org/10.22452/mjs.vol43sp1.7
Malaysian Journal of Science 43 (Special Issue 1): 38-43 (July 2024)

Mesopores, with pore sizes ranging from 2 to 50 nm, contribute to the effectiveness of CO_2 capture in activated carbons. While micropores play a dominant role in providing high surface area and strong interaction with CO_2 molecules, mesopores offer additional advantages. Their presence facilitates improved mass transfer and faster diffusion of CO_2 within the material. By providing larger pathways, mesopores can enhance the accessibility of CO_2 to the adsorption sites, leading to potentially more efficient adsorption. The reduced diffusion resistance within mesoporous structures enables a higher flow rate of CO_2, resulting in enhanced kinetics of the capture process (Azmi & Aziz, 2019).

4. Conclusion

In the context of CO_2 capture, it is important to note that pore size alone is not the sole determinant of the CO_2 capture ability of Na_2CO_3-AC. While pore size can influence the accessibility and diffusion of CO_2 molecules within the material, other factors such as surface chemistry, surface area, and pore volume also play crucial roles in determining the CO_2 adsorption capacity. Therefore, it is necessary to consider a comprehensive analysis of all these parameters to assess the CO_2 capture ability of Na_2CO_3-AC accurately. The choice between these agents depends on the desired pore structure and specific application requirements, with KOH offering greater mesopore development when it is needed for applications like gas adsorption and catalysis. Additionally, mesopores can be modified or coated to increase surface coverage and affinity for CO_2 adsorption.

Although, KOH based activated carbon in this study seemed to be a more favorable adsorbent material for CO_2 capture, employing Na_2CO_3 to produce the activated carbon from biomass waste such as *MO* seed husk, provided an insight on a greener adsorbent production strategy, that can be further explored.

5. Acknowledgement

The authors express gratitude to International Islamic University Malaysia, Faculty of Engineering, for the financial support under Tuition Fee Waiver (TFW) 2021 scheme. The authors also thank the Ministry of Education (MOE) Malaysia for granting a Fundamental Research Grant Scheme (FRGS), project no. FRGS/1/2019/TK02/UIAM/01/1 to support this work.

6. References

Abuelnoor N., AlHajaj, A., Khaleel M., Vega L. F. & Abu-Zahra M R M. (2021). Activated carbons from biomass-based sources for CO_2 capture applications. Chemosphere, 282(March), 131111, https://doi.org/10.1016/j.chemosphere.2021.131111.

Azmi A. A. & Aziz M. A. A. (2019). Mesoporous adsorbent for CO2 capture application under mild condition: A review. Journal of Environmental Chemical Engineering, 7(2), 103022, https://doi.org/10.1016/j.jece.2019.103022.

González-García P. (2018). Activated carbon from lignocellulosics precursors: A review of the synthesis methods, characterization techniques and applications. Renewable and Sustainable Energy Reviews, 82(August 2017), 1393–1414, https://doi.org/10.1016/j.rser.2017.04.117.

Jawad A. H. & Abdulhameed A. S. (2020). Statistical modeling of methylene blue dye adsorption by high surface area mesoporous activated carbon from bamboo chip using KOH-assisted thermal activation. Energy, Ecology and Environment, 5(6), 456–469, https://doi.org/10.1007/s40974-020-00177-z.

Khalfaoui A., Mahfouf E., Derbal K., Boukhaloua S., Chahbouni B. & Bouchareb R. (2022). Uptake of Methyl Red dye from aqueous solution using activated carbons prepared from Moringa Oleifera shells. 4(September), https://doi.org/10.1016/j.clce.2022.100069.

Nedjai R., Alkhatib M. F. R., Alam M. Z. & Kabbashi N. A. (2021). Adsorption Of Methylene Blue Onto Activated Carbon Developed From Baobab Fruit Shell By Chemical Activation: Kinetic Equilibrium Studies. IIUM Engineering Journal, 22(2), 31–49, https://doi.org/10.31436/iiumej.v22i2.1682.

Nguyen T. H., Kim S., Yoon M. & Bae T. H. (2016). Hierarchical Zeolites with Amine-Functionalized Mesoporous Domains for Carbon Dioxide Capture. ChemSusChem, 9(5), 455–461, https://doi.org/10.1002/cssc.201600004.

Prakash M. O., Raghavendra G., Ojha S. & Panchal M. (2020). Characterization of porous activated carbon prepared from arhar stalks by single step chemical activation method. Materials Today: Proceedings, 39(xxxx), 1476–1481, https://doi.org/10.1016/j.matpr.2020.05.370.

Prahas D., Kartika Y., Indraswati N. & Ismadji S. (2008). Activated carbon from jackfruit peel waste by H3PO4 chemical activation: Pore structure and surface chemistry characterization. Chemical Engineering Journal, 140(1–3), 32–42, https://doi.org/10.1016/j.cej.2007.08.032.

Raji Y., Nadi A., Mechnou I., Saadouni M., Cherkaoui O. & Zyade S. (2023). High adsorption capacities of crystal violet dye by low-cost activated carbon prepared from Moroccan Moringa oleifera wastes: Characterization, adsorption and mechanism study. Diamond and Related Materials, 135(February), 109834, https://doi.org/10.1016/j.diamond.2023.109834.

Santos T. M., de Jesus F. A., da Silva G. F. & Pontes L. A. M. (2020). Synthesis of activated carbon from oleifera moringa for removal of oils and greases from the produced water. Environmental Nanotechnology, Monitoring and Management, 14(August), https://doi.org/10.1016/j.enmm.2020.100357.

Serafin J., Ouzzine M., Cruz O. F., Sreńscek-Nazzal J., Campello Gómez I., Azar F. Z., Rey Mafull C. A., Hotza D. & Rambo C. R. (2021). Conversion of fruit waste-derived biomass to highly microporous activated carbon for enhanced CO_2 capture. Waste Management, 136(October), 273–282, https://doi.org/10.1016/j.wasman.2021.10.025.

DOI: https://doi.org/10.22452/mjs.vol43sp1.7
Malaysian Journal of Science 43 (Special Issue 1): 38-43 (July 2024)

Sevilla M., Díez N. & Fuertes A. B. (2021). More Sustainable Chemical Activation Strategies for the Production of Porous Carbons. ChemSusChem, 14(1), 94–117, https://doi.org/10.1002/cssc.202001838.

Yamaguchi N. U., Cusioli L. F., Quesada H. B., Camargo Ferreira M. E., Fagundes-Klen M. R., Salcedo Vieira A. M., Gomes R. G., Vieira M. F. & Bergamasco R. (2021). A review of Moringa oleifera seeds in water treatment: Trends and future challenges. Process Safety and Environmental Protection, 147(September), 405–420, https://doi.org/10.1016/j.psep.2020.09.044.

Varma R. S. (2019). Biomass-Derived Renewable Carbonaceous Materials for Sustainable Chemical and Environmental Applications. ACS Sustainable Chemistry and Engineering, 7(7), 6458–6470, https://doi.org/10.1021/acssuschemeng.8b06550.

Vunain E. & Biswick T. (2019). Adsorptive removal of methylene blue from aqueous solution on activated carbon prepared from Malawian baobab fruit shell wastes: Equilibrium, kinetics and thermodynamic studies. Separation Science and Technology (Philadelphia), 54(1), 27–41, https://doi.org/10.1080/01496395.2018.1504794.

Zhang S., Zheng M., Tang Y., Zang R., Zhang X., Huang X., Chen Y., Yamauchi Y., Kaskel S. & Pang H. (2022). Understanding Synthesis–Structure–Performance Correlations of Nanoarchitectured Activated Carbons for Electrochemical Applications and Carbon Capture. Advanced Functional Materials, 32, https://doi.org/10.1002/adfm.202204714.

DOI: https://doi.org/10.22452/mjs.vol43sp1.7
Malaysian Journal of Science 43 (Special Issue 1): 38-43 (July 2024)

MALAYSIAN JOURNAL OF SCIENCE
MJS
ISSN 1394 - 3065

2nd Euro-Asia Conference on CO_2 Capture and Utilization (EACCO2CU2022) Special issue

Malaysian Journal of Science 43 (Special Issue 1): 44-49 (July 2024) https://mjs.um.edu.my

PERFORMANCE EVALUATION OF HYDROXYAPATITE PREPARED FROM EGGSHELLS IN CARBON DIOXIDE ADSORPTION

Kah Man Su[1a], Kiat Moon Lee[2a,b*], Farihahusnah Hussin[3c], Mohamed Kheireddine Aroua[4c]

Abstract: Eggshell waste is typically produced from daily poultry consumption and industrial applications. They are a rich source of calcium in the form of carbonates and oxides, recognised as excellent hydroxyapatite sources (HAp). To date, limited studies have highlighted the modification of HAp with impregnation. In the present study, HAp was prepared via the precipitation method, and further modification of HAp using monoethanolamine (MEA) and deep eutectic solvent, particularly choline chloride:urea (ChCl:U), were explored for carbon dioxide (CO_2) capture. The morphological structures were studied using a scanning electron microscope, while properties were assessed using energy-dispersive X-ray spectroscopy techniques (SEM-EDX) and Brunauer-Emmett-Teller (BET). The CO_2 adsorption performance using raw and impregnated HAp was also evaluated. By introducing the chemisorption process, the impregnated ChCl:U-HAp with irregular crystallite agglomerates demonstrated a higher adsorption capacity and longer breakthrough time than raw HAp and MEA-HAp. This study confirms the feasibility of using eggshells to produce HAp as an effective adsorbent in CO_2 capture.

Keywords: Hydroxyapatite, eggshell, carbon dioxide adsorption, impregnation, deep eutectic solvent

1. Introduction

In the era of industrialisation, the combustion of fossil fuels is the major culprit of environmental issues like climate change and global warming. In compliance with the Kyoto Protocol and the Paris Agreement, the scientific community has proposed several techniques in carbon capture, utilisation and storage (CCUS) to combat global warming. Some CCUS techniques, such as chemical absorption, membrane separation and cryogenic processes, have been widely implemented to minimise carbon dioxide (CO_2) emissions (Zhao et al., 2018). Chemical absorption using amines is commonly used in industries due to high CO_2 capture efficiency. However, it encounters high energy consumption during regeneration and experiences solvent degradation problems (Azmi & Aziz, 2019). Therefore, adsorption using porous carbonaceous materials is more attractive, with the advantages of low-cost synthesis and high thermal and chemical stability. To achieve satisfaction in aspects of operational and economical, novel adsorbents have been produced from low-cost natural wastes such as tea (Rattanaphan et al., 2020), municipal solid waste (Karimi et al., 2020), walnut shell (Khoshraftar & Ghaemi, 2022) and other biomass sources (P. H. Ho et al., 2021).

The yearly generation of about 250,000 tons of eggshells from daily use results in landfill disposal without further processing, leading to other environmental issues, such as disgusting smell and infection propagation risk (Mignardi et al., 2020). Hence, reusing and converting eggshell wastes into useful materials for sustainable development is vital. In recent years, eggshell wastes have been utilised as a low-cost adsorbent due to their porous structure. Several researchers highlighted that eggshells have a high specific surface area that aids in heavy metal removal (Abatan et al., 2020; Latiff et al., 2022; Tizo et al., 2018). Considering the calcium levels in eggshells, they could serve as a potential source for synthesising hydroxyapatite (HAp) . HAp is an organic mineral with a typical $Ca_{10}(PO_4)_6(OH)_2$ lattice structure. Due to its calcium and phosphate content (the main mineral component of bones and teeth), it offers several applications, including bone repair and tissue regeneration (Tangboriboon et al., 2019). HAp is also gaining significant attention in developing novel adsorbents due to their favourable properties, such as high adsorptive, thermal and chemical stability (J.-Y. Ho et al., 2024).

A deep eutectic solvent (DES) is a eutectic mixture with two or three components capable of self-dissociating to form a eutectic solvent of a lower melting point than their individual (Chia et al., 2023). DES is formed by a hydrogen-bond donor and a hydrogen-bond acceptor components via hydrogen bonds. DES is widely recognised as a green solvent as it offers several advantages, such as low toxicity, low volatility, low flammability, high solubility capacity, high thermal stability, and biodegradable properties (Babaei & Haghtalab, 2023; Massayev & Lee, 2022). Recently, many efforts have been made to develop DES for CO_2 capture. Trivedi et al. (2016) synthesised monoethanolamine hydrochloride-ethylenediamine DES for CO_2 capture. The DES

Authors information:
[a] Department of Chemical & Petroleum Engineering, UCSI University, Kuala Lumpur 56000, Malaysia. Email: 1001438119@ucsiuniversity.edu.my[1], leekm@ucsiuniversity.edu.my[2]
[b]UCSI-Cheras Low Carbon Innovation Hub Research Consortium, Kuala Lumpur, Malaysia. Email: leekm@ucsiuniversity.edu.my[2]
[c]Research Centre for Carbon Dioxide Capture and Utilization (CCDCU), School of Engineering and Technology, Sunway University, Selangor, Malaysia. Email: farihah@sunway.edu.my[3], kheireddinea@sunway.edu.my[4]

*Corresponding author: leekm@ucsiuniversity.edu.my[2]

Received: February 7, 2024
Accepted: May 7, 2024
Published: July 31, 2024

DOI: https://doi.org/10.22452/mjs.vol43sp1.8
Malaysian Journal of Science 43 (Special Issue 1): 44-49 (July 2024)

could interact with CO_2 gas to form carbamate. An adsorption capacity of 0.54 mol CO_2/mol solvent was reported for the system.

Nevertheless, little scientific research on CO_2 adsorption using DES-impregnated HAp is available. Therefore, this work would explore eggshell-based HAp to be impregnated with DES (particularly choline chloride:urea, ChCl:U) as a bioadsorbent for CO_2 capture. A comparison study was also included by impregnating the HAp with monoethanolamine (MEA), a common solvent used for CO_2 capture. The results of CO_2 adsorption performance were supported by scanning electron microscopy with energy dispersive X-ray spectroscopy (SEM-EDX) and Brunauer-Emmett-Teller (BET) analyses.

2. Methodology

2.1 Materials

All chemicals and reagents were in analytical grade and used without further purification. Phosphoric acid (H_3PO_4, 85%) and urea (CH_4N_2O, 99%) were purchased from Anhui Fulltime. Nitric acid (HNO_3, 69%) and ammonium hydroxide (NH_4OH, 25%) were supplied by R&M Chemicals. Ethanolamine (C_2H_7NO, 99%) and choline chloride ($C_5H_{14}ClNO$, 99%) were purchased from Thermo Fisher Scientific; meanwhile, ethanol (C_2H_5OH, 95%) was from HMBG.

2.2 Pretreatment of Eggshells

All the collected eggshells were cleaned with water to remove impurities, followed by 30 min of boiling and removing their inner white membrane. The eggshells were sent into an oven (AX30, Carbolite, UK) for drying overnight. Dried eggshells were ground into fine powder using an agate mortar and passed through a 10 mesh sieve, followed by calcination in a furnace (DAIHAN FHX-14, Daihan Scientific, Korea) at a temperature of 900℃ for 4 h.

2.3 Synthesis of Hydroxyapatite (HAp)

Pretreated eggshells were reacted with HNO_3 (69%) at a weight ratio 10:6 under constant stirring. Titration was done by adding 50 ml of 0.6 M H_3PO_4 solution into the mixture. The pH of the mixture was maintained at 10 using NH_4OH solution. The mixture was put aside for precipitation, and the resultant precipitate was filtered and washed using distilled water and ethanol. The washed sample was sent for overnight drying, followed by calcination at 900℃ for 1 h to form HAp powder.

2.3 HAp impregnation with MEA and DES

HAp was impregnated with MEA according to the procedure introduced by Khalil (2018). 2 g of MEA was stirred with 5 g of HAp for 1 h, and deionised water was added as an environmentally friendly medium to facilitate the impregnation process. The slurry was filtered and dried in the oven at 70°C for 6 h to form MEA-HAp. Choline chloride and urea were mixed in a molar ratio of 1:2 at 80℃ with constant mixing until homogenous. The homogenous solution developed is known as DES. Impregnation of HAp with DES was fixed at a weight ratio of 1. 5 ml ethanol was added to HAp and DES, followed by 2 h stirring to ensure complete impregnation. The mixture was kept overnight and dried at 80℃ for 6 h, forming DES-HAp.

2.4 Characterisation Studies and Adsorption Test

The HAp samples were sent for scanning electron microscopy (SEM) characterisation (Vega3, TESCAN, Czech Republic) to study the surface morphology of the synthesised bioadsorbents. Energy dispersive X-ray spectroscopy (EDX) (EDX-Oxford, TESCAN, UK) were incorporated to analyse the elemental composition of the adsorbents. The Bunauer-Emmett-Teller (BET) method was used to study samples' specific surface area using Micromeritics Tristar II Plus, USA.

The CO_2 adsorption study was conducted using a packed bed column to determine the adsorbent's performance in CO_2 capture. Breakthrough curve and maximum CO_2 adsorption capacity were determined. Initially, 30 g of the bioadsorbent was transferred into the packed bed column. The column was purged with N_2 gas for 10 min at room temperature and atmospheric pressure to create an inert environment. The adsorption study was conducted by introducing a mixture of N_2 and CO_2 gases into the packed bed column, in which the CO_2 composition was maintained at 15% under a constant flow rate of 200 ml/min using a digital mass flow controller. A CO_2 analyser (Alpha Omega series 9610) was connected to the column outlet to analyse the CO_2 concentration. The results were collected and recorded using a data logger system (GRAPHTEC GL820).

3. Results and discussion

3.1 SEM Characterisation

SEM was used to identify the surface morphology of HAp samples. Figure 1 shows the SEM images of raw HAp, MEA-HAp and DES-HAp under the magnification of 3000×. Raw HAp shows smooth flakes of porous surface (Figure 1(a)). The observed morphology could be effective in CO_2 adsorption. Unigul and Nigiz (2020a) reported that activated carbon exhibited a smooth and porous structure that demonstrated a higher CO_2 adsorption than other samples. Therefore, the similarity of HAp morphology to that of activated carbon could suggest the effectiveness of the HAp in CO_2 adsorption. Impregnation was introduced to modify the surface properties of the HAp for enhanced CO_2 adsorption capacity. With impregnation, an irregular cloud-like shape and more visible pores were observed in MEA-HAp (Figure 1(b)), and irregular clouds with distinct pores were observed in DES-HAp (Figure 1(c)). The distinct pores could provide more active sites for CO_2 adsorption, as Makoś and his co-authors (2020) suggested.

3.2 EDX Characterisation

EDX analysis was performed to identify the elemental composition of the HAp samples. Table 1 summarises the elemental composition of carbon (C), oxygen (O), calcium (Ca), phosphorus (P), nitrogen (N) and chlorine (Cl) in each sample. Figure 2(a) reveals that the typical elements of C, O, Ca and P were found in the raw HAp. The presence of C evinced the synchronised process. Heat supply during the calcination process initiated the

DOI: https://doi.org/10.22452/mjs.vol43sp1.8
Malaysian Journal of Science 43 (Special Issue 1): 44-49 (July 2024)

t

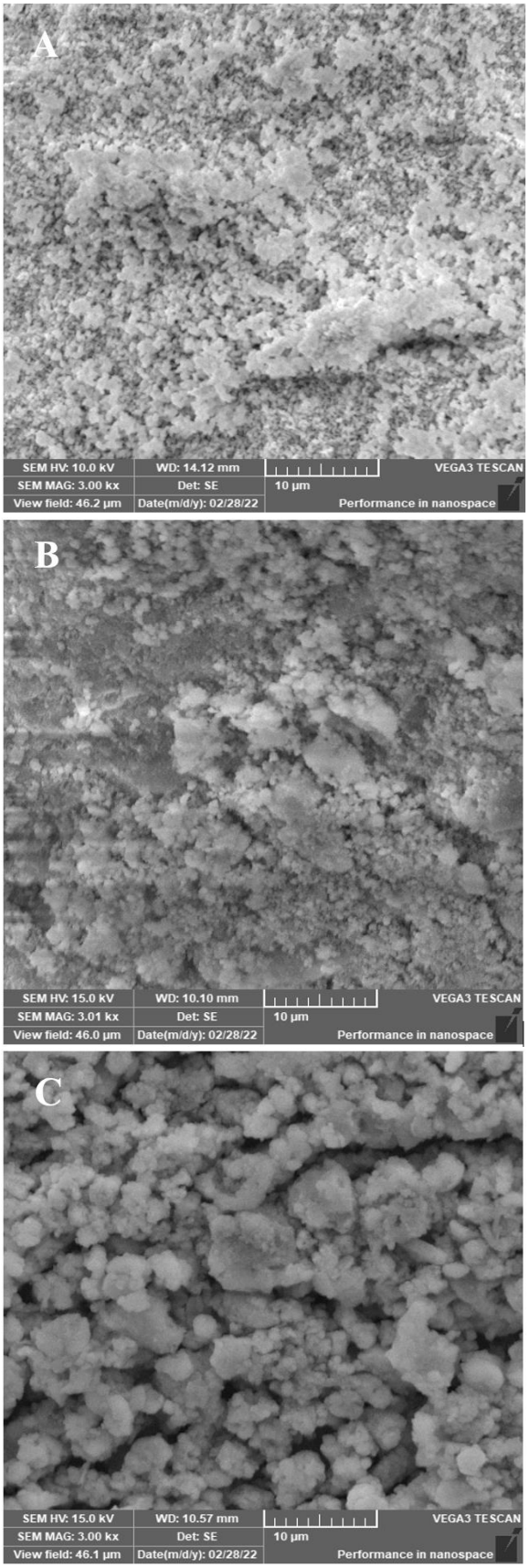

Figure 1. SEM image of (A) raw HAp, (B) MEA-HAp and (C) DES-HAp.

Table 1. Elemental composition of raw HAp, MEA-HAp, DES-HAp

Element	Weight (%)		
	Raw HAp	MEA-HAp	DES-HAp
C	7.04	10.35	21.19
O	58.34	44.43	36.13
Ca	21.09	24.75	20.87
P	13.53	12.74	11.08
N	-	5.77	9.49
Cl	-	1.96	1.23

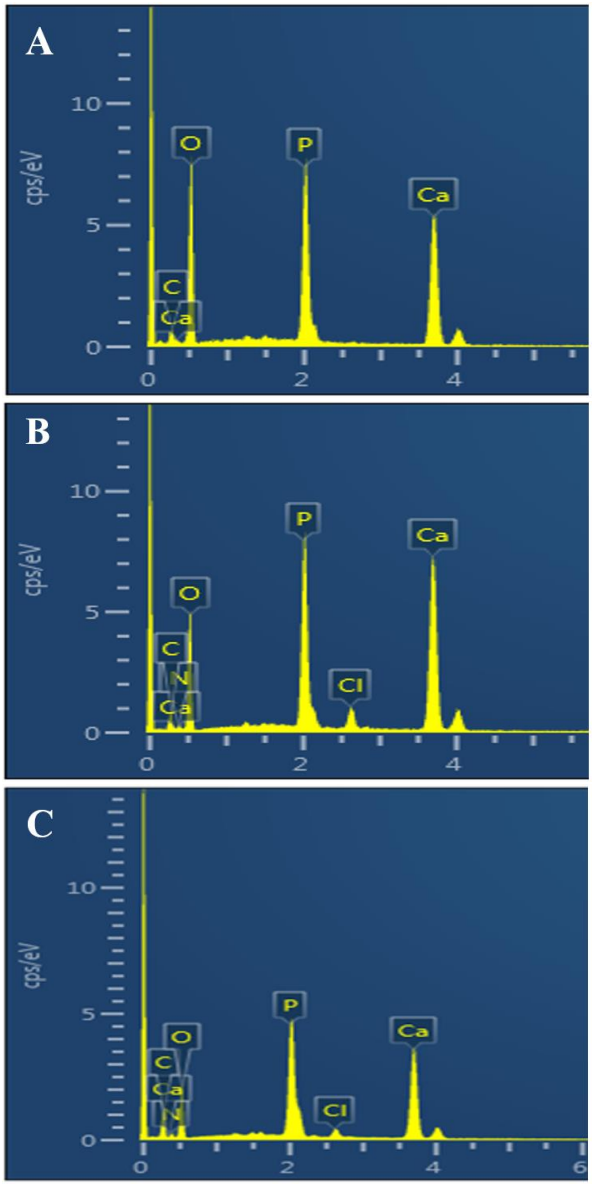

Figure 2. EDX spectra of (A) raw HAp, (B) MEA-HAp and (C) DES-HAp.

DOI: https://doi.org/10.22452/mjs.vol43sp1.8
Malaysian Journal of Science 43 (Special Issue 1): 44-49 (July 2024)

volatile matter from the eggshells. Subsequently, it produced a stable carbon element in the raw HAp (Agbabiaka et al., 2020). The element P was detected due to the addition of phosphoric acid during the titration process in the HAp synthesis reaction (Ariyanto et al., 2021). Additional elements of N and Cl were detected in MEA-HAp and DES-HAp samples (as shown in Figures 2(b) and 2(c))due to the impregnation solvents of MEA and ChCl:U, respectively. The presence of N provided more active sites for CO_2 adsorption. The features stem from the inherent qualities of the N element, allowing it to bind effectively with CO_2 based on its acidity.

3.3 BET Characterisation

Table 2 presents the BET surface area and pore characteristics of the raw HAP, MEA-HAp and DES-HAp. Raw HAp possessed a low specific surface area of 5.71 m^2/g. The result is aligned with the morphology structure discussed earlier in Section 3.1. As shown in Table 2, the specific surface area of MEA-HAp increased significantly from 5.71 m^2/g to 105.84 m^2/g. This sharp change shows that MEA impregnation enhanced the formation of a porous structure, directly increasing the BET surface area. This observation was also synchronised with the morphology study in Section 3.1, whereby more visible pores were observed in MEA-HAp compared to raw HAp. Nevertheless, the total surface area and pore volume of HAp impregnated with ChCl:U were lower than raw HAp. The total surface area and pore volume reduction in the DES-HAp sample were caused by pores blockage of HAp with DES solvent during the impregnation process (Ghazali et al., 2020).

Table 2. BET surface area and pore characteristics of raw HAp, MEA-HAp and DES-HAp

	RAW HAp	MEA-HAp	DES-HAp
BET(m^2/g)	5.7058	105.8397	5.4287
Langmuir(m^2/g)	26.1995	423.8743	18.6011
Average pore diameter (nm)	0.92873	0.81247	0.71154

3.4 CO_2 Adsorption

The CO_2 adsorption performances were recorded at 273 K and 1 atm, and the results were presented in Figure 3 and Table 3. All samples followed a similar adsorption trend. The CO_2 uptake of all samples increased with contact time and occupied all available adsorption sites until a final equilibrium was obtained. However, each adsorbent had a different time spent to reach saturation. Raw HAp demonstrated an adsorption capacity of 5.14 mg/g at 3.05 mins breakthrough time. As presented in the SEM morphology study in Section 3.1, raw HAp possessed a large pore diameter, which is advantageous for CO_2 to diffuse and adsorb into the adsorbent. However, the low adsorption capacity of raw HAp was mainly attributed to its lowest specific surface area, as discussed in BET analysis, which limited the amount of CO_2 adsorbed on the adsorbent.

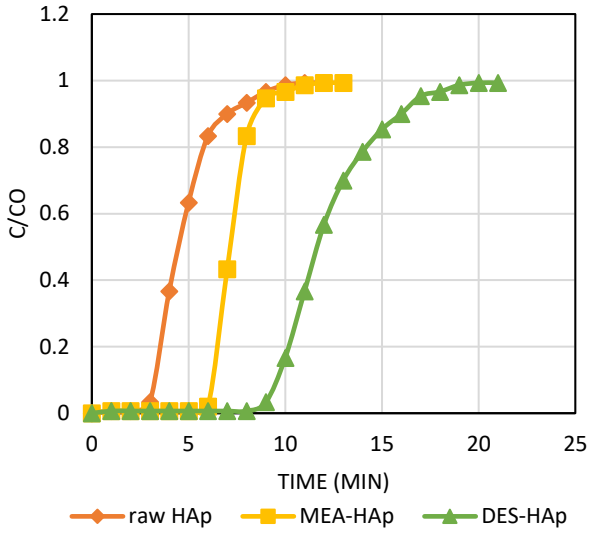

Figure 3. Adsorption breakthrough curves of raw HAp, MEA-HAp and DES-HAp.

Table 3. Breakthrough time and adsorption capacity of raw HAp, MEA-HAP, DES-HAp

	RAW HAp	MEA-HAp	DES-HAp
Adsorption capacity (mg/g)	5.14	10.24	15.38
Breakthrough time (min)	3.05	6.07	9.13

Impregnated HAp demonstrated higher adsorption capacities and longer breakthrough times than raw HAp. MEA-HAp achieved 10.24 mg/g adsorption capacity at a breakthrough time of 6.07 mins. Its excellent absorption quality was highly related to the change of its surface morphology during the impregnation process. High surface area and good porosity after impregnation improved the adsorption performances of HAp, which was also aligned with the finding reported by (Ghosh et al., 2019). Furthermore, impregnation with MEA introduced the amine group, which promoted basic adsorption sites and CO_2 adsorption (Das & Meikap, 2018).

DES-HAp demonstrated the highest adsorption capacity and breakthrough time among all the samples investigated. It manifested 15.38 mg/g with a breakthrough time of 9.13 min. This observation was repudiated with the low surface area and pore diameter finding, as reported in Section 3.3. The improved CO_2 adsorption could be elucidated by introducing active basic sites with ChCl:U impregnation, promoting chemisorption when reacted with Lewis acidic CO_2 (Raja Shahrom et al., 2019). The findings aligned with the work conducted by Zohdi and his co-authors (2019), where chemisorption was observed through the formation of ammonium carbamate. Unlike raw HAp, which depends highly on physisorption and is mainly controlled by the porosity and surface area of the adsorbent, DES-HAp introduced

DOI: https://doi.org/10.22452/mjs.vol43sp1.8
Malaysian Journal of Science 43 (Special Issue 1): 44-49 (July 2024)

chemisorption through the introduction of basic sites of N. In chemisorption, CO_2 was adsorbed on the adsorbent via chemical bonds and, therefore, independent of the pore characteristics of the adsorbent.

The CO_2 adsorption capacity of DES-HAp obtained in this study is comparable to other reported literature. For instance, Das and Meikap (2018) reported that activated carbon impregnated with MEA had an adsorption capacity of 12.8 to 18.2 for CO_2 gas. In another work by Ariyanto and his co-authors (2021), the CO_2 adsorption capacity of DES-impregnated activated carbon was found in the range of 13.3 to 15.4. These suggest that the DES-HAp produced in this work offers attractive and competitive performance in terms of CO_2 uptake with other impregnated porous adsorbents.

4. Conclusion

In this study, raw HAp was successfully synthesised from eggshells via precipitation. Impregnation modified the porosity of Hap and introduced amine elements. Impregnation using MEA increased the BET surface area due to enhanced porosity. Meanwhile, impregnation using DES caused a reduction in the BET surface area. High porosity improved the adsorption capacity of MEA-HAp when compared with raw HAp. Despite the lower BET surface area, DES-HAp offered the highest adsorption capacity with the longest breakthrough time. These favourable properties are attributed to the presence of amine group, which promotes chemisorption. The findings suggested that ChCl:U-impregnated HAp could be a potential adsorbent for CO_2 capture. The reusability of the adsorbent can be evaluated in future work to increase the economic feasibility of the process.

5. Acknowledgement

This work was supported by the UCSI University Research Excellence & Innovation Grant (Grant number: REIG-FETBE-2023/018).

6. References

Abatan OG., Alaba PA., Oni BA., Akpojevwe K., Efeovbokhan V. & Abnisa F. (2020). Performance of eggshells powder as an adsorbent for adsorption of hexavalent chromium and cadmium from wastewater. SN Applied Sciences 2(12): 1996. https://doi.org/10.1007/s42452-020-03866-w

Agbabiaka OG., Oladele IO., Akinwekomi AD., Adediran AA., Balogun AO., Olasunkanm OG. & Olayanju TMA. (2020). Effect of calcination temperature on hydroxyapatite developed from waste poultry eggshell. Scientific African 8: e00452. https://doi.org/10.1016/j.sciaf.2020.e00452

Ariyanto T., Masruroh K., Pambayun GYS., Mukti NIF, Cahyono RB, Prasetya A. & Prasetyo I. (2021). Improving the separation of CO2/CH4 using impregnation of deep eutectic solvents on porous carbon. ACS Omega 6(29): 19194–19201. https://doi.org/10.1021/acsomega.1c02545

Azmi AA. & Aziz MAA. (2019). Mesoporous adsorbent for CO2 capture application under mild condition: A review. Journal of Environmental Chemical Engineering 7(2): 103022. https://doi.org/10.1016/j.jece.2019.103022

Babaei M. & Haghtalab A. (2023). High-pressure CO2 solubility measurement in aqueous mixtures of (2-amino-2-methyl-1-propanol (AMP) and deep eutectic solvent (tetra butyl ammonium bromide 1: 3 ethylene glycol)) at various temperatures. Fluid Phase Equilibria 565: 113643. https://doi.org/10.1016/j.fluid.2022.113643

Chia SM., Chiong MC., Panpranot J. & Lee KM. (2023). Process optimisation on co-production of lignin and cellulose in deep eutectic solvent pretreatment of oil palm empty fruit bunch. Biomass Conversion and Biorefinery. https://doi.org/10.1007/s13399-023-05025-8

Das D. & Meikap BC. (2018). Comparison of adsorption capacity of mono-ethanolamine and di-ethanolamine impregnated activated carbon in a multi-staged fluidised bed reactor for carbon-dioxide capture. Fuel 224: 47–56. https://doi.org/10.1016/j.fuel.2018.03.090

Ghazali Z., Suhaili N., Tahari MNA., Yarmo MA., Hassan NH. & Othaman R. (2020). Impregnating deep eutectic solvent choline chloride:urea:polyethyleneimine onto mesoporous silica gel for carbon dioxide capture. Journal of Materials Research and Technology 9(3): 3249–3260. https://doi.org/10.1016/j.jmrt.2020.01.073

Ghosh S., Sarathi R. & Ramaprabhu S. (2019). Magnesium oxide modified nitrogen-doped porous carbon composite as an efficient candidate for high pressure carbon dioxide capture and methane storage. Journal of Colloid and Interface Science 539: 245–256. https://doi.org/10.1016/j.jcis.2018.12.063

Ho JY., Chang TT., Ho PC., Chang HK. & Chen PY. (2024). Fabrication of gyroid-structured, hierarchically-porous hydroxyapatite scaffolds by a dual-templating method. Materials Chemistry and Physics 314: 128854. https://doi.org/10.1016/j.matchemphys.2023.128854

Ho PH., Lofty V., Basta A. & Trens P. (2021). Designing microporous activated carbons from biomass for carbon dioxide adsorption at ambient temperature. A comparison between bagasse and rice by-products. Journal of Cleaner Production 294: 126260. https://doi.org/10.1016/j.jclepro.2021.126260

Karimi M., Zafanelli LFAS., Almeida JPP., Ströher GR., Rodrigues AE. & Silva JAC. (2020). Novel insights into activated carbon derived from municipal solid waste for CO2 uptake: Synthesis, adsorption isotherms and scale-up. Journal of Environmental Chemical Engineering 8(5): 104069. https://doi.org/10.1016/j.jece.2020.104069

Khalil S. (2018). Effects on surface area, intake capacity and regeneration of impregnated palm-shell activated carbon with monoethanolamide and 2-amino-2-methyl-1-propanol equipped for CO2 adsorption. Journal of Earth Science &

DOI: https://doi.org/10.22452/mjs.vol43sp1.8
Malaysian Journal of Science 43 (Special Issue 1): 44-49 (July 2024)

Climatic Change 9(7): https://doi.org/10.4172/2157-7617.1000484

Khoshraftar Z. & Ghaemi A. (2022). Presence of activated carbon particles from waste walnut shell as a biosorbent in monoethanolamine (MEA) solution to enhance carbon dioxide absorption. Heliyon 8(1): e08689. https://doi.org/10.1016/j.heliyon.2021.e08689

Latiff AFA., Yee LS., Muhammad MS., Chuan LT & Basri H. (2022). Natural adsorbent made from eggshells for removal of chromium (VI) in water. Biointerface Research in Applied Chemistry 12(1): 518–528. https://doi.org/10.33263/BRIAC121.518528

Makoś P., Słupek E. & Małachowska A. (2020). Silica gel impregnated by deep eutectic solvents for adsorptive removal of BTEX from gas streams. Materials 13(8): 1894. https://doi.org/10.3390/ma13081894

Massayev S. & Lee KM. (2022). Evaluation of deep eutectic solvent pretreatment towards efficacy of enzymatic saccharification using multivariate analysis techniques. Journal of Cleaner Production 360: 132239. https://doi.org/10.1016/j.jclepro.2022.132239

Mignardi S., Archilletti L., Medeghini L. & De Vito C. (2020). Valorisation of eggshell biowaste for sustainable environmental remediation. Scientific Reports 10(1): 2436. https://doi.org/10.1038/s41598-020-59324-5

Raja Shahrom MS., Nordin AR. & Wilfred CD. (2019). The improvement of activated carbon as CO2 adsorbent with supported amine functionalised ionic liquids. Journal of Environmental Chemical Engineering 7(5): 103319. https://doi.org/10.1016/j.jece.2019.103319

Rattanaphan S., Rungrotmongkol T. & Kongsune P. (2020). Biogas improving by adsorption of CO2 on modified waste tea activated carbon. Renewable Energy 145: 622–631. https://doi.org/10.1016/j.renene.2019.05.104

Tangboriboon N., Suttiprapar J., Changkhamchom S. & Sirivat A. (2019). Alternative green preparation of mesoporous calcium hydroxyapatite by chemical reaction of eggshell and phosphoric acid. International Journal of Applied Ceramic Technology 16(5): 1989–1997. https://doi.org/10.1111/ijac.13241

Tizo MS., Blanco LAV., Cagas ACQ., Dela Cruz BRB., Encoy JC., Gunting JV., Arazo RO. & Mabayo VIF. (2018). Efficiency of calcium carbonate from eggshells as an adsorbent for cadmium removal in aqueous solution. Sustainable Environment Research 28(6): 326–332. https://doi.org/10.1016/j.serj.2018.09.002

Trivedi TJ., Lee JH., Lee HJ., Jeong YK. & Choi JW. (2016). Deep eutectic solvents as attractive media for CO2 capture. Green Chemistry 18(9): 2834–2842. https://doi.org/10.1039/C5GC02319J

Unugul T. & Nigiz FU. (2020). Preparation and characterisation an active carbon adsorbent from waste mandarin peel and determination of adsorption behavior on removal of synthetic dye solutions. Water, Air, & Soil Pollution 231(11): 538. https://doi.org/10.1007/s11270-020-04903-5

Zhao H., Luo X., Zhang H., Sun N., Wei W. & Sun Y. (2018). Carbon-based adsorbents for post-combustion capture: A review. Greenhouse Gases: Science and Technology 8(1): 11–36. https://doi.org/10.1002/ghg.1758

Zohdi S., Anbia M. & Salehi S. (2019). Improved CO2 adsorption capacity and CO2/CH4 and CO2/N2 selectivity in novel hollow silica particles by modification with multi-walled carbon nanotubes containing amine groups. Polyhedron 166: 175–185. https://doi.org/10.1016/j.poly.2019.04.001

DOI: https://doi.org/10.22452/mjs.vol43sp1.8
Malaysian Journal of Science 43 (Special Issue 1): 44-49 (July 2024)

MALAYSIAN JOURNAL OF SCIENCE
MJS
ISSN 1394 - 3065

2nd Euro-Asia Conference on CO_2 Capture and Utilization (EACCO2CU2022)

Special issue

Malaysian Journal of Science 43 (Special Issue 1): 50-57 (July 2024)

https://mjs.um.edu.my

IONIC LIQUIDS AS POTENTIAL CO-CATALYST FOR CO_2 ELECTROCHEMICAL REDUCTION

Sulafa Abdalmageed Saadaldeen Mohammed[1a,b], Wan Zaireen Nisa Yahya[2a,c*], Mohamad Azmi Bustam[3a,c] , Muzamil A.Hassan[4d], Asiah Nusaibah Masri[5e], Md Golam Kibria[6f]

Abstract: Carbon dioxide electrochemical reduction (CO_2ER) presents numerous advantages in mitigating greenhouse gas emissions by converting CO_2 into value-added chemicals and can be integrated with renewable energy sources such as solar and wind. Nevertheless, establishing an electrochemically stable catalytic system that can effectively decrease the overpotential while maintaining high current density and faradaic efficiency is challenging. The precise mechanisms causing the reactions and the specific functions of the electrode with electrolytes are still not fully understood. Hence, a significant increase in attention has been paid to using ionic liquids (ILs) as electrolytes for CO_2ER. This phenomenon is attributed to the unique capabilities of ILs to reduce overpotential, increase current density, and improve electrochemical stability. Therefore, this study evaluated the effect of incorporating ILs into electrolytes to comprehend the cation and anion influences on CO_2ER reactions. Linear sweep voltammetry (LSV) and chronoamperometry (CA) were employed to examine the reduction peaks and current density values for different electrolytes, respectively. Consequently, a 0.1 M NBu_4PF_6 acetonitrile solution containing 1-ethyl-3-methylimidazolium tetrafluoroborate [EMIM][BF_4] demonstrated a significantly lower onset potential of the reduction by 320 mV. A reduced CO_2ER efficiency involving ILs with long alkyl chains was also observed. Meanwhile, a novel hypothesis concerning molecular orbitals for the CO_2ER reaction mechanism was discussed. Overall, various performance variables (reduction stability, applied potential, and current density) of CO_2ER were improved using cations with short alkyl chains, anions with high highest occupied molecular orbital (HOMO) levels, and appropriate solvation media. These findings can serve as selection criteria to aid in choosing appropriate ionic liquids for CO_2 electrochemical reduction (CO_2ER).

Keywords: Ionic liquids, CO_2 conversion, electrochemical reduction, COSMO-RS, Turbomole

1. Introduction

Considering the progress of the global economy and society, the growing energy demand is a pressing issue that must be addressed. Despite the considerable advancements in green renewable energy sources (such as solar and wind energy), fossil fuels remain the dominant primary source (accounting for more than 80% of energy output) (Yang *et al*., 2008; Tian *et al*., 2022). Generally, fossil fuels release significant carbon dioxide (CO_2) into the atmosphere, causing its entrapment. Numerous environmental and climate change issues are then observed due to the disruption of the global carbon cycle. Higher sea levels and greenhouse effect intensification are two common examples caused by this phenomenon (Friedlingstein *et al*., 2014). Hence, the negative impacts necessitate a highly effective method for converting CO_2 into valuable compounds to lower the atmospheric CO_2 concentration. Several studies have addressed these issues by efficiently developing strategies to convert CO_2 into valuable carbon-based compounds. These approaches include thermal reduction (Shi *et al*., 2018), biotransformation (Karishma *et al*., 2024), photoelectrochemical (Bi *et al*., 2022), and electrochemical reduction (Gu *et al*., 2022).

The CO_2 electrochemical reduction (CO_2ER) system can produce numerous value-added products through CO_2 conversion, including methane (CH_4), ethylene (C_2H_4), carbon monoxide (CO), methanol (CH_3OH), formic acid (CH_2O_2), and ethanol (C_2H_5OH). Notably, the cathode material is the primary catalyst in the CO_2ER system. Multiple studies by Hori *et al*. also reported the effects of different metal catalysts on CO_2ER, such as Cu, Au, In, Sn, Pb, Zn, Ag, and Pd (Y. Hori *et al*., 1987; Y. Hori *et al*., 1994; Y. i. Hori, 2008). Consequently, Cu and its derivatives have been extensively researched as catalysts due to their unique capability to efficiently convert CO_2 into several higher products, surpassing the production of only CO. These reactions occur at ambient conditions and exhibit high current efficiencies. Nevertheless, ILs have garnered significant interest as an electrolyte for CO_2ER due to their distinctive characteristics,

Authors information:
[a]Chemical Engineering Department, Universiti Teknologi PETRONAS, 32610 Seri Iskandar, Perak, MALAYSIA.
[b]Department of Energy, Aalborg University, 9220 Aalborg, Denmark. E-mail: sasm@energy.aau.dk[1]
[c]Centre for Research in Ionic Liquid, Universiti Teknologi PETRONAS, 32610 Seri Iskandar, Perak, MALAYSIA. E-mail: azmibustam@utp.edu.my[3]
[d]Centre for Biofuel and Biochemical Research, Institute for Sustainable Building, Universiti Teknologi PETRONAS, 32610 Seri Iskandar, Perak, MALAYSIA. E-mail: muzamil.hassan@utp.edu.my[4]
[e]Energy Engineering Department, School of Chemical and Energy Engineering, Faculty of Engineering, Universiti Teknologi Malaysia, 81310 Skudai, Johor, MALAYSIA. E-mail: nusaibah@utm.my[5]
[f]Chemical and Petroleum Engineering, University of Calgary, 2500 University Drive, NW, Calgary, Alberta T2N 1N4, CANADA. E-mail: md.kibria@ucalgary.ca[6]

*Corresponding Author: zaireen.yahya@utp.edu.my

Received: February 7, 2024
Accepted: May 7, 2024
Published: July 31, 2024

DOI: https://doi.org/10.22452/mjs.vol43sp1.9
Malaysian Journal of Science 43 (Special Issue 1): 50-57 (July 2024)

including excellent thermal and chemical stability, good CO_2 solubility, and the capacity to reduce the applied potential (Carlesi *et al*., 2014).

The cations of the ILs have been reported as the primary active component influencing catalytic performance and have garnered significant interest (Lau *et al*., 2016). Specifically, imidazolium-based ILs have demonstrated substantial potential and can be categorised into two divergent mechanisms. Firstly, the ILs and CO_2 form a covalent bonding by carboxylic adduct formation, or that hydride is transmitted. Secondly, the ILs and CO_2 form non-covalent interactions, such as stabilising complexes through alterations in the localised CO_2 environment or hydrogen bonding (Vasilyev *et al*., 2020).

A study by Aki *et al*. (2004) discovered that anions were crucial in determining the solubility of CO_2. The study also denoted that fluoroalkyl-containing anions (such as [TFSI] and [methide]) presented higher solubilities than other anions. Likewise, Snuffin *et al*. (2011) reported that [EMIM][BF_3Cl] with a C_3 symmetric tetrahedral structure was more effective in electroreducing CO_2 compared to [BMIM][BF_4] and [BMIM][TFSI]. This outcome suggested a significant correlation between anion and catalytic performance. Nonetheless, insufficient studies have been observed regarding comprehending the precise reaction mechanisms and the distinct functions of cations and anions in electrochemical reduction reactions.

This study assessed the impact of different ILs on the CO_2 reduction peaks and current density values for two different CO_2ER setups. The molecular orbital energy levels [highest occupied molecular orbital (HOMO) and lowest occupied molecular orbital (LUMO)] of the various cations and anions were determined using a TmoleX simulation software. Furthermore, the impacts of the structure size and the HOMO value of the anion on the catalytic performance of CO_2 reduction were explored.

2. Materials and methods

2.1 Materials

The [BBT][BF_4], [BBT][TFSI], [BMIM][BF_4], and [BMIM][GLY] in this study were synthesised following the methods outlined in the authors' previous article (Mohammed *et al*., 2022). Meanwhile, [EMIM][TFSI] (purity: ≥97.0%) and [HMIM][TFSI] (purity: ≥98.0%) were obtained from Sigma Aldrich without requiring any further purification. Figure 1 illustrates the structures of the selected ILs for this study.

2.2 CO_2ER setup

The electroreduction was conducted in an H-cell, in which an Ag/AgCl electrode was used as the reference electrode, and a Pt mesh of (1 cm × 1 cm) area was employed as the anode in 0.5 M H_2SO_4 anolyte solution. A Nafion 117 membrane was also utilised to separate the catholyte and anolyte to prevent the re-oxidation of the reduction products. This membrane underwent pre-treatment through a series of three sequential steps: (i) pre-treatment using 3% hydrogen peroxide for 1 h at 80°C, (ii) pre-treatment using 0.5 M sulfuric acid solution for 1 h at 80°C, and (iii) rinsing process using distilled water. The purpose of this

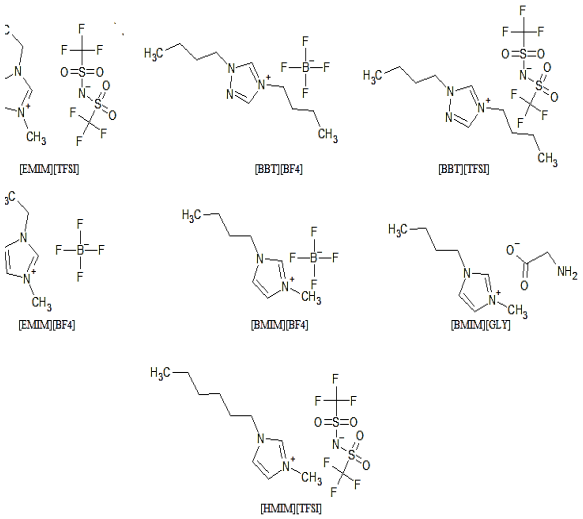

Figure 1. ILs structures used in this study.

procedure was to cleanse the membrane of organic contaminants and protonation of the membrane (Navarra *et al*., 2008). A 0.5 L gas bag was also attached to the catholyte side to collect the gaseous products. Meanwhile, various ILs were introduced as additives into two distinct electrolyte systems based on the solubility of the ILs: (i) 0.1 M $NaHCO_3$ aqueous solution and (ii) 0.1 M NBu_4PF_6 acetonitrile (ACN) solution.

A) CO_2ER in $NaHCO_3$-aqueous based electrolytes

Five different electrolytes were studied as the catholyte, namely 0.1 M $NaHCO_3$-based electrolytes containing 0.02 M of four different ILs, including [BBT][BF_4], [BMIM][GLY], I[EMIM][BF_4], and [BMIM][BF_4], alongside a 0.1 M $NaHCO_3$ solution without any IL. A copper (Cu) plate of 1 cm × 1 cm was used as the cathode, platinum (Pt) mesh as the anode, and Ag/AgCl as the reference electrode. The Cu plate was polished and cleaned using acetonitrile and water and then dried to eliminate particulate residue. Subsequently, N_2 gas was purged into the electrolytes for 15 mins. The pH of the selected electrolytes was then measured using a pH meter. Lastly, the electrolytes underwent a 40-minute purging process with CO_2, followed by an additional step of monitoring the pH before the CO_2ER reaction.

B) CO_2ER in NBu_4PF_6 -based electrolytes

The cathode utilised in this part was a silver disc electrode with a diameter of 2 mm. Seven different catholytes were prepared namely 0.1 M NBu_4PF_6 acetonitrile solutions containing 0.02 M of six ILs including BBT][BF_4], [BBT][TFSI], [EMIM][BF_4], [EMIM][TFSI], [BMIM][BF_4], and [HMIM][TFSI]. A 0.1 M NBu_4PF_6 ACN solution without any IL was also employed as a reference.

2.3 Evaluation of reduction peak and current density

The CO_2ER reaction was assessed using a potentiostat (AutoLAB, PGSTAT128N) equipped with NOVA software. This study then used linear sweep voltammetry (LSV) based on a scan rate of 0.0049 V/s to determine the CO_2 reduction peak. Finally, a chronoamperometry (CA) method was used to conduct the reaction, depending on the reduction peak potential.

DOI: https://doi.org/10.22452/mjs.vol43sp1.9
Malaysian Journal of Science 43 (Special Issue 1): 50-57 (July 2024)

2.4 Molecular computational modelling study

A molecular computer modelling investigation was conducted using TmoleX to optimise the chosen structures and determine the LUMO and HOMO values of these structures. The TmoleX programme utilised parametrisation, incorporating triple-zeta valence with polarisation (TZVP) based on density functional theory (DFT). Typically, the sigma profile and sigma potential present extensive uses in determining the polarity of the molecule (Khan *et al*., 2023; Khan *et al*., 2020; Wojeicchowski *et al*., 2021). Thus, these parameters were generated using COSMO-RS. The classifications of the parameters are as follows: (i) bond donor ($\sigma < -0.01$ e/Å^2), (ii) non-polar area for ($-0.01 < \sigma < +0.01$ e/Å^2), (iii) and hydrogen bond acceptor for ($\sigma > +0.01$ e/Å^2) (Klamt, 2005; Klamt, Jonas, Bürger, & Lohrenz, 1998).

3. Results and discussions

3.1 CO_2ER in 0.1 $NaHCO_3$ aqueous solution

Initially, the impact of introducing ILs on the pH of the CO_2ER system was evaluated. Table 1 tabulates the pH values for the selected electrolytes before and after purging CO_2, showing the pH reduction due to CO_2 absorption. Figure 2 illustrates the CO_2 reduction peaks for various electrolytes. These peaks were obtained using the LSV method to assess the correlation between the IL structure and the potential onset. Consequently, the potential onset followed a specific order beginning with the most favourable option: [EMIM][BF_4] > [BMIM][GLY] > [reference] > [BMIM][BF_4] > [BBT][BF_4].

Table 1. The pH values for the selected electrolytes before and after purging CO_2.

Electrolyte	pH (before CO_2 purging)	pH (after CO_2 purging)
Reference (0.1 $NaHCO_3$)	8.46	7.04
0.1 $NaHCO_3$ + 0.02M [EMIM][BF_4]	8.49	6.97
0.1 $NaHCO_3$ + 0.02M [BMIM][BF_4]	8.41	7.12
0.1 $NaHCO_3$ + 0.02M [BBT][BF_4]	8.49	7.11
0.1 $NaHCO_3$ + 0.02M [BMIM][GLY]	9.02	6.78

A study by Whipple *et al.* (2010) highlighted a negative correlation between pH value and concentration of protons (H^+) in the solution (lower pH = higher H^+), producing a higher CO_2 protonation. Given that the hydrogen evolution reaction (HER) rate competing with the CO_2 reduction reaction for electrons decreased, the production rates of the desired products were accelerated. On the contrary, this study presented that the sequence of pH values (starting from the lowest) did not align with the sequence of potential onsets (starting from the most positive) (see Table 1). Therefore, this outcome implied that no correlation between pH and onset reduction potential was observed. Meanwhile, Snuffin *et al.* (2011) explained that the catalytic reduction of CO_2 using IL salts was caused by the interaction between CO_2 and the anions of ILs, which was based on the Lewis acid-base mechanism.

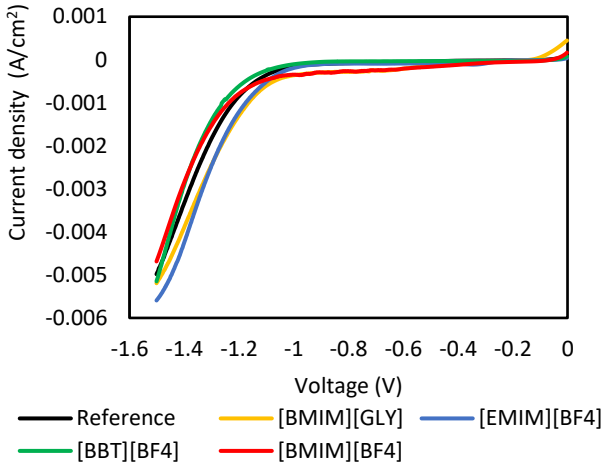

Figure 2. CO_2 reduction peaks for different 0.1 M 0.1 $NaHCO_3$

The CO_2ER reaction for the selected electrolytes was performed using CA for 2 h. Table 2 lists the applied potentials for the selected electrolytes and their corresponding current density values, as shown in Figure 3. Confirming Ohm's law, a higher applied potential resulted in higher current density. Moreover, the electrolyte containing the 0.1 M $NaHCO_3$ + 0.02 M EMIM BF_4 produced a lower applied potential and higher current density than the solution without IL. This finding was highly favourable for the CO_2ER system, in which the significantly higher current density was attributed to the enhanced conductivity arising from a higher concentration of ions in the solution. Therefore, this enhancement provided more charge carriers to facilitate the electric current conduction.

Nevertheless, a substantially lower current density at the same applied potential was observed for the 0.1 M $NaHCO_3$ + 0.02 M BMIM GLY electrolyte than the solution containing EMIM BF_4. This outcome could be explained by the strong interaction between glycinate ions and CO_2 through chemical absorption and extensive solvation, thus limiting the mobility of the ions and

Table 2. The applied potential for selected electrolytes and their corresponding current density

Electrolyte	Applied potential (V)	Current density (mA/cm^2)
Reference (0.1 $NaHCO_3$)	-1.42	-2.9
0.1 $NaHCO_3$ + 0.02M EMIM BF_4	-1.36	-3.8
0.1 NaHCO3 + 0.02M BMIM BF_4	-1.48	-4.9
0.1 $NaHCO_3$ + 0.02M BBT BF_4	-1.44	-4.84
0.1 $NaHCO_3$ + 0.02M BMIM GLY	-1.36	-2.77

DOI: https://doi.org/10.22452/mjs.vol43sp1.9
Malaysian Journal of Science 43 (Special Issue 1): 50-57 (July 2024)

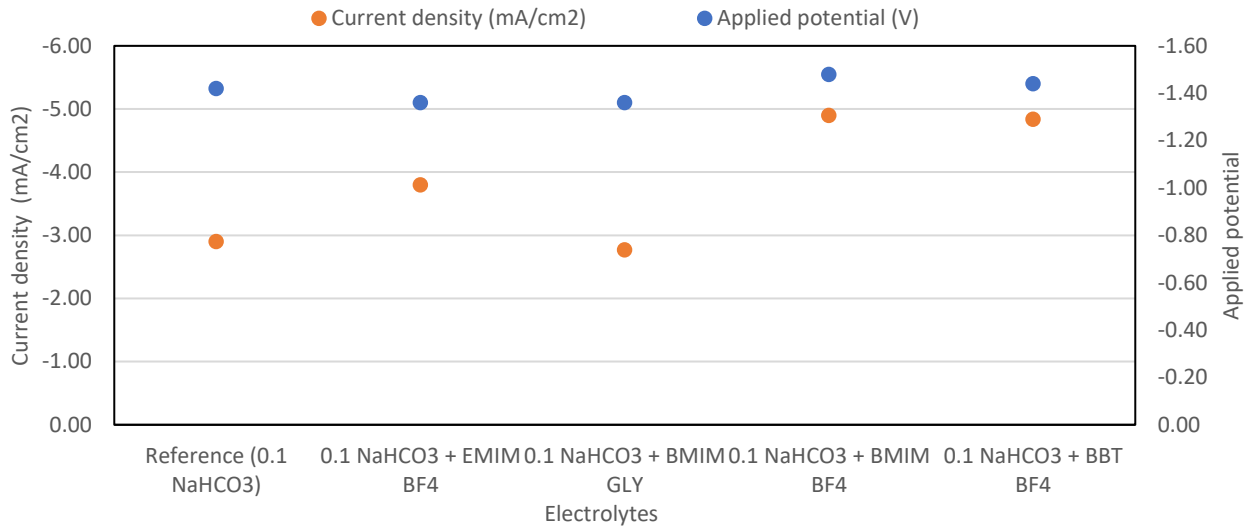

Figure 3: Chronoamperometry results for 0.1 $NaHCO_3$ aqueous electrolytes with and without ILs

decreasing current density (Mohammed *et al*., 2023). The same explanation could also describe the 0.1 M $NaHCO_3$ + 0.02 M BMIM GLY electrolyte demonstrating the lowest pH value. Nevertheless, this condition could be avoided by choosing an electrolyte with high basicity.

The alkyl chain length negatively impacted the transport parameters (conductivity and cation diffusion coefficients) (Every *et al*., 2004). Considering that the length of the alkyl chains in the cation increased, the packing density of the ions dropped, and the space between the cation and anion increased. This process weakened the ion-ion interactions and reduced the dissociation of the ions in the IL, causing a decrease in ionic conductivity. On the contrary, shorter alkyl chains resulted in a greater packing density of the ions and stronger ion-ion interactions, leading to improved ion dissociation and increased ionic conductivity.

3.2 CO_2 ER in 0.1 M NBu_4PF_6 ACN-Based solution

Figure 4 displays the CO_2 reduction peaks for different 0.1 M NBu_4PF_6 ACN-based electrolytes with and without ILs. The CO_2 reduction potential was lower in all electrolytes containing ILs than in the reference electrolyte. The [EMIM][BF_4] electrolyte solution exhibited a lower overpotential of 320 mV compared to the reference solution. Rosen *et al*. (2011) observed that [EMIM][BF_4] demonstrated a 96% faradaic efficiency on the silver cathode (Ag) and a significant capability to decrease the overpotential (approximately 200 mV higher than the equilibrium potential). Furthermore, the electrostatic interaction reduced when the alkyl chain length increased. This process reduced the transport characteristics, leading to more negative onset potential.

Table 3 summarises the results of the CA study at the applied potential and the corresponding current density value for each electrolyte after running the experiment for 30 minutes, with the corresponding graph in Figure 5. The ILs were observed to improve the current density, even at a lower potential than the reference electrolyte. This outcome was attributed to the higher mobility of IL ions compared to the larger structure of NBu_4PF_6.

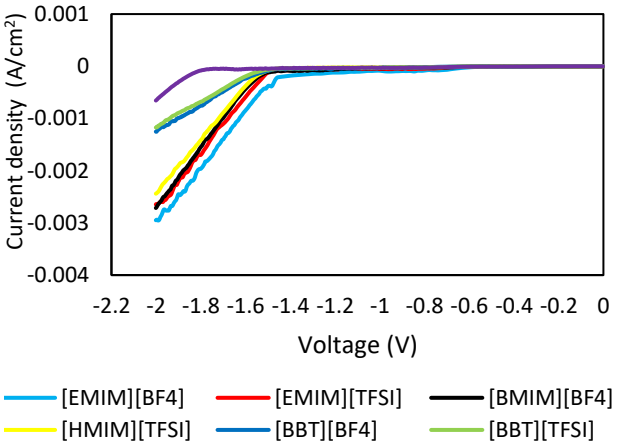

Figure 4: CO_2 reduction peaks in different 0.1 M NBu_4PF_6 acetonitrile-based electrolytes with and without ILs

Table 3. The applied potential for selected electrolytes and their corresponding current density

Electrolyte	Applied potential (V)	Current density (mA/cm²)
Reference (0.1 M NBu_4PF_6 in ACN)	-2.64	-3.40
0.1 M NBu_4PF_6 in ACN + 0.02M EMIM BF_4	-2.32	-4.40
0.1 M NBu_4PF_6 in ACN + 0.02M EMIM TFSI	-2.33	-4.60
0.1 M NBu_4PF_6 in ACN + 0.02M BMIM BF_4	-2.39	-4.40
0.1 M NBu_4PF_6 in ACN + 0.02M BBT BF_4	-2.42	-3.32
0.1 M NBu_4PF_6 in ACN + 0.02M BBT TFSI	-2.44	- 3.60
0.1 M NBu_4PF_6 in ACN + 0.02M HMIM TFSI	-2.34	-4.30

DOI: https://doi.org/10.22452/mjs.vol43sp1.9
Malaysian Journal of Science 43 (Special Issue 1): 50-57 (July 2024)

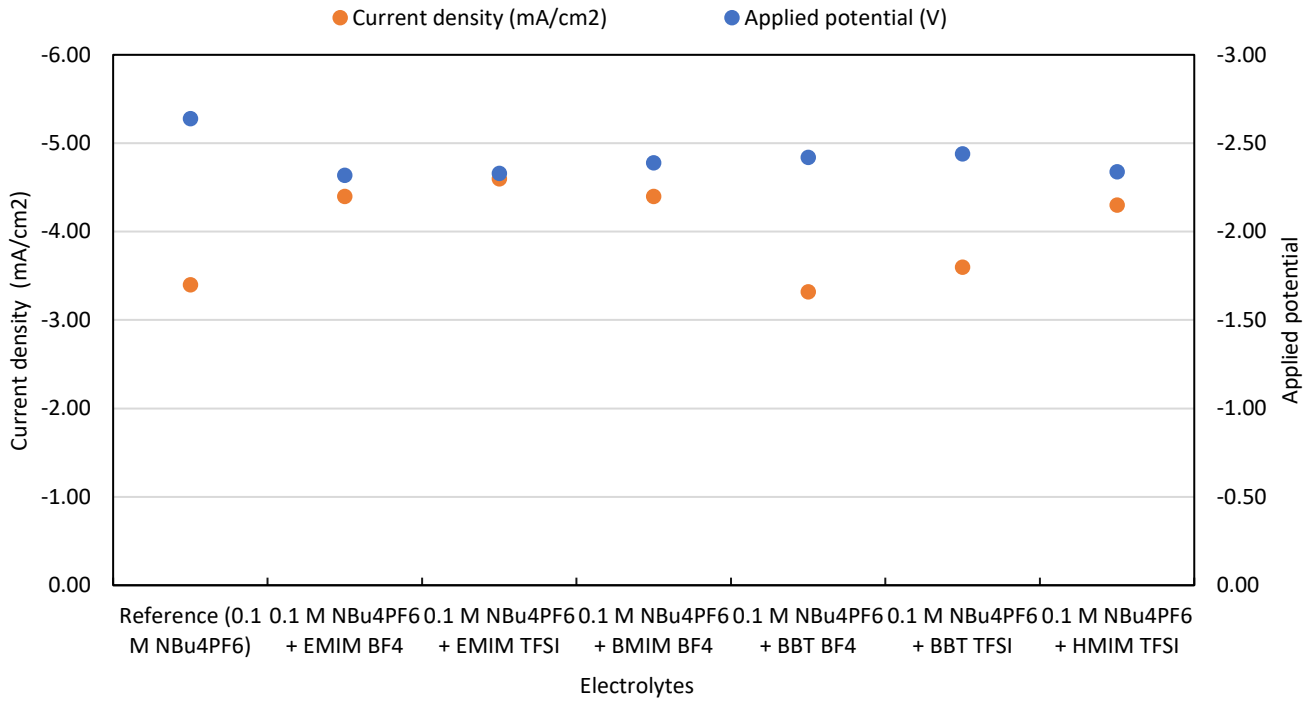

Figure 5: Chronoamperometry results for 0.1 M NBu_4PF_6 acetonitrile-based electrolytes with and without ILs

The applied potential for the same current density at 4.4 mA/cm^2 was also slightly higher for BMIM BF_4 with a longer alkyl chain when comparing the electrolytes containing EMIM BF_4. In addition, the influence of the alkyl chain was more pronounced for BBT BF_4. At a similar applied voltage, the BBT BF_4 exhibited significantly reduced current density compared to BMIM BF_4 due to the presence of the dibutyl chain on the triazolium ring. Thus, this outcome further confirmed that an increase in the alkyl chain length led to decreased ion mobility and increased resistance towards the electrode.

Further investigation of the effects of the IL structure on the molecular orbitals and CO_2ER was performed due to inadequate conclusive evidence. The frontier molecular orbital theory states that the interaction between a Lewis acid and a Lewis base occurs through the interaction of specific frontier orbitals of the acid and base (Fukui, 1975; Liu *et al*., 2020). This interaction involves the transfer of electrons from the HOMO level of the base to the LUMO level of the acid. Therefore, the impact of molecular orbital levels on CO_2 reduction potential is highly relevant. Figure 6 portrays the HOMO and LUMO values of [EMIM], [BMIM], [BBT], [BF_4], [TFSI], and [GLY] calculated using TmoleX.

A significantly higher HOMO value was observed for the [GLY] anion than the [BF_4] anion. Even though the [GLY] anion also demonstrated a notably lower current density than the [BMIM][BF_4], a more favourable onset potential was presented (see Figure 3). Given that CO_2 was the Lewis acid and anions were the Lewis base, anions with higher HOMO values possessed a more significant positive reduction potential. A study by Gomes *et al*. (2022) also highlighted that the [TFSI] anion produced a decreased capability for reducing CO_2 compared to [BF_4]. Typically, the [TFSI] anion exhibits a greater HOMO value in comparison to [BF_4]. Therefore, the anions with higher HOMO values improved the efficiency of CO_2ER by reducing the overpotential. Nonetheless, a significant pH decrease was observed for a strong acid or base interaction between the anion and CO_2 (such as glycinate), which produced a detrimental effect on reducing the current density.

Another study by Monteiro *et al*. (2021) presented three main hypotheses on the impact of cations on the activity and selectivity of electrocatalytic processes at the interface. These hypotheses suggested that the cations modified the local electric field, buffer the interfacial pH, or stabilise reaction intermediates. The study also explained that cation acidity substantially impacted the CO_2ER, which acidic cations promoted CO_2ER at low overpotentials and in acidic media. Meanwhile, Lau et al. (2016) described that the acidic proton at the C_2 position of the

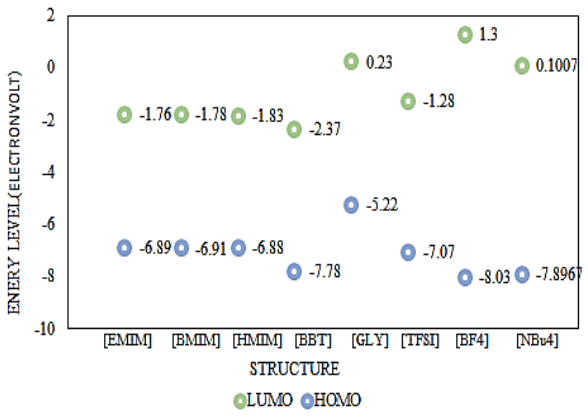

Figure 6. LUMO and HOMO values for the selected structures.

DOI: https://doi.org/10.22452/mjs.vol43sp1.9
Malaysian Journal of Science 43 (Special Issue 1): 50-57 (July 2024)

imidazolium ring stabilised the intermediate CO_2 anion radical by forming hydrogen bonds, which rendered it a significant catalytic site. Similarly, Neyrizi *et al*. (2022) concluded a direct correlation between the performance of CO_2 reduction and acidity of the imidazolium cation (C_2-H).

This study investigated the cation effect on CO_2ER by examining the CO_2 reduction for the same anion. Figure 2 illustrates that for the same anion, the order of CO_2 reduction for [BF_4] (starting from the more positive onset potential) was [EMIM][BF_4] > [BMIM][BF_4] > [BBT][BF_4]. In contrast, the sequence of cation acidity did not follow a similar trend as the CO_2 reduction overpotential, in which the order of LUMO values of the cations (starting from the lowest) was [BBT] < [BMIM] < [EMIM]. Our previous study deduced that a low LUMO value of the cation (acidity) enhanced the solubility of CO_2 by facilitating an acid/base interaction between the cation and the negatively charged oxygen (Mohammed *et al*., 2023). Therefore, a long cation alkyl chain could present difficulties reaching the electrode surface, impeding its proximity with the electrons. This observation was attributed to the positively charged nitrogen atom of the cation that was relatively far from the electrode surface due to the long alkyl chain.

Coulomb's law states that the electrostatic attraction or repulsion intensity between two-point charges is directly proportional to the product of their magnitudes and inversely proportional to the square of the distance between them. A study by Azra *et al*. (2022) supported this statement by demonstrating the correlation between long alkyl chains and molecular interaction. The study highlighted the significance of chain length in separating organic and aqueous phases, in which longer chain lengths promoted easy separation. In contrast, shorter chain lengths enhanced water clarity, hindering complete separation and resulting in lower extraction efficiency. Considering that the disparity in the LUMO values between the cations was not substantial, the long alkyl chain of a cation decreased the interaction between its positively charged nitrogen and the electrons on the electrode to a greater extent than the magnitude of the charge. When an electric potential was provided, the positively charged ions migrated towards the negatively charged electrode (cathode). Consequently, the long non-polar alkyl chain decreased or increased the mobility of the ions or resistance towards the electrode, respectively.

Figure 5 demonstrates that the inclusion of ILs significantly improves the system. This observation was due to the inclusion of ILs enhancing the acid or base interaction with CO_2. Additionally, a higher non-polar/non-polar interaction with CO_2 and lower acid/base interaction was observed owing to the large structure and the long alkyl chain of NBu_4PF_6. Figure 7 depicts the sigma profile and sigma potential of the cations and anions. Similar to CO_2, the NBu_4PF_6 was highly non-polar. Overall, the CO_2 exhibited a dual nature, with both partially charged properties that allowed it to interact with its environment through acid/base interaction and non-polar characteristics (due to the linear structure of its bonds). Thus, the CO_2ER was greatly affected by the interaction between CO_2 and the electrolyte environment.

Another study by Ueno *et al*. (2010) denoted that the solvation of strongly Lewis basic anions and highly Lewis acidic cations by solvents enabled a substantial level of salt dissociation. Therefore, selecting a favourable combination of ILs with a short alkyl chain, an anion with a high HOMO value, and a compatible

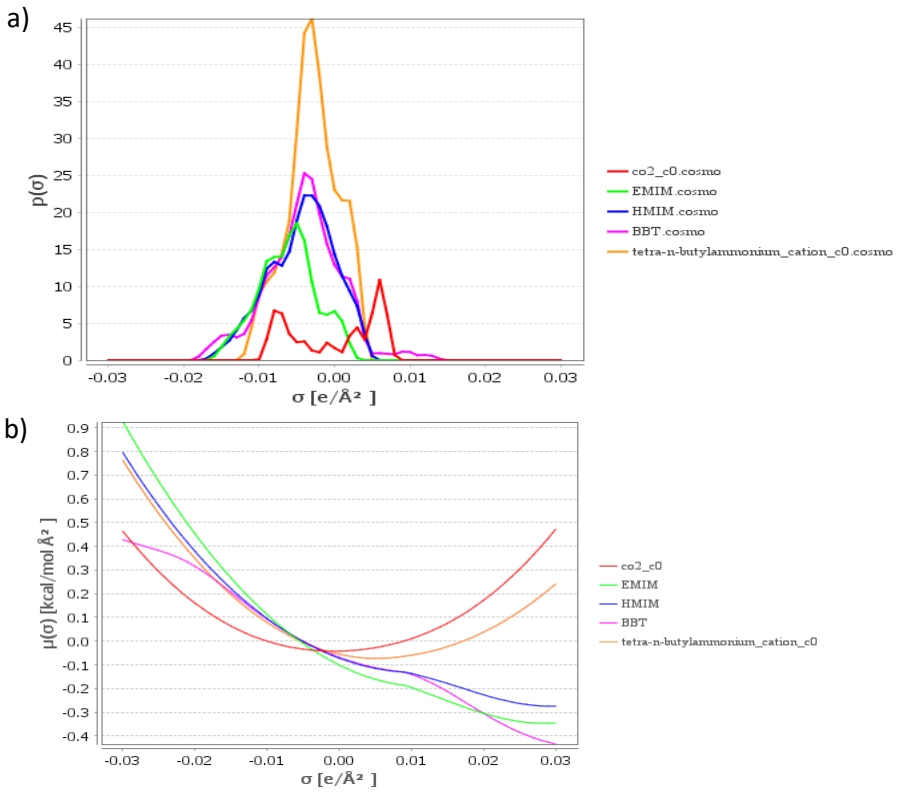

Figure 7: Sigma profile (a) and sigma potential (b) of the cations and anions of ILs including CO_2

DOI: https://doi.org/10.22452/mjs.vol43sp1.9
Malaysian Journal of Science 43 (Special Issue 1): 50-57 (July 2024)

solvent increased the current density. The performance of the CO_2ER system was also reduced when the non-polar/non-polar interaction between the ILs and CO_2 was dominant. Thus, cations with short alkyl chains and anions with high HOMO values were essential to improve the acid/base interaction between CO_2 and electrolytes for optimal performance of ILs in CO_2ER. Notably, cations with short alkyl chains lowered the resistance to charge resistance at the electrode.

4. Conclusion

In this study, The CO_2 reduction peaks, and the current density of different electrolytes were evaluated using linear sweep voltammetry (LSV), and chronoamperometry (CA). HPLC and GC-TCD were used to confirm the formation of the reaction products. The addition of 1-ethyl-3-methylimidazolium tetrafluoroborate [EMIM][BF_4] to the 0.1 M NBu_4PF_6 acetonitrile solution demonstrates that the reduction's onset potential significantly decreased by 320 mV. It can be concluded that to have effective ionic liquid as electrolyte for CO_2ER reaction, in order to have low overpotential and high current density, the acid/base interaction with IL and CO_2 is desirable , and for that ILs with small alkyl chain, low LUMO values of cations and high HOMO values as anions are recommended while considering the suitable organic solvent.

5. Acknowledgement

The Fundamental Research Grant Scheme initiative of the Malaysian Ministry of Higher Education provided funding for this study (MOHE-FRGS/1/2021/TK0/UTP/02/12). Additionally, the authors acknowledge the Chemical Engineering Department, the Centre for Research in Ionic Liquids (CORIL), the Centre for Biofuel and Biochemical Research (CBBR), and Centre for Corrosion Research (CCR) of Universiti Teknologi PETRONAS (UTP) for their technical assistance and resources.

6. References

Aki, S. N., Mellein, B. R., Saurer, E. M., & Brennecke, J. F. (2004). High-pressure phase behavior of carbon dioxide with imidazolium-based ionic liquids. *The Journal of Physical Chemistry B, 108*(52), 20355-20365.

Azra, N., Nazir, F., Roosh, M., Khalid, M. A., Mansoor, M. A., Khan, S. B., & Iqbal, M. (2022). Extraction of Pb (II) and Co (II) using N, N-dioctylsuccinamate based room temperature ionic liquids containing aliphatic and aromatic cations. Arabian Journal of Chemistry, 15(9), 104099.

Bi, Z.x., Guo, R.t., Hu, X., Wang, J., Chen, X., & Pan, W.g. (2022). Research progress on photocatalytic reduction of CO_2 based on LDH materials. *Nanoscale, 14*(9), 3367-3386.

Carlesi, C., Carvajal, D., Vasquez, D., & Arratia, R. S. (2014). Analysis of carbon dioxide-to-methanol direct electrochemical conversion mediated by an ionic liquid. *Chemical Engineering Processing: Process Intensification 85*, 48-56.

Every, H. A., Bishop, A. G., MacFarlane, D. R., Orädd, G., & Forsyth, M. (2004). Transport properties in a family of dialkylimidazolium ionic liquids. *Physical Chemistry Chemical Physics, 6*(8), 1758-1765.

Friedlingstein, P., Andrew, R. M., Rogelj, J., Peters, G. P., Canadell, J. G., Knutti, R., . van Vuuren, D. P. (2014). Persistent growth of CO_2 emissions and implications for reaching climate targets. *Nature geoscience, 7*(10), 709-715.

Fukui, K. (1975). *Theory of Orientation*: Springer.

Gu, J., Liu, S., Ni, W., Ren, W., Haussener, S., & Hu, X. (2022). Modulating electric field distribution by alkali cations for CO_2 electroreduction in strongly acidic medium. *Nature Catalysis, 5*(4), 268-276.

Hori, Y., Murata, A., Kikuchi, K., & Suzuki, S. (1987). Electrochemical reduction of carbon dioxides to carbon monoxide at a gold electrode in aqueous potassium hydrogen carbonate. *Journal of the Chemical Society, Chemical Communications*, 728-729.

Hori, Y., Wakebe, H., Tsukamoto, T., & Koga, O. (1994). Electrocatalytic process of CO selectivity in electrochemical reduction of CO_2 at metal electrodes in aqueous media. *Electrochimica Acta, 39*(11-12), 1833-1839.

Hori, Y.,(2008). Electrochemical CO_2 reduction on metal electrodes. In *Modern aspects of electrochemistry* (pp. 89-189): Springer.

Khan, H. W., Khan, M. K., Moniruzzaman, M., Al Mesfer, M. K., Danish, M., Irshad, K., . Chelliapan, S. (2023). Evaluating ionic liquids for its potential as eco-friendly solvents for naproxen removal from water sources using COSMO-RS: Computational and experimental validation. *Environmental Research*, 116058.

Khan, H. W., Reddy, A. V. B., Nasef, M. M. E., Bustam, M. A., Goto, M., & Moniruzzaman, M. (2020). Screening of ionic liquids for the extraction of biologically active compounds using emulsion liquid membrane: COSMO-RS prediction and experiments. *J. Mol. Liq., 309*, 113122.

Klamt, A. (2005). *COSMO-RS: from quantum chemistry to fluid phase thermodynamics and drug design*. Germany: Elsevier.

Klamt, A., Jonas, V., Bürger, T., & Lohrenz, J. C. (1998). Refinement and parametrization of COSMO-RS. *J. Phys. Chem A, 102*(26), 5074-5085.

Lau, G. P., Schreier, M., Vasilyev, D., Scopelliti, R., Grätzel, M., & Dyson, P. J. (2016). New insights into the role of imidazolium-based promoters for the electroreduction of CO_2 on a silver electrode. *Journal of the American Chemical Society, 138*(25), 7820-7823.

Lau, G. P. S., Schreier, M., Vasilyev, D., Scopelliti, R., Grätzel, M., & Dyson, P. J. (2016). New Insights into the Role of Imidazolium-Based Promoters for the Electroreduction of CO_2 on a Silver Electrode. *Journal of the American Chemical Society, 138*, 7820-7823.

DOI: https://doi.org/10.22452/mjs.vol43sp1.9
Malaysian Journal of Science 43 (Special Issue 1): 50-57 (July 2024)

Liu, C., Li, Y., Takao, M., Toyao, T., Maeno, Z., Kamachi, T., . . . Shimizu, K.i. (2020). Frontier molecular orbital based analysis of solid–adsorbate interactions over group 13 metal oxide surfaces. *The Journal of Physical Chemistry C 124*(28), 15355-15365.

Mohammed, S. A. S., Yahya, W. Z. N., Bustam, M. A., & Kibria, M. G. (2023). Experimental and Computational Evaluation of 1, 2, 4-Triazolium-Based Ionic Liquids for Carbon Dioxide Capture. *Separations, 10*(3), 192.

Mohammed, S. A. S., Yahya, W. Z. N., Bustam, M. A., Kibria, M. G., Masri, A. N., & Kamonwel, N. D. M. (2022). Study of the ionic liquids' electrochemical reduction using experimental and computational methods. *Journal of Molecular Liquids*, 119219.

Monteiro, M. C., Dattila, F., Hagedoorn, B., García-Muelas, R., López, N., & Koper, M. T. (2021). Absence of CO_2 electroreduction on copper, gold and silver electrodes without metal cations in solution. *Nature Catalysis, 4*(8), 654-662.

Navarra, M., Abbati, C., & Scrosati, B. (2008). Properties and fuel cell performance of a Nafion-based, sulfated zirconia-added, composite membrane. *Journal of power sources, 183*(1), 109-113.

Neyrizi, S., Kiewiet, J., Hempenius, M. A., & Mul, G. (2022). What It Takes for Imidazolium Cations to Promote Electrochemical Reduction of CO_2. *ACS Energy Letters, 7*(10), 3439-3446.

Rosen, B. A., Haan, J. L., Mukherjee, P., Braunschweig, B., Zhu, W., Salehi-Khojin, A., . Masel, R. I. (2012). In situ spectroscopic examination of a low overpotential pathway for carbon dioxide conversion to carbon monoxide. *Journal of Physical Chemistry C, 116*, 15307-15312.

Rosen, B. A., Salehi-Khojin, A., Thorson, M. R., Zhu, W., Whipple, D. T., Kenis, P. J. A., & Masel, R. I. (2011). Ionic liquid-mediated selective conversion of CO_2 to CO at low overpotentials. *Science, 334*, 643-644.

Shi, Z., Yang, H., Gao, P., Chen, X., Liu, H., Zhong, L., . Sun, Y. (2018). Effect of alkali metals on the performance of CoCu/TiO2 catalysts for CO2 hydrogenation to long-chain hydrocarbons. *Chinese Journal of Catalysis, 39*(8), 1294-1302.

Snuffin, L. L., Whaley, L. W., & Yu, L. (2011). Catalytic electrochemical reduction of CO_2 in ionic liquid $EMIMBF_3Cl$. *Journal of The Electrochemical Society, 158*, 155-158.

Tian, J., Yu, L., Xue, R., Zhuang, S., & Shan, Y. (2022). Global low-carbon energy transition in the post-COVID-19 era. *Applied energy 307*, 118205.

Ueno, K., Tokuda, H., & Watanabe, M. (2010). Ionicity in ionic liquids: correlation with ionic structure and physicochemical properties. *Physical Chemistry Chemical Physics, 12*(8), 1649-1658.

Vasilyev, D. V., Shyshkanov, S., Shirzadi, E., Katsyuba, S. A., Nazeeruddin, M. K., & Dyson, P. J. (2020). Principal descriptors of ionic liquid co-catalysts for the electrochemical reduction of CO_2. *ACS Applied Energy Materials, 3*(5), 4690-4698.

Whipple, D. T., Finke, E. C., & Kenis, P. J. (2010). Microfluidic reactor for the electrochemical reduction of carbon dioxide: the effect of pH. *Electrochemical Solid-State Letters, 13*(9), B109.

Wojeicchowski, J. P., Abranches, D. O., Ferreira, A. M., Mafra, M. R., Coutinho, J. o. A., & Engineering. (2021). Using COSMO-RS to Predict Solvatochromic Parameters for Deep Eutectic Solvents. *ACS Sustainable Chemistry, 9*(30), 10240-10249.

Yang, H., Xu, Z., Fan, M., Gupta, R., Slimane, R. B., Bland, A. E., & Wright, I. (2008). Progress in carbon dioxide separation and capture: A review. *Journal of environmental sciences, 20*(1), 14-27.

DOI: https://doi.org/10.22452/mjs.vol43sp1.9
Malaysian Journal of Science 43 (Special Issue 1): 50-57 (July 2024)

MALAYSIAN JOURNAL OF SCIENCE
MJS
ISSN 1394 - 3065

2nd Euro-Asia Conference on CO_2 Capture and Utilization (EACCO2CU2022) Special Issue

Malaysian Journal of Science 43 (Special Issue 1): 58-66 (July 2024) https://mjs.um.edu.my

INVESTIGATION OF CARBON DIOXIDE ABSORPTION CAPACITY AND DISSOLUTION RATE WITH AMINO ACID SALT SOLUTIONS: SODIUM AND POTASSIUM GLYCINATE

İrem Koçyiğit Çapoğlu[1a], Duygu Uysal[2b*] and Özkan Murat Doğan[3c]

Abstract: Global warming is a major world problem and causes climate change. The primary cause of global warming is carbon dioxide (CO_2) emissions. Ongoing studies are being conducted to mitigate the effects of this problem. Anthropogenic CO_2 emissions occur by burning fossil fuels to generate power and heat. To combat this problem, CO_2 must be captured from point emission sources or directly from air. The conventional method to remove CO_2 at the point emission sources is post-combustion systems. In these systems, absorption process is generally used to diminish CO_2 emission and capturing at the source. Current researches aim to find an efficient and alternative solution to absorption. In this work, sodium glycinate (NaGly) and potassium glycinate (KGly), which are amino acid salt solutions, were investigated for CO2 absorption. Amino acid salt solutions have shown similar absorption kinetics and capacities to amine-based solutions due to same functional group. These solutions are usually more stable to oxidative degradation and have low volatilities, higher surface tensions and the viscosities are very close to waters. Experiments were performed using a stirred cell system at ambient temperature (20°C) and atmospheric pressure (91 kPa), in Ankara, Türkiye. In experiments, sodium glycinate and potassium glycinate concentration was ranged between 0.1 and 1.5 M. The experiments were also repeated with sodium hydroxide and potassium hydroxide in the same concentration range for comparison. In addition, the amino acid salt solutions examined in this study were compared with alkaline solutions and glycine in terms of total CO_2 absorption capacity and CO_2 dissolution rate. As a result of the experiments, the potassium glycinate solutions gave approximately 1.4 times better results than the sodium glycinate solutions at the highest concentration. Also, functional groups were determined by FTIR analysis of pure and CO_2-loaded potassium glycinate solution.

Keywords: carbon dioxide, absorption, amino acid, sodium glycinate, potassium glycinate.

1. Introduction

Carbon dioxide (CO_2) emissions rapidly increase worldwide, most of which stem from anthropogenic activities. The latest atmospheric CO_2 concentration reached 421 ppm in May 2023 and this trend unfortunately continuously increasing (NASA, 2023). According to the Intergovernmental Panel on Climate Change (IPCC), CO_2 emissions must reach net zero by 2050 with no or limited temperature rise (IPCC, 2022). Using fossil fuels in combustion processes with increasing energy demand is directly associated with excessive CO_2 concentrations in the atmosphere. Humanity's main energy source is still fossil fuels, and CO_2 must be captured from the atmosphere or point emission sources (such as power plants) to reduce emissions (Yuan et al., 2022; Keith et al., 2018). Carbon dioxide capture and storage (CCS) or carbon dioxide capture and utilization (CCU) technologies are considered to have significant potential for decarbonization (Zhang & Huisingh, 2017). To capture CO_2 there are three systems recommended mainly: pre-combustion, post-combustion, and oxy-fuel combustion. (Buckingham et al., 2022; Ahmed et al., 2020). The gas streams' pressure, CO_2 concentration, and fuel type (e.g., coal or natural gas) are considerable factors in choosing the capture system (Olajire, 2010).

In post-combustion capture systems, CO_2 is captured from flue gases produced because of the combustion of fuels with high carbon sources such as fossil fuels and biomass. Post-combustion systems use a liquid solution to capture the small fraction of CO_2 (typically 3–15% by volume) present in a flue gas stream (IPCC, 2005). Post-combustion carbon capture has important potential because it can be retrofitted to existing units in the power sector. Currently, conventional pulverized coal (PC) power plants or natural gas combined cycle (NGCC) power plants use post-combustion capture systems that employ an organic solution such as monoethanolamine (MEA) (Figueroa et al., 2008).

There are many methods for capturing CO_2. Common methods for CO_2 capture are absorption, adsorption, separation with a membrane, cryogenic separation, etc. (Wu et al., 2020). Among all these systems and methods, the most used system is the post-combustion/absorption mechanism because of reliable technology, large operation capacity, and longtime industrial process experience (Wang et al., 2011; Ochedi et al., 2021). CO_2 absorption with the solution can occur in two ways: physical or chemical absorption. There are several CO_2 capture solutions available including, alkanolamine solutions (Murrieta-Guevara et

Authors information:
[a]Graduate School of Natural and Applied Sciences, Main Campus, Gazi University, 06500, Ankara, Türkiye, E-mail: iremkocyigit@gazi.edu.tr[1]
[b]Chemical Engineering Department, Gazi University, Faculty of Engineering, Maltepe, Ankara, 06570, Türkiye, E-mail: duysal@gazi.edu.tr[2]
[c]Chemical Engineering Department, Gazi University, Faculty of Engineering, Maltepe, Ankara, 06570, Türkiye, E-mail: mdogan@gazi.edu.tr[3]

*Corresponding Author: duysal@gazi.edu.tr

Received: February 7, 2024
Accepted: May 7, 2024
Published: July 31, 2024

DOI: https://doi.org/10.22452/mjs.vol43sp1.10
Malaysian Journal of Science 43 (Special Issue 1): 58-66 (July 2024)

al., 1988; Puxty et al., 2009; Bernhardsen & Knuutila, 2017), ionic liquids (ILs) (Babamohammadi et al., 2015), liquid ammonia (Wang et al., 2018), polyethylene glycol (Li et al., 2012), methanol (Gatti et al., 2014), potassium carbonate (Ghosh et al., 2009), and others. Alkanolamine solutions such as monoethanolamine (MEA), diethanolamine (DEA), and methyl diethanolamine (MDEA) are mostly used as an absorbent in commercial applications (Aghel et al., 2021). However, these solutions have several drawbacks related to limited cyclic carbon dioxide loading capacity, degradation by oxygen, high equipment corrosion and the operating cost is fairly high due to the high energy requirement for regeneration of the solution (Ahn et al., 2010; Luis, 2016). Therefore, studies on CO_2 absorption have focused on finding efficient, environmentally friendly energy-saving alternative solutions that may eliminate the disadvantages of the current systems.

Recently, it has been seen that amino acid salts have shown significant potential in CO_2 absorption. The latest research shows that amino acid salts could be replaced with alkanolamine solutions due to their molecular structure similarity (Kumar et al., 2003; Harris et al., 2009). Amino acid salts are formed by equimolar mixing an alkaline solution with amino acids such as glycine and sarcosine (Lee et al., 2007). Amino acid salt solutions have certain advantages over amines such as higher surface tension, low volatility, low toxicity, high biodegradation potential, resistance to oxidative degradation, and better absorption capacity (Guo et al., 2013; Majchrowicz et al., 2014; Hu et al., 2018). Because of these substantial properties, amino acid salt solutions have been used commercially as the promoters in carbonate solutions in the Giammarco-Vetrocoke process (Thee et al., 2013), selective acid gas removal from industrial gas streams in the Alkacid process by BASF (Vaidya et al., 2010), as precipitating solutions in the DECAB process (Fernandez & Goetheer, 2011), and in post-combustion CO_2 capture in the Siemens POSTCAP process (Majchrowicz et al., 2014).

The absorption of monoethanolamine (MEA) and amino acid salt solutions with carbon dioxide is chemical absorption. Similar to primary and secondary amines, since it has the same functional groups (amine groups), CO_2 is expected to react with the amino acid salt solution via the zwitterionic mechanism (Kumar et al., 2003; Lee et al., 2007). The zwitterion mechanism was first introduced by Caplow (1968) and later explained by Danckwerts (1979). The general reactions occurring during amine-CO_2 absorption can be summarized as carbamate formation, bicarbonate formation, and carbonic acid formation.

In amine-CO_2 absorption, first the free electrons in the nitrogen atom attack the carbon atom in the CO_2 and form the zwitterion. The zwitterion formation reaction is shown by Eq. (1) (Caplow, 1968; Kumar et al., 2003; Lee et al., 2007).

$$CO_2 + RNH_2 \underset{k_{-1}}{\overset{k_2}{\rightleftarrows}} RNH_2^+COO^- \quad (1)$$

Considering MEA, the R expression can be expressed as: $R = HOCH_2CH_2 -$. Subsequently, it gives the zwitterion proton to a free base, forming carbamate (carbamic acid). The proton transfer to the free base B is shown by Eq. (2). In this reaction, the proton transfer reaction can be considered irreversible as the equilibrium predominates on the right side of the reaction (Majchrowicz et al., 2014).

$$RNH_2^+COO^- + B \overset{k_B}{\rightarrow} RNHCOO^- + BH^+ \quad (2)$$

The base referred to herein as B may be any of the amine, water, or hydroxyl (OH^-) groups. The contribution of these groups during proton transfer is shown by Eq. (3), Eq. (4), and Eq. (5) (Lee et al., 2007)

$$RNH_2^+COO^- + H_2O \rightarrow RNHCOO^- + RNH_3^+ \quad (3)$$

$$RNH_2^+COO^- + RNH_2 \rightarrow RNHCOO^- + H_3O^- \quad (4)$$

$$RNH_2^+COO^- + OH^- \rightarrow RNHCOO^- + H_2O \quad (5)$$

During the formation of zwitterion, the reaction of carbon dioxide with hydroxyl ions in the water also occurs simultaneously, albeit in small amounts, and bicarbonate ions are formed. The reactions are shown by Eq. (6) and Eq. (7).

$$H_2O \rightleftarrows H^+ + OH^- \quad (6)$$

$$CO_2 + OH^- \rightleftarrows HCO_3^- \quad (7)$$

The carbonic acid formation reaction is quite slow and negligible (Lee et al., 2007). The reaction is shown by Eq. (8).

$$CO_2 + H_2O \rightleftarrows HCO_3^- + H^+ \quad (8)$$

The reaction rate of the quasi-steady state between CO_2 and amino acids for the zwitterionic mechanism (considering all possible free bases-$\sum k_b\,[B]$) can be described as follow:

$$r_{CO_2,abs} = \frac{k_2\,[CO_2][Am]}{1+\frac{k_{-1}}{k_b\,[B]}} \quad \frac{[CO_2][RNH]}{\frac{1}{k_2}+\frac{k_{-1}}{k_2}\frac{1}{\sum k_b\,[B]}} = k_{app}\,[CO_2] \quad (9)$$

Here, k_{app} is called the apparent rate constant. If the deprotonation of the zwitterion is much faster than the reverse rate of the first reaction $\left(\frac{k_{-1}}{\sum k_b\,[B]} \ll 1\right)$, the rate of absorption of carbon dioxide is reduced to a simple second-order reaction rate expression. In this case, the reaction rate equation is shown as in Eq. (10).

$$r_{CO_2,abs} = k_2\,[CO_2][RNH] = k_{app}\,[CO_2] \quad (10)$$

While the above expression is accepted as valid for simple amine groups such as MEA, the reaction expression is shown as in Eq. (11) since $\left(\frac{k_{-1}}{\sum k_b\,[B]} \gg 1\right)$ for large volume amine groups.

$$r_{CO_2,abs} = k_2\,[CO_2][RNH]\left(1+\frac{\sum k_b\,[B]}{k_{-1}}\right) \cong k_2\,[CO_2][RNH]\left(\frac{\sum k_b\,[B]}{k_{-1}}\right) = k_{app}\,[CO_2] \quad (11)$$

Considering the reaction of CO_2 directly with hydroxyl ions in water, the total rate constant and reaction rate expression can be written as Eq. (12) and Eq. (13).

$$k_{ov} = k_{app} + k_{OH^-}[OH^-] \quad (12)$$

$$r_{CO_2,abs} = k_{ov}\,[CO_2] \quad (13)$$

This work focuses on the determination of the total CO_2 absorption capacity and dissolution rate of the amino acid salt solutions potassium glycinate (KGly) and sodium glycinate (NaGly) and their comparison with alkaline solutions sodium hydroxide

DOI: https://doi.org/10.22452/mjs.vol43sp1.10
Malaysian Journal of Science 43 (Special Issue 1): 58-66 (July 2024)

(NaOH) and potassium hydroxide (KOH). All experiments were carried out in a stirred cell at ambient temperature (20°C) and atmospheric pressure (91 kPa). pH measurements of the solutions were made before and after CO_2 absorption. The solution concentration varied between 0.1 to 1.5 M. In addition, amino acid functional groups were determined by FTIR analysis of potassium glycinate solution. FTIR analysis was applied to both pure potassium glycinate solution and CO_2-loaded potassium glycinate solution, and the results are presented in this study.

2. Materials and methods

2.1 Materials

The CO_2 gas cylinder (>99.99%) was supplied from Samtaş A.Ş. Glycine were purchased from Carlo Erba and, sodium hydroxide (NaOH) and potassium hyrdroxide (KOH) pellets were purchased from Merck. Aqueous sodium glycinate and potassium glycinate solutions were prepared by neutralizing glycine dissolved in distilled water, with equimolar sodium hydroxide and potassium hydroxide, respectively. The measurements of weight were employed using an analytical balance with an ±0.1 mg accuracy. During the experiments, the absorption solution was stirred with a VELP SCIENTIFICA ARE model magnetic stirrer. The pressure drop in the system was measured with HK Instruments DPT-R8 model pressure transmitter and recorded on the computer with the ORDEL UDL100 model data logger. In all experiments, pH measurements were made with a WTW pH 3110 model pH meter.

2.2 Experimental Set-Up

Experiments were carried out in stirred cell reactor. Stirred cell reactor is a known equipment for employed reaction and mass transfer studies in gas-liquid systems (Kucka et al., 2003; Ying & Eimer 2013). Stirred cell reactor experiment principle is based on the gas in the gas chamber being absorbed into the liquid in time. By observing the pressure drop in the gas chamber along with the amount of gas absorbed into the liquid, it is possible to calculate how much gas is absorbed. The schematic experimental set-up is shown in Fig. (1).

The stirred cell reactor system consists of two parts, a 0.5 L gas chamber and a 0.4 L liquid reservoir. The reactor part is made of pyrex glass. The gas chamber has valves to which the gas inlet and outlet are connected. A CO_2 gas cylinder is attached to the gas chamber. Before the gas was fed to the system, it was passed through the humidifier to keep the temperature constant at the gas-liquid interface. Absorption liquid is placed in the liquid reservoir. Two parts of the system are connected by a metal clamp to seal the system.

2.3 Experimental Procedure

In the experiments, firstly, pure CO_2 gas flow is fed to the reactor from the gas inlet, and the air inside the system was swept. Afterward, all valves are closed simultaneously, and CO_2 gas is trapped in the gas chamber. Then, trapped CO_2 gas in the system is absorbed into the absorption solution. As CO_2 is absorbed by the solution, the pressure inside the gas chamber decreased until the constant value is reached. Meanwhile, the absorption solution is stirred with a magnetic stirrer regarding no vibration/vortex forms at the interface.

Through this stirring, mass transfer resistances that may occur on the liquid surface and in the areas close to the surface are prevented by providing homogeneity in the liquid. Also, the solution temperature is instantaneously controlled by a thermocouple with ± 0.2 K accuracies. In the experiments, the pressure drop occurring in the gas chamber is instantly recorded every second on the computer with a data logger using a differential pressure transmitter. While the pressure drop values occurring in the stirred cell reactor were increased at the beginning over time, they were fixed after a while. Then, the total CO_2 absorption capacity and dissolution rate were calculated using the recorded values.

In the experiments glycine, sodium hydroxide, potassium hydroxide, sodium glycinate, and potassium glycinate were used as absorbents with a molar range of 0.1-1.5 M. All experiments were conducted at an ambient temperature of 20°C and an atmospheric pressure of 91 kPa, in Ankara, Türkiye. In all experiments, pH measurements of solutions were made with a pH meter before and after the experiment.

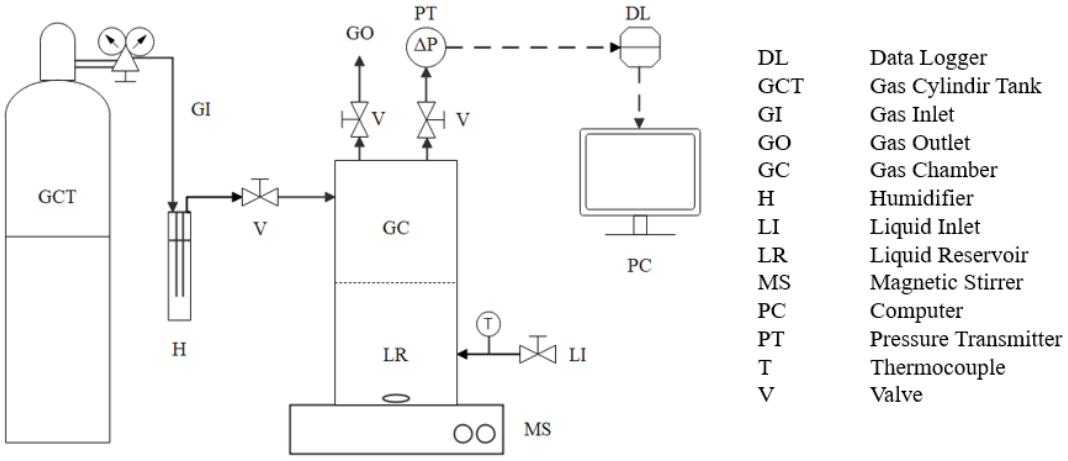

Figure 1. The stirred cell reactor system.

DOI: https://doi.org/10.22452/mjs.vol43sp1.10
Malaysian Journal of Science 43 (Special Issue 1): 58-66 (July 2024)

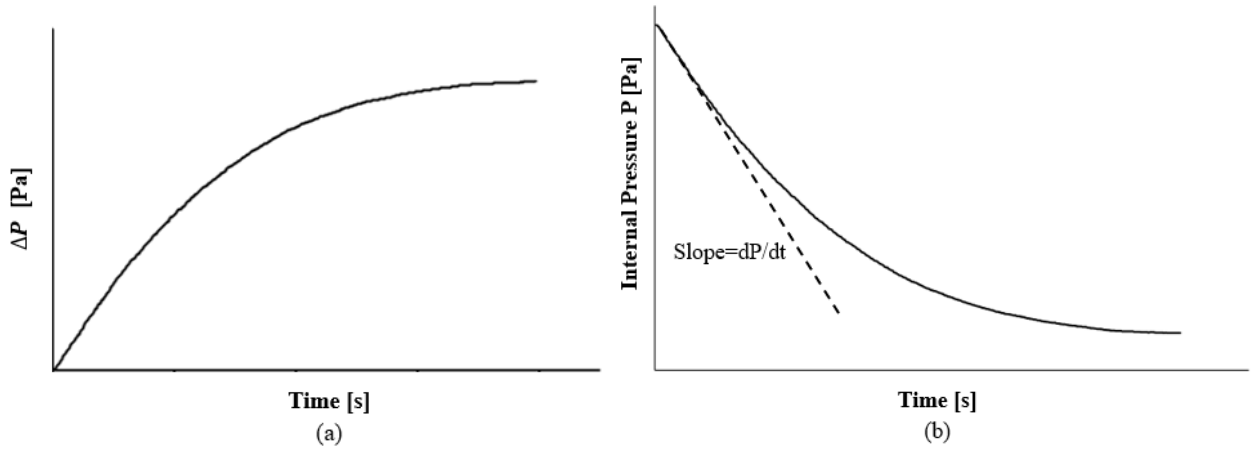

Figure 2. (a) Increase in pressure drop (ΔP) in the gas chamber of the stirred cell reactor with time; (b) The change in the internal pressure (P) in the gas chamber of the stirred cell reactor with time.

2.4 Determination of the Total CO_2 Absorption Capacity

The total CO_2 absorption capacity calculations are made with the ideal gas equation shown in Eq. (14) (Smith et al., 2022).

$$PV_g = ZnRT \quad (14)$$

In this equation, P is the gas pressure [Pa] in the stirred cell reactor gas chamber; V_g is the gas volume [m^3], Z is the compressibility factor [0.995], n is the mole of carbon dioxide gas [mol], R is the gas constant [8.314 Pa-m^3-mol^{-1}-K^{-1}], T is the temperature [K].

The pressure determination in the gas chamber of the stirred cell reactor is calculated with the difference between the atmospheric pressure and the pressure drop measured from the transmitter which is shown in Eq. (15).

$$P = P_{atm} - \Delta P \quad (15)$$

The pressure drop values in the gas chamber were recorded on the computer via the pressure transmitter and then these data were plotted against the time. An example of the graph of the pressure drop versus time in stirred cell reactor is shown in Figure 2 (a). The ordinate of the graph represents the pressure drop difference (ΔP) measured from the transmitter in Pa units, and the abscissa represents the time in seconds.

According to the pressure drop values fixed at the end of the experiment, the mole of CO_2 gas remaining in the gas chamber was calculated with the ideal gas equation (Eq. (14)). Then, by taking the difference between gas moles in the initial and final state, the amount of CO_2 absorbed into the unit volume of absorption liquid also was calculated (Genç Çelikçi, 2020).

2.5 Determination of the Dissolution Rate

The dissolution rate experimental procedure is the same as the total CO_2 absorption capacity experiments but theoretically different. Eq. (16) is obtained by taking and arranging the differential of the ideal gas equation represented by Eq. (14) (Uysal, 2016).

$$dn = \frac{V_g}{ZRT} dP \quad (16)$$

Since the experiments are performed as a function of time, the variation of the expression obtained by Equation 16 with time is shown in Eq. (17) (Uysal, 2016).

$$w = \frac{dn}{dt} = \frac{V_g}{zRT}\frac{dP}{dt} \quad (17)$$

Here w is the dissolution rate [mol-s^{-1}] of CO_2 in absorption solutions. The part on the right side of the equation expresses the change in moles of CO_2 due to the absorption of CO_2 in the gas chamber into the absorption solutions over time.

The internal pressure in the gas chamber was calculated with Eq. (15) and the plot is shown in Figure 2 (b). In order to determine the pressure change (dP/dt) over time, the slope of the first part of the graph, in which it proceeds linearly, was calculated.

The absorption takes place in the liquid reservoir volume (V_L), and the dissolution rate of CO_2 in the solution can be shown by Eq. (18) (Uysal, 2016).

$$r = \frac{w}{V_L} = -\frac{1}{V_L}\frac{V_g}{zRT}\frac{dP}{dt} \quad (18)$$

In Eq. (18), r is the rate of the absorption process relative to the total solution volume from the unit [mol-m^{-3}-s^{-1}], the slope read from the graph from the unit of dP/dt [Pa-s^{-1}] on the right side of the equation, V_L, solution volume [m^3], V_g, gas volume [m^3], T is the gas constant in [K], temperature, R [8.314 Pa-m^3-mol^{-1}-K^{-1}].

3. Results and discussion

3.1. Total CO_2 Absorption Capacity and Dissolution Rate

As a result of all experiments, the dissolution rate (w), the rate of the absorption process relative to the total liquid volume (r), and the total CO_2 absorption capacity were calculated at 20°C and 91 kPa. All experiments were repeated three times and since the values are close to each other, the average values were determined for each solution. The results of the 0.1-1.5 M alkaline solutions (KOH, NaOH) and amino acids (KGly, NaGly) solutions experiment results are shown in Table 1. It was determined that the dissolution rate (w), the rate of the absorption process

DOI: https://doi.org/10.22452/mjs.vol43sp1.10
Malaysian Journal of Science 43 (Special Issue 1): 58-66 (July 2024)

Table 1. Experimental Results of Total CO2 Absorption Capacity and Dissolution Rate for Each Solution.

Solution	Molarity (M)	w* (mol/s)	r** (mol/m³-s)	Total CO_2 absorption capacity (g/L)
KOH	0.1	2.32×10^{-6}	0.006	0.030
	0.5	1.06×10^{-5}	0.026	0.140
	1	2.14×10^{-5}	0.054	0.371
	1.5	2.95×10^{-5}	0.064	0.558
NaOH	0.1	2.98×10^{-6}	0.007	0.071
	0.5	1.09×10^{-5}	0.028	0.132
	1	2.05×10^{-5}	0.048	0.222
	1.5	3.26×10^{-5}	0.081	0.420
KGly	0.1	2.14×10^{-6}	0.005	0.019
	0.5	5.84×10^{-6}	0.015	0.087
	1	6.64×10^{-6}	0.017	0.117
	1.5	1.19×10^{-5}	0.030	0.183
NaGly	0.1	2.37×10^{-6}	0.006	0.020
	0.5	4.81×10^{-6}	0.012	0.062
	1	6.80×10^{-6}	0.017	0.080
	1.5	1.26×10^{-5}	0.031	0.132
Gly	0.1-1.5	$(8.02\text{-}8.30) \times 10^{-7}$	0.0021-0.0022	0.006

w*: Dissolution rate
r**: The rate of the absorption process relative to the total liquid volume

relative to the total liquid volume (r), and the total CO_2 absorption capacity increase as the solution concentration increases.

The dissolution rate (w), the rate of the absorption process relative to the total liquid volume (r), and the total CO_2 absorption capacity are shown graphically in Fig (3), Fig (4), and Fig (5), respectively.

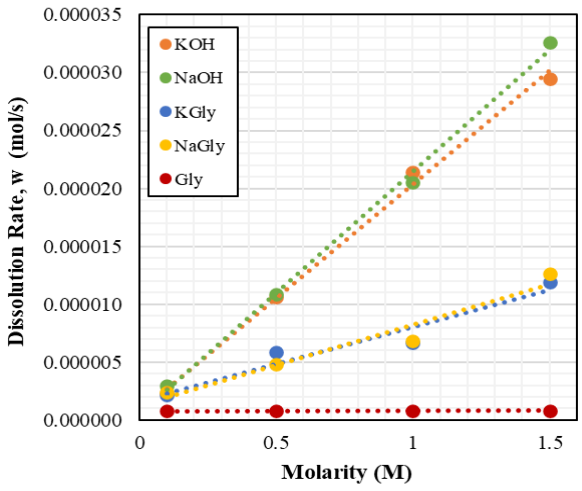

Figure 3. The dissolution rate of CO2 in absorption solutions for comparison of each solution

When the results are compared, alkaline solutions (NaOH and KOH) give better results than amino acid salt solutions (KGly and NaGly), as expected. Because alkaline solutions have high pH so carbonate and bicarbonate formation rates faster than amino acid salt solutions. Also, glycine solution gives the lowest result. Under ambient conditions, potassium glycinate gives slightly better results than sodium glycinate. According to increasing concentration, dissolution rate and total CO_2 absorption capacity

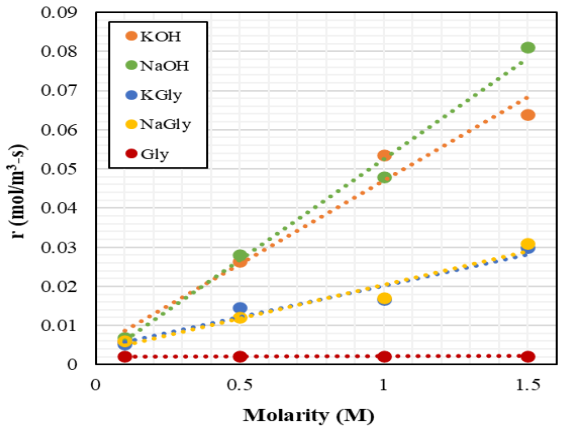

Figure 4. Rate of the absorption process relative to the total liquid volume for comparison of each solution.

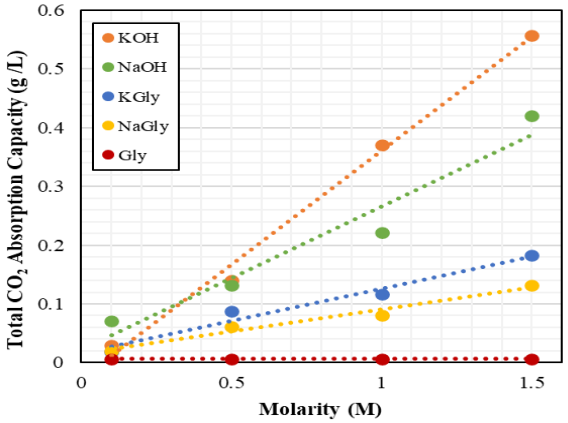

Figure 5. Total CO_2 absorption capacity for comparison of each solution.

DOI: https://doi.org/10.22452/mjs.vol43sp1.10
Malaysian Journal of Science 43 (Special Issue 1): 58-66 (July 2024)

Table 2. Experimental results for total CO_2 absorption capacity of KGly and NaGly

Solution	Concentration	T (K)	Apparatus	Total CO_2 absorption capacity (mol CO_2/mol solution)	References
NaGly	10-30 wt%	303-323	Vapor-Liquid Equilibrium Cell	0.17-1.07	Song et. al (2006)
NaGly	1-30 wt%	298, 313	High Pressure Cell	0.5-1.6	Harris et. al (2009)
KGly	0.1-3 M	293-351	Stirred Reactor	0.1-1.4	Portugal et. al (2009)
KGly	0.1, 1, 3 M	308.15	N/A	0.456-2.62	Mohsin et. al (2018)
NaGly	0.1-1.5 M	293	Stirred Cell Reactor	0.09-0.20	This work
KGly	0.1-1.5 M	293	Stirred Cell Reactor	0.13-0.19	This work

Table 3. pH Measurements of Solutions Before and After CO2 Loading.

Solution	Molarity (M)	pH (Before CO_2-loading)	pH (After CO_2-loading)
KOH	0.1	12.50	12.45
	0.5	13.17	13.01
	1	13.39	13.29
	1.5	13.48	13.23
NaOH	0.1	12.95	12.56
	0.5	13.00	12.94
	1	13.05	12.90
	1.5	13.25	13.07
KGly	0.1	10.11	9.89
	0.5	10.25	10.12
	1	10.47	10.31
	1.5	10.60	10.47
NaGly	0.1	10.22	10.05
	0.5	10.54	10.49
	1	10.63	10.44
	1.5	10.77	10.32
Gly	0.1	6.23	5.90
	0.5	6.28	5.92
	1	6.33	5.95
	1.5	6.35	5.98

DOI: https://doi.org/10.22452/mjs.vol43sp1.10
Malaysian Journal of Science 43 (Special Issue 1): 58-66 (July 2024)

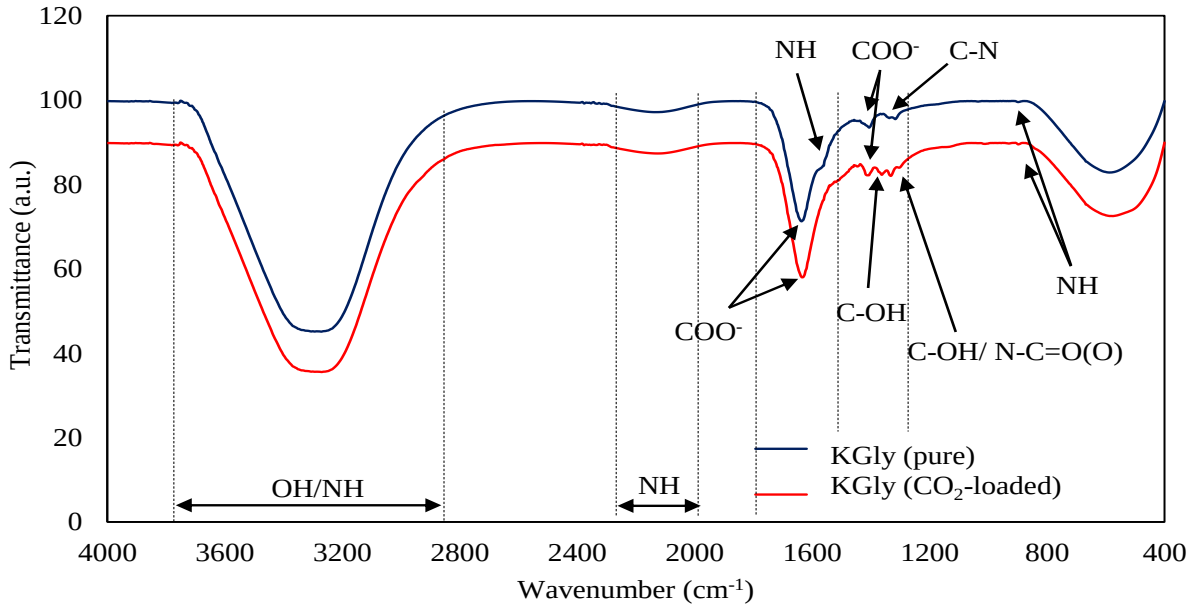

Figure 6. FTIR Spectra of KGly before and after CO_2 absorption.

approximately 1.4 times better results than sodium glycinate in terms of total CO_2 absorption capacity at the highest concentration.

According to Table 2, it can be said that sodium glycinate and potassium glycinate have different results under different experimental conditions. In this work, it was found that the experimental results of this work under atmospheric working conditions are lower than in the literature results. Studies can be carried out under higher pressure conditions and lower temperature conditions. Thus, higher absorption capacities can be achieved.

Table 3 shows the pH graph of the amino acid salt solutions potassium glycinate, sodium glycinate, and the alkaline solutions potassium hydroxide, sodium hydroxide before and after CO_2 loading. At high concentrations, the pH is also high due to the alkaline solution concentration. The high solution pH increases the reaction rate of CO_2 with OH^-. This causes an increase in the absorption rate of CO_2. At higher concentrations where the pH is high, the total CO_2 absorption capacity and dissolution rate experimental results are also better.

3.2. FTIR Results for Potassium Glycinate Solution

Potassium glycinate and sodium glycinate solutions have nearly similar results however, potassium glycinate gave slightly better results in terms of total CO_2 absorption capacity and dissolution rate. This comparison aroused the interest of the authors to observe the interaction between the amino acid salt solution and CO_2, and FTIR analysis was performed on pure and CO_2-loaded potassium glycinate solution for comparison. Functional groups of potassium glycinate were identified using Fourier Transform Infrared (FTIR) spectrometer (PerkinElmer) in METU Central Laboratory. FTIR spectra of potassium glycinate solution before and after CO_2 absorption were recorded at wavenumber ranging from 4000 to 400 cm^{-1} and results is shown in Fig. 6.

Fig. 6 shows that interactions occur between CO_2 and potassium glycinate due to the formation of new peaks as a result of CO_2-loaded. Table 4 indicates the characteristic peaks detected in the FTIR spectra of 0.5 M potassium glycinate solution before and after CO_2 absorption. While pure potassium glycinate FTIR spectrum is available in the literature, no data could be found for the CO_2-loaded potassium glycinate solution. Pure potassium glycinate FTIR spectra were also compared with Mohsin et al. (2018) and their results is also shown in Table 4.

Table 4. The Characteristics Peaks of Potassium Glycinate Before and After CO_2 Absorption.

Functional Groups	Wavenumber (cm^{-1}) This work Pure KGly	Wavenumber (cm^{-1}) This work CO_2-loaded KGly	Wavenumber (cm^{-1}) Mohsin et al. (2018) Pure KGly
OH/NH	3271	3270	3332
NH	2135	2126	2210
COO-	1636	1635	1630
NH	1559	-	1562
COO-	1405	1410	1404
C-OH	-	1362	-
C-OH/ N-C=O(O) (carbamate)	-	1332	-
C-N	1316	-	1320
NH	904	893	894

As can be seen in Table 4, the potassium glycinate spectrum was similar with the spectra reported by Mohsin et al. (2018). The OH characteristic peak was observed at approximately 3271 cm^{-1}, due to water molecules in KGly structure. The NH and COO^- peaks were observed 2135 and 1636 cm^{-1}, respectively. The last peaks

DOI: https://doi.org/10.22452/mjs.vol43sp1.10
Malaysian Journal of Science 43 (Special Issue 1): 58-66 (July 2024)

C-N and NH were observed at 1316 and 904 cm^{-1} and these peaks show the presence of amine in KGly structure. When the results of CO_2-loaded solution are examined, it can be seen that new peak intensities occur at 1332 and 1362 cm^{-1} wavenumbers. In the literature, the presence of C-OH functional groups in the range of 1400-1300 cm^{-1} and the presence of N-C=O(O) carbamate groups at 1322 cm^{-1} are mentioned (Jacson et al., 2009). The peaks here are thought to occur as a result of carbonate (CO_3^{2-}) and bicarbonate ions (HCO_3^-) formed as a result of the reaction of potassium glycinate solution with CO_2. Also in the literature, Falk & Miller (1992) reported peak intensities of 1385 cm^{-1} for CO_3^{2-} and 1360 cm^{-1} for HCO_3^-. According to the reaction mechanism between CO_2 and amino acid solution, carbamate and carbonate ions at similar peak intensities in the literature were determined by FTIR analysis in this study.

4. Conclusion

In this work, potassium and sodium glycinate solutions used as amino acid salt solutions were compared with alkaline solutions potassium and sodium hydroxide. The total CO_2 absorption capacity and dissolution rate of the solutions were investigated experimentally. According to the results, alkaline solutions gave the best results due to their high pH, while potassium glycinate gave approximately 1.4 times better results than sodium glycinate. In addition, characteristic functional groups were determined for both pure and CO_2-loaded solutions in FTIR analysis of potassium glycinate. According to the potassium glycinate-CO_2 reaction mechanism, it has been shown that carbamate and C-OH bonds are formed in the CO_2-loaded solution. When the study is evaluated, the use of amino acid salt solutions in CO_2 capture systems can reduce the use of toxic and hazardous solutions such as sodium hydroxide and potassium hydroxide, and also have the potential as promising solutions for CO_2 absorption. In the future, a detailed study of adding additives to amino acid salt solutions which will increase absorption performance, will be investigated.

5. Acknowledgement

The authors would like to acknowledge Em. Prof. Dr. Bekir Zühtü UYSAL for his valuable knowledge and constructive suggestions.

6. References

Aghel B., Maleki M., Sahraie S., & Heidaryan E. (2021). Desorption of carbon dioxide from a mixture of monoethanolamine with alcoholic solvents in a microreactor. *Fuel* 306:121636.

Ahn S., Song HJ., Park JW., Lee JH., Lee IY., & Jang KR. (2010). Characterization of metal corrosion by aqueous amino acid salts for the capture of CO_2. Korean J Chem Eng 27:1576-1580.

Ahmed R., Liu G., Yousaf B., Abbas Q., Ullah H., & Ali MU. (2020). Recent advances in carbon-based renewable adsorbent for selective carbon dioxide capture and separation-A review. *J Clean Prod* 242:118409.

Bernhardsen IM., & Knuutila HK. (2017). A review of potential amine solvents for CO_2 absorption process: absorption capacity, cyclic capacity and pKa. *Int J Grenh Gas Control* 61:27-48.

Buckingham J., Reina TR., & Duyar MS. (2022). Recent advances in carbon dioxide capture for process intensification, *Carbon Capture Science & Technology* 2:100031.

Babamohammadi S., Shamiri A., & Aroua MK. (2015). A review of CO_2 capture by absorption in ionic liquid-based solvents. *Rev Chem Eng* 31:383-412

Caplow, M. (1968) Kinetics of Carbamate Formation and Breakdown. *J. Am. Chem. Soc.* 90:6796.

Danckwerts, PV. (1979) The Reaction of CO_2 with Ethanolamines, *Chem. Eng. Sci*. 34:443.

Falk M., & Miller AG. (1992). Infrared spectrum of carbon dioxide in aqueous solution, *Vibrational Spectroscopy*, 4:105-108.

Fernandez ES., & Goetheer ELV. (2011). DECAB: process development of a phase change absorption process. *Energy Proceedia* 4:868-875.

Figueroa JD., Fout T., Plasynski S., McIlvried H., & Srivastava RD. (2008). Advances in CO_2 capture technology-The U.S. Department of Energy's Carbon Sequestration Program. *Int J Greenh. Gas Control* 2:9–20.

Gatti M., Martelli E., Marechal F., & Consonni S. (2014). Review, modeling, Heat Integration, and improved schemes of Rectisol®-based processes for CO_2 capture. *Appl. Therm. Eng.* 70:1123-1140.

Genç Çelikçi G. (2020). *Carbon Dioxide Capture in Structured Packing Column with n-Butanol and Ethyl Acetate*, Ph.D. Thesis, Gazi University, Ankara.

Ghosh UK., Kentish SE., & Stevens GW. (2009). Absorption of carbon dioxide into aqueous potassium carbonate promoted by boric acid. *Energy Procedia* 1:1075-1081.

Guo D., Thee H., Tan CY., Chen J., Fei W., Kentish SE., Stevens GW., & da Silva G. (2013). Amino Acids as Carbon Capture Solvents: Chemical Kinetics and Mechanism of the Glycine + CO_2 Reaction. *Energy &Fuels*, 27:3898-3904.

Harris F., Kurnia KA., Mutalib MI., & Thanapalan M. (2009). Solubilities of Carbon Dioxide and Densities of Aqueous Sodium Glycinate Solutions before and after CO_2 Absorption, *J. Chem. Eng. Data* 54:144-147.

Hu G., Smith KH., Wu Y., Mumford KA., Kentish SE., & Stevens GW. (2018). Carbon Dioxide Capture by Solvent Absorption Using Amino Acids: A Review. *Chin. J. Chem. Eng*. 26: 2229-2237.

IPCC. (2005). *Carbon Dioxide Capture and Storage*. Prepared by Working Group III of the Intergovernmental Panel on Climate Change, [Metz, B., O. Davidson, H. C. de Coninck, M. Loos, and L. A. Meyer (eds.)]. Cambridge University Press, Cambridge, UK and New York, NY, USA.

DOI: https://doi.org/10.22452/mjs.vol43sp1.10
Malaysian Journal of Science 43 (Special Issue 1): 58-66 (July 2024)

IPCC (2022). *Climate Change 2022: Impacts, Adaptation and Vulnerability.* Contribution of Working Group II to the Sixth Assessment Report of the Intergovernmental Panel on Climate Change [H.-O. Pörtner, D.C. Roberts, M. Tignor, E.S. Poloczanska, K. Mintenbeck, A. Alegría, M. Craig, S. Langsdorf, S. Löschke, V. Möller, A. Okem, B. Rama (eds.)]. Cambridge University Press. Cambridge University Press, Cambridge, UK and New York, NY, USA.

Jacson P., Robinson K., Puxty G., & Attalla M. (2009). In situ Fourier Transform-Infrared (FT-IR) analysis of carbon dioxide absorption and desorption in amine solution, *Energy Procedia*, 1:985-994.

Keith DW., Holmes G., St. Angelo D., & Heidel K. (2018). A process for capturing CO_2 from the atmosphere. *Joule* 2:1573-1594.

Kucka L., Richter J., Kenig EY., & Górak A. (2003). Determination of gas–liquid reaction kinetics with a stirred cell reactor. *Sep. Purif. Technol*. 2:163-175.

Kumar PS., Hongendoorn JA., Versteeg GF., & Veron PHM. (2003). Kinetics of the Reaction of CO_2 with Aqueous Potassium Salt of Taurine and Glycine. *AIChE J*. 49: 203-213.

Lee S., Song H., Maken S., & Park J. (2007). Kinetics of CO_2 Absorption in Aqueous Sodium Glycinate Solutions, *Ind. Eng. Chem. Res*. 46: 1578-1583.

Li J., Ye Y., Chen L., & Qi Z. (2012). Solubilities of CO_2 in Poly(ethylene glycols) from (303.15 to 333.15) K. *J. Chem. Eng. Data* 57:610-616.

Luis P. (2016). Use of monoethanolamine (MEA) for CO_2 capture in a global scenario: Consequences and alternatives. *Desalination* 380:93-99.

Majchrowicz ME., Kersten S., & Brilman W. (2014). Reactive Absorption of Carbon Dioxide in L-Prolinate Salt Solutions. *Ind. Eng. Chem. Res.* 53:11460-11467.

Mohsin HM., Johari K., & Shariff AM. (2018). Virgin coconut oil (VCO) and potassium glycinate (PG) mixture as absorbent for carbon dioxide capture, *Fuel* 232:454-462.

Murrieta-Guevara F., Romero-Martinez A., & Trejo A. (1988). Gas solubilities of carbon dioxide and hydrogen sulfide in sulfolane and its mixtures with alkanolamines. *Fluid Ph. Equilibria* 44:105-115.

National Aeronautics and Space Administration (NASA), Climate Change Carbon Dioxide Latest Measurements, United States https://climate.nasa.gov/vital-signs/carbon-dioxide/ (accessed 2023-06-22).

Ochedi FO., Yu J., Yu H., Liu Y., & Hussain A. (2021). Carbon dioxide capture using liquid absorption methods: a review, Environmental *Chemistry Letters*, 19:77-109.

Olajire AA. (2010) CO_2 capture and separation technologies for end-of-pipe applications–A review. *Energy* 35:2610-2628.

Portugal A., Sousa J., Magalhães F., & Mendes A. (2009). Solubility of carbon dioxide in aqueous solutions of amino acid salts. *Chem. Eng. Sci.* 64: 1993–2002.

Puxty G., Rowland R., Allport A., Yang Q., Bown M., Burns R., & Attala M. (2009). Carbon Dioxide Postcombustion Capture: A Novel Screening Study of The Carbon Dioxide Absorption Performance of 76 Amines. *Environ. Sci. Technol.* 43:6427-6433.

Smith JM., Van Ness HC., Abbott MM., & Swihart MT. (2022) *Introduction to Chemical Engineering Thermodynamics*, pp. 78, New York, USA: Mc Graw-Hill.

Song H., Lee S., Maken S., Park JJ., & Park JW. (2006). Solubilities of carbon dioxide in aqueous solutions of sodium glycinate. *Fluid Phase Equil*. 246: 1–5.

Thee H., Nicholas J., Smith KH., da Silva G., Kentish SE., & Stevens GW. (2013). A kinetic study of CO_2 capture with potassium carbonate solutions promoted with various amino acids: Glycine, sarcosine and proline. *Int. J. Greenh. Gas Control.* 20:212-222.

Uysal D. (2016). *Absorption of Carbon Dioxide into Calcium Acetate Solution*, Ph.D. Thesis, Gazi University, Ankara.

Vaidya PD., Konduru P., Vaidyanathan M., & Kenig EY. (2010). Kinetics of carbondioxide removal by aqueous alkaline amino acid salts. *Ind. Eng. Chem. Res.* 49:11067–11072.

Wang F., Zhao J., Miao H., Zhao J., Zhang H., Yuan J., & Yan J. (2018). Current status and challenges of the ammonia escape inhibition technologies in ammonia-based CO_2 capture technologies, *Appl. Energy* 230:734-749.

Wang M., Lawal A., Stephenson P., Sidders J., & Ramshaw C. (2011). Post-combustion CO_2 capture with chemical absorption: a state-of-the-art-review. *Chem. Eng. Res. Des.* 89:1609-1624.

Wu Y., Xu J., Mumford K., Stevens GW., Fei W., & Wang Y. (2020). Recent advances in carbon dioxide capture and utilization with amines and ionic liquids. *Green. Chem. Eng.* 1:16-32.

Ying J., & Eimer DA. (2013). Determination and measurements of mass transfer kinetics of CO_2 in concentrated aqueous monoethanolamine solutions by a stirred cell *Ind. Eng. Chem. Res*. 52: 2548–2559.

Yuan X., Wang J., Deng S., Suvarna M., Wang X., Zhang W., Hamilton ST., Alahmed A., Jamal A., Park AHA., Bi X., & Ok YS. (2022). Recent advancements in sustainable upcycling of solid waste into porous carbons for carbon dioxide capture. *Renewable Sustainable Energy Rev.* 162:112413.

Zhang Z., & Huisingh D. (2017). Carbon dioxide storage schemes: technology, assessment and deployment. *J. Clean. Prod.* 142:1055-1064.

DOI: https://doi.org/10.22452/mjs.vol43sp1.10
Malaysian Journal of Science 43 (Special Issue 1): 58-66 (July 2024)